INVERSE SCATTERING BY UNBOUNDED ROUGH SURFACES

A thesis submitted for the degree of Doctor of Philosophy

by

Claire Deborah Lines

Department of Mathematical Sciences, Brunel University

June 2003

I dedicate this thesis to my family

Acknowledgements

I would like to acknowledge the help and support I have been given throughout my PhD foremost, and most importantly, from my supervisor, Dr Simon Chandler-Wilde. I must also mention the encouragement I received from Anja Meier and Tilo Arens plus the rest of the research group at Brunel over the last three and a half years. On a wider scale I would like to thank Dr Roland Potthast for his help during and after his position at Brunel.

On a personal note obviously my friends and family have played a vital role in providing support and motivation during all my studies, namely Angie, Anne, Karen, and Phil, Sam, Vanessa, Dad and Jake and of course not forgetting, Nobby and Stella.

I would also like to recognize the Mathematical Sciences Department for those who have made my stay there enjoyable as well as educational. I have had an awful lot of fun whilst there and this is mainly due to the great characters working there.

Abstract

We consider the problem of inverse scattering of electromagnetic waves by perfectly conducting unbounded rough surfaces. We describe a new algorithm (a Point Source Method) based on the method of Potthast (IMA J.Appl.Math. 61, 119 – 140, 1998) for inverse scattering by bounded obstacles. The algorithm proposed requires the approximate solution of an ill-posed first kind integral equation which reconstructs the scattered field above the surface, when the incident field is that due to a time harmonic point source. To solve this equation we study the theory of Tikhonov regularisation for solving ill-posed operator equations on Hilbert spaces in the case when the operator is not compact. We apply this theory and a detailed analysis of various related direct problems to show that we can solve the integral equation arising in the Point Source Method to arbitrary accuracy. Moreover we include a complete analysis of the method which shows that the approximation to the total field produced by the Point Source Method tends to the actual total field, the solution of the direct scattering problem, as the regularisation parameter tends to zero. Numerical results show that, for a variety of surfaces, reconstructions of the total field agree well with exact values of the total field. Two methods are described and results shown to predict the surface location from the absolute values of the reconstructed total field, using the a priori knowledge that the total field vanishes on the boundary. We go on to propose an extension of the Point Source Method which can reconstruct the total field when the incident field is not necessarily time harmonic. In particular we

consider inverse rough surface scattering problems with geometry and incident pulses similar to those arising in ground penetrating radar (GPR) applications. We produce and analyse results showing great accuracy of reconstruction of the total field and of the surface location in the case when the total field vanishes on the boundary. We propose that the location of the surface can be predicted as the locus of points where the incident and reflected pulses coincide in time in the case of more general boundary conditions.

Contents

List of Tables

List of Figures

Chapter 1

Introduction

This thesis is concerned with the problem of inverse scattering by infinite rough surfaces ("rough surface" in the sense of [43, 49], see page 7 below). We describe a new Point Source Method to reconstruct the total field on and above the boundary. The method is based on the Point Source Method of Potthast [44], for inverse scattering by bounded obstacles. During the analysis of the new Point Source Method (Chapter 4) we will see that it is necessary to also fully analyse three direct scattering problems (see Chapter 3). We show a series of numerical results comparing the exact total field with the reconstructed total field, due to a time harmonic incident field, computed using the Point Source Method. From the total field we go on to predict the surface location. In Chapter 5 we develop the Point Source Method for incident fields that are time dependent but not necessarily time harmonic. We show that reconstructions of the total field in the time domain computed using the Point Source Method agree well with the exact total field and that we can predict the surface location in such a way that the Point Source Method can be expected to work for any boundary condition.

In this introduction we will define fully the direct and inverse scattering problems and discuss the difficulties involved with inverse scattering problems. We give brief histories of methods for inverse scattering by bounded obstacles which is a much more well established area than that of inverse scattering by unbounded obstacles, and also give a review of the methods currently used in practice for inverse scattering by unbounded surfaces. We then present a detailed overview of the thesis and finally provide a list of mathematical tools and notations used repeatedly throughout the thesis.

The scattering of acoustic and electromagnetic waves plays a vital role in many areas of applied sciences. Acoustic and electromagnetic waves are used in areas such as non-destructive testing, medical imaging, archeology, radar, remote sensing, ultrasound tomography and seismic exploration. Broadly speaking, scattering theory is concerned with the effect an inhomogeneity has on an incident wave. In particular, if the total field is viewed as the sum of an incident field u^i and a scattered field u^s

then the *direct scattering problem* is to determine u^s from a knowledge of the incident field and the inhomogeneity. The *inverse scattering problem* takes the solution of the direct scattering problem, u^s, as the starting point and asks what is the nature of the inhomogeneity that gave rise to this scattered field.

The study of inverse problems has become an active area of research only in the last 40 years mainly due to a historical prejudice dating back to Hadamard, who claimed that a mathematical model for a physical problem has to be properly or well-posed in the sense that it has the following three properties:

1. There exists a solution of the problem (existence).
2. There is at most one solution of the problem (uniqueness).
3. The solution depends continuously on the data (stability).

The most important requirement is that of stability. If a problem lacks this property then small errors in measurement or numerical computation may lead to large errors in the solution. Mathematically, many well-posed problems take the form specified in the following definition.

Definition 1.0.1 *Let X and Y be normed spaces, $K : X \to Y$ a (linear or non-linear) mapping. The equation $Kx = y$ is called* properly posed *or* well-posed *if the following holds:*

1. Existence. *For every $y \in Y$ there is (at least one) $x \in X$ such that $Kx = y$.*

2. Uniqueness. *For every $y \in Y$ there is at most one $x \in X$ with $Kx = y$.*

3. Stability. *The solution x depends continuously on y, i.e., for every sequence $(x_n) \subset X$ with $Kx_n \to Kx$ as $n \to \infty$, it follows that $x_n \to x$ as $n \to \infty$.*

Equations for which (at least) one of these properties does not hold are called improperly posed *or* ill-posed.

It turns out that many interesting and important inverse problems in science including those in inverse scattering, are ill-posed problems. So it was not until Tikhonov developed regularisation techniques for linear ill-posed problems in the mid 1960's and the necessary computational facilities had been developed that an effective study of inverse scattering problems could be made. For simplicity we will concentrate on scattering by time harmonic acoustic waves within this introduction, although the theory we describe is also relevant for electromagnetic waves, which is what we will be studying throughout the rest of this thesis.

Acoustic wave motion is determined by the velocity potential. Let $U(x,t)$ denote the velocity potential at point x at time t. Then in a homogenous medium U satisfies the wave equation

$$\frac{\partial^2 U}{\partial t^2} = c^2 \Delta U$$

where Δ denotes the Laplace operator, and the constant $c > 0$ is the wave speed. For time harmonic waves $U(x,t) = \Re\{u(x)\exp^{-i\omega t}\}$ for some angular frequency $\omega > 0$. The space dependent part u satisfies the Helmholtz equation

$$\Delta u + k^2 u = 0,$$

where the wave number $k > 0$ is given by $k = \omega/c$. It is convenient to regard u as the sum of the incident field u^i, the solution in the absence of the scattering object, and a scattered field u^s, so that $u = u^i + u^s$.

1.1 Current Work on Inverse Scattering

The area of direct scattering is a well studied one, and much of the present effort is directed towards the speed and accuracy of computational implementation rather than further theoretical developments [49, 54, 18]. The area of inverse scattering, however, has been far less studied for reasons discussed in the previous section, but is

currently a highly active area with an abundance of new ideas. Presently, investigations into inverse scattering by bounded obstacles fall into three categories: iterative methods; decomposition methods; and sampling-and-probe methods. General iterative methods use the field calculated from solving the direct problem for a boundary $\partial\Omega$, and from this the corresponding measured data being considered is subtracted. When this difference is "small", $\partial\Omega$ is deemed to be the boundary from which the measured data was obtained. In particular the Newton method requires solution of the direct problem at each iteration step. One needs to know the relevant physical properties of the scattering obstacle which determine some kind of parameterisation capable of describing the boundary of the scattering obstacle. For further details we refer the reader to [28, 29, 35].

The second category is decomposition methods, for the reconstruction of sound-soft or perfectly conducting surfaces, precisely surfaces on which $u = u^i + u^s$ vanishes, which decompose the problem into two parts, a linear ill-posed problem and a nonlinear well-posed problem. Examples of such methods are the method of Kirsch and Kress [33], the method of Colton and Monk [15, 14] and the Point Source Method of Potthast [45]. In each method the first problem solved is to reconstruct the scattered field from the far field pattern. This problem is linear but ill-posed. The second step, well-posed but nonlinear, is to determine the unknown boundary of the scatterer as the location of zeros of the total field $u = u^i + u^s$. These methods have the advantage that no direct problem needs to be solved but on the other hand some a priori information about the position and type of boundary is required.

The third category of methods, the sampling and probe methods, involve characterising the boundary of the scattering body by an indicator function and then calculating this function approximately. From the behaviour of this function the scatterer can be determined. The Linear Sampling Method by Colton and Kirsch [12] and the improved version of this, the Factorisation Method by Kirsch, described in [11, 31, 32], are both examples of this type of method. To give a brief description of

these we first define the far field operator $F : L^2(S) \to L^2(S)$, where $S := \{x| \, |x| = 1\}$, by

$$(Fg)(\hat{x}) := \int_S u_\infty(\hat{x}, d)g(d)\mathrm{ds}(d), \qquad \hat{x} \in S.$$

In this equation $u_\infty(\hat{x}, d)$, for $x, d \in S$, is the far field pattern of the scattered field in direction $\hat{x}$ when the incident field is a plane wave in direction d. Now the linear sampling method uses regularisation to solve the first kind integral equation

$$(Fg)(\hat{x}) = \Phi_\infty(\hat{x}, z), \qquad \hat{x} \in S,$$

where $\Phi_\infty(\hat{x}, z)$ is the far field pattern in direction $\hat{x}$ of the total field due to a unit point source at the point z in the case where no scattering obstacle is present. The mathematical problem with this is that the range of the far field operator is unknown. The Factorization Method of Kirsch solves instead the equation

$$(F^*F)^{\frac{1}{4}}g = \Phi_\infty(\cdot, z),$$

and he has shown that $\Phi_\infty(\cdot, z)$ is in the range of $(F^*F)^{\frac{1}{4}}$ if and only if $z \in \Omega$ where Ω is the region occupied by the scatterer and F^* is the adjoint of F, defined in Theorem 2.1.1 [12, 16, 32, 31]. In both of these methods the equation is solved on a grid which is known to contain the unknown scatterer and the boundary is found to be the set of points where $\|g\|$ begins to increase sharply. Even though no boundary condition is required for these methods to work, some information as to where the scatterer is positioned is required. The amount of data needed is immense, namely $u_\infty(\hat{x}, d)$ for all $\hat{x}, d \in S$ [11], and the precision is low. The singular sources method due to Potthast [45] has similar advantages and disadvantages to the previous two methods but it also reconstructs some physical properties of the scatterer. The latest two methods, the No-Response test of Luke and Potthast [46] and the Range test of Potthast and Sylvester-Kusiak [47] again reconstruct the scatterer with no a priori information. Both these methods use much less data, but a convergence theory is lacking.

This thesis is concerned with scattering by unbounded rough surfaces, by which we mean, as in [43], the problem of scattering by an infinite surface which is the graph of some bounded function f. When studying the problem of inverse scattering by unbounded rough surfaces, one must distinguish between the deterministic problem, where reconstructions of the shape of the surface profile are made, and the statistical problem, which consists of the estimation of statistical parameters which are supposed to characterise the surface profile. One of the most popular ways of describing the roughness of a rough surface is the root mean square (rms) height defined as

$$\sigma := \sqrt{\langle f^2 \rangle},$$

where $\langle \cdot \rangle$ denotes a spatial average [25] and it is assumed, without loss of generality, that $\langle f \rangle = 0$. The reconstruction of some partial information about the rough surface [51, 24] or its statistical parameters, such as the root mean square height or the correlation length [37, 38, 36], is easier than the problem of finding the surface profile deterministically. Often the rough surface is assumed to be Gaussian distributed which is not valid for a number of natural surfaces. Many of these surfaces contain variations in their surface height which are typically smaller than the wavelengths, and under these circumstances the validity requirements for the Kirchhoff approximation or quasi-specular models, to obtain rough surface parameters, are not met. To try and overcome this problem Marchand has combined the quasi-specular model with the boundary perturbation result (known as the Bragg scattering result) [37, 38]. There seems to have been much progress in recent years in the accuracy with which surface parameters such as correlation length and root mean square height can be numerically estimated [37, 38, 36, 21], making it possible to distinguish natural surfaces from one another. However these advances do not take us closer to describing the shape and location of the surface itself.

As for the deterministic problem, with which this thesis is concerned, advances

have been made, but problems involving highly rough surfaces or grazing incident angles have hardly been studied [51, 52]. Most of the algorithms available are restricted to $2D$ geometry as the field is in its infancy. The three most popular direct scattering methods are the integral equation method, which is applicable over a wide range of surface roughness, the Kirchhoff Approximation Method which can be applied to large roughness scales (up to σ of order λ, the wavelength), and the Small Perturbation Method, applicable to small scale roughness [21]. The associated inverse problem for the Kirchhoff approximation [55, 50] involves approximating the normal derivative of the scattered field on the surface by twice the value of the normal derivative of the incident field on the surface. Reconstructions of the surface profile are made from scattered field data. In the method of [55] it is necessary to measure the amplitude and phase of the scattered field in a certain direction that is highly related to the incident field direction; thus in practice data may be very hard to collect. The method is very sensitive to accuracy and range of incident and scattering angles chosen and the reconstructions start to break down when $\sigma = 0.2\lambda$.

The associated inverse problem for the perturbation approximation [19] reconstructs the rough surface profile from data resulting from illumination by a single frequency field at a fixed illumination angle. The data measured is the whole or part of the far field pattern and the only assumptions made are on the height of the surface and the amount of data available. Reconstructions are limited to $\sigma < 0.1\lambda$.

The accuracy of both methods depends highly on the choice of incident angle and the range of scattering angles chosen [56]. In [56, 25] an iterative method based on the inverse algorithms described in [55] and [19] is discussed. The problems of inverse scattering by a one dimensional perfectly conducting rough surface and a two dimensional rough surface with a Neumann boundary condition are studied. The results presented are limited to that of reconstructions of rough surfaces where the rms height is of order $10^{-1}\lambda$ for one-dimensional rough surfaces or is of order $10^{-3}\lambda$ for two-dimensional rough surfaces.

1.2 Overview of Thesis

This thesis is concerned with the inverse scattering of electromagnetic time harmonic waves incident on an infinite perfectly conducting rough surface. An algorithm for the solution to this problem is described and analysed fully. Numerical results are presented to back up the analytical results and a possible application for the method is described in the last chapter.

In Chapter 2 we provide an analysis of Tikhonov regularisation for solving ill-posed operator equations $Kx = y$ on Hilbert spaces. In this chapter we synthesise results from [30, 34, 3, 17, 27, 26] but, in contrast to recent expositions of the theory of Tikhonov regularisation in [30, 13, 20] and appropriately for problems of scattering by unbounded surfaces, we do not assume compactness of the operator K, so that we are obliged to develop the theory without using the singular value decomposition. The results presented are crucial to the analysis of the algorithm proposed in Chapter 4.

For the investigation and solution of inverse problems, a good understanding is required of the corresponding direct problem. In Chapter 3 we analyse fully three direct scattering problems that are necessary for the analysis developed in Chapter 4. The first problem is that of the scattering of an electromagnetic time harmonic wave incident on a perfectly conducting infinite rough surface. The second is the problem of scattering of a time harmonic wave incident on a rough surface with an impedance boundary condition and the third is the problem of propagation of time harmonic waves within an infinite duct.

In Chapter 4 we discuss the following inverse problem: Given measurements of the total electric field, after scattering by an unknown rough surface, on a finite line above the surface, determine the location of the said surface. We formulate a new algorithm which reconstructs the total field on and above the surface. This is a version of the Point Source Method of Potthast [44] discussed in section 1.1, and is

the first application of the Point Source Method to inverse scattering by unbounded surfaces. We provide a complete analysis of the Point Source Method culminating in theoretical estimates for the error in the reconstructed total field. The lack of compactness of the surface leads to significantly more complicated arguments in the theoretical analysis than in the original Point Source Method [44]. Numerical results compare the reconstructed total field with the exact total field. We go on to predict the surface location in the case of exact measured data and when 5% noise is added to the measured data. Results are shown for sinusoidal surfaces of varying amplitudes and for non-sinusoidal rough surfaces.

In Chapter 5 we generalise the Point Source Method so that the incident pulse is arbitrarily time dependent. Measurements of the total electric field are taken, as a function of time, on a finite line above the surface for a single fixed source position. We produce, using the Point Source Method, what appear to be the first reconstructions of the total electric field in the time domain, i.e. reconstructions of the total electric field as a function of position and time. We show numerical results for geometry and incident pulse similar to those arising in ground penetrating radar (GPR) applications. Comparisons of the reconstructed total field and exact total field show that the reconstructions are excellent even when 5% noise is added to the measurements. Accurate predictions of the surface location are also made.

1.3 Tools and Notation

In this section we collect various miscellaneous mathematical results and notations which are used repeatedly in this thesis.

Theorem 1.3.1 *(***Young's Inequality** *[1]). If* $1 \leq p \leq \infty$, $\psi \in L^p(\mathbb{R})$ *and* $l \in L^1(\mathbb{R})$ *then*

$$\phi(s) = \int_{-\infty}^{+\infty} l(s-t)\psi(t)\,dt$$

exists for almost all $s \in \mathbb{R}$. *Moreover* $\phi \in L^p(\mathbb{R})$ *with*

$$\|\phi\|_p \leq \|l\|_1 \|\psi\|_p.$$

The following result is easily proved by adapting the argument in [53, Section 1.88].

Theorem 1.3.2 *Let* $\gamma \subset \mathbb{R}^2$ *be an open or closed curve of class* C^1 *and finite length, and let* D *be an open subset of* $\mathbb{R}^2$. *Suppose* $l \in C(D \times \gamma)$, $\nabla_x l(x,y) \in C(D \times \gamma)$, $\phi \in L^1(\gamma)$, *and*

$$v(x) := \int_\gamma l(x,y)\phi(y)\,ds(y), \qquad x \in D.$$

Then $v \in C^1(D)$ *and*

$$\nabla v(x) = \int_\gamma \nabla_x l(x,y)\phi(y)\,ds(y), \qquad x \in D.$$

Theorem 1.3.3 *(***Unique continuation for the Helmholtz equation** *[14]). Let* G *be a domain in* $\mathbb{R}^2$ *and suppose* $u \in C^2(G)$ *is a solution of*

$$\Delta u + k^2 u = 0$$

in G *such that* u *vanishes in a neighbourhood of some* $x_0 \in G$. *Then* $u \equiv 0$ *in* G.

In Table 1.1 we collect notations that are used repeatedly throughout this thesis. In this table V denotes some open subset of R^n ($n = 1$ or 2).

$C(V)$	The set of real or complex valued continuous functions defined on V.
$C^n(V)$	The set of n times continuously differentiable functions defined on V.
$BC(V)$	The set of real or complex valued functions that are bounded and continuous on V.
$L^p(V)$	For $1 \leq p < \infty$, the set of those measurable functions $\phi : V \to \mathbb{C}$ for which $\int_V \lvert\phi\rvert^p \mathrm{d}s < \infty$.
$L^\infty(\mathrm{V})$	The collection of all real or complex-valued essentially bounded measurable functions defined on V.
$C^{0,\alpha}(V)$	$\{\phi \in BC(V) : \lVert\phi\rVert_{C^{0,\alpha}(V)} < \infty\}$, for $0 < \alpha \leq 1$.
$C^{1,\alpha}(V)$	$\{\phi \in BC(V) \cap C^1(V) : \nabla\phi \in C^{0,\alpha}(V)\}$, for $0 < \alpha \leq 1$.
$\lVert\cdot\rVert_{L^p(V)}$	$\lVert\psi\rVert_{L^p(V)} := \left(\int_V \lvert\psi\rvert^p \mathrm{d}s\right)^{\frac{1}{p}}$,
$\lVert\cdot\rVert_p$	abbreviation for $\lVert\cdot\rVert_{L^p(\mathbb{R})}$.
$\lVert\cdot\rVert_{\infty,V}$	$\lVert\psi\rVert_{\infty,V} := \sup_{x\in V} \lvert\psi(x)\rvert$.
$\lVert\cdot\rVert_\infty$	abbreviation for $\lVert\cdot\rVert_{\infty,\mathbb{R}}$.
$\lVert\cdot\rVert_{C^{0,\alpha}(V)}$	$\lVert\phi\rVert_{C^{0,\alpha}(V)} := \lVert\phi\rVert_\infty + \sup_{x,y\in V, x\neq y}\left[\frac{\lvert\phi(x)-\phi(y)\rvert}{\lvert x-y\rvert^\alpha}\right]$, for $0 < \alpha \leq 1$.
$\lVert\cdot\rVert_{C^{1,\alpha}(V)}$	$\lVert\phi\rVert_{C^{1,\alpha}(V)} := \lVert\phi\rVert_\infty + \lVert\phi'\rVert_{C^{0,\alpha}(V)}$, for $0 < \alpha \leq 1$.
Γ	$\{(x_1, f(x_1))\mid x_1 \in \mathbb{R}\}$.
D	$\{(x_1, x_2)\mid x_2 > f(x_1)\}$.
Γ_h	$\{x \in \mathbb{R}^2 : x_2 = h\}$ (page 29).
U_h	$\{x \in \mathbb{R}^2 : x_2 > h\}$ (page 29).
γ^*	See page 43.
Γ_{x^*}	See page 44.
G_0	See page 35.
G^*	See page 48.
G_ϵ	See page 56.
Γ^0	See page 35.
$B_\epsilon(x)$	$\{y \in \mathbb{R}^2 : \lvert x - y\rvert < \epsilon\}$.

Table 1.1: Table of notation

Chapter 2

Hilbert Spaces and Tikhonov Regularisation

2.1 Hilbert Spaces

In this section we present the concept of a Hilbert space along with some of its properties required to describe and analyse the procedure used in many inverse problems known as Tikhonov Regularisation, described in section 2.2 below. Throughout this section we use [30, 34, 3, 17, 27] as general references and Σ (the set of scalars) is either $\mathbb{R}$ or $\mathbb{C}$.

Definition 2.1.1 *For a linear space V, a* norm $\|\cdot\|$ *on V is a function from V to $\mathbb{R}$ with the following properties.*

(a) $\|f\| \geq 0$ *for all* $f \in V$.

(b) $\|cf\| = |c|\|f\|$ *for all* $f \in V$ *and* $c \in \Sigma$.

(c) $\|f\| = 0 \iff f = 0$ *for all* $f \in V$.

(d) $\|f + g\| \leq \|f\| + \|g\|$ *for all* $f, g \in V$. *(The triangle inequality).*

The space V equipped with the norm is called a normed space. Every normed space is also a metric space with metric $d(f, g) := \|f - g\|$.

Definition 2.1.2 *An* inner product space *is a vector space V together with a function (the inner product) from $V \times V$ to Σ, denoted $(,)$, satisfying:*

(a) $(f + g, h) = (f, h) + (g, h)$ *for all* $f, g, h \in V$.

(b) $(cf, g) = c(f, g)$ *for all* $f, g \in V$ *and* $c \in \Sigma$.

(c) $\overline{(f, g)} = (g, f)$ *for all* $f, g \in V$.

(d) $0 \leq (f, f)$ *for all* $f \in V$.

(e) $(f, f) = 0 \iff f = 0$.

Lemma 2.1.1 *[34] For an inner product there holds the Cauchy-Schwarz inequality*

$$|(f,g)|^2 \leq (f,f)(g,g)$$

for all $f, g \in V$.

Any inner product space is also a normed space by defining

$$\|f\| = \sqrt{(f,f)}. \tag{2.1}$$

That $\|.\|$ defined by (2.1) satisfies the triangle inequality follows from the Cauchy-Schwarz inequality and the identity

$$\|f+g\|^2 = \|f\|^2 + 2\Re(f,g) + \|g\|^2. \tag{2.2}$$

When we talk about convergence in an inner product space we will intend, unless we specify otherwise, this convergence to be convergence with respect to the metric induced by the norm (2.1).

Definition 2.1.3 *An inner product space* X *is called a* Hilbert Space *if it is complete i.e. if every Cauchy sequence in* X *converges.*

Theorem 2.1.1 *[30] Let* $A : X \to Y$ *be a linear and bounded operator between Hilbert spaces. Then there exists one and only one linear bounded operator* $A^* : Y \to X$ *with the property*

$$(Ax, y) = (x, A^*y) \tag{2.3}$$

for all $x \in X$, $y \in Y$. *This operator* $A^* : Y \to X$ *is called the adjoint operator to* A.

Note that equation (2.3) implies that $(A^*y, x) = (y, Ax)$ and so A is the adjoint of A^*, in symbols $(A^*)^* = A$.

Lemma 2.1.2 *Let* S *be a linear subspace of* X. *Then* S *is dense in* X *if and only if*

$$x \in X,\ (x,z) = 0,\ \forall z \in S \Rightarrow x = 0. \tag{2.4}$$

Proof. (i) If S is dense in X, then for all $x \in X$, $\epsilon > 0$, there exists a $y \in S$ such that $\|x - y\| < \epsilon$. So if $(x, z) = 0 \; \forall z \in S$ then

$$\begin{aligned} (x, y) = 0 \quad &\Leftrightarrow \quad (x, x) = (x, x - y) \\ &\Rightarrow \quad \|x\|^2 \leq \|x\|\epsilon \\ &\Rightarrow \quad \|x\| \leq \epsilon. \end{aligned}$$

Since $\epsilon > 0$ is arbitrary it follows that $x = 0$.
(ii) Next we show that if (2.4) holds then S is dense in X. Note that $\overline{S}$ is a closed linear subspace of X. If S is not dense in X then $\overline{S} \neq X$. Let $x^* \in X \backslash \overline{S}$. Then, by the projection theorem [30], $x^* = s + x$ where $s \in \overline{S}$ and $x \in \overline{S}^{\perp}$, i.e. $(x, z) = 0$ for all $z \in \overline{S}$, and, since $x^* \notin \overline{S}$, $x \neq 0$. □

Theorem 2.1.2 *$A^* : Y \to X$ is injective if and only if $A(X)$ is dense in Y.*

Proof. First note that $A^* : Y \to X$ is injective if and only if

$$y \in Y, \; A^* y = 0 \Rightarrow y = 0.$$

This is equivalent to

$$\begin{aligned} y \in Y, \quad (A^* y, x) = 0 \; \forall x \in X \quad &\Rightarrow y = 0 \\ \Leftrightarrow y \in Y, \quad (y, Ax) = 0 \; \forall x \in X \quad &\Rightarrow y = 0 \\ \Leftrightarrow y \in Y, \quad (y, z) = 0 \; \forall z \in A(X) \quad &\Rightarrow y = 0. \end{aligned}$$

The required result follows from Lemma 2.1.2. □

Definition 2.1.4 *A bounded linear operator $A : X \to X$ on a Hilbert space X is called* strictly coercive *if there exists a constant $c > 0$ such that*

$$\Re(Ax, x) \geq c\|x\|^2$$

for all $x \in X$.

Lemma 2.1.3 *[34]**(Lax-Milgram)** In a Hilbert space X a strictly coercive operator $A : X \to X$ has a bounded inverse $A^{-1} : X \to X$.*

The usual convergence of a sequence in a Hilbert space, i.e. that $x_n \to x$ if and only if $\|x_n - x\| \to 0$, is often called strong convergence to distinguish it from weak convergence defined as follows.

Definition 2.1.5 *A sequence (x_n) in a Hilbert space X is said to converge weakly to $x \in X$ if*

$$(x_n, z) \to (x, z) \qquad \text{as } n \to \infty, \forall z \in X,$$

i.e. if

$$(x_n - x, z) \to 0 \qquad \text{as } n \to \infty, \forall z \in X.$$

This is written as $x_n \rightharpoonup x$.

To establish a key property of weak convergence we use the Banach-Steinhaus theorem.

Theorem 2.1.3 *[17]**(Banach-Steinhaus)** Suppose that E is a Banach space and F a normed space. Let $\{A_i\}_{i \in I}$ be a family of continuous linear operators from E into F. If*

$$\sup_{i \in I} \|A_i x\|_F < \infty$$

for each $x \in E$, then

$$\sup_{i \in I} \|A_i\| < \infty.$$

We note the following properties of weak convergence.

Theorem 2.1.4 *Let X be a Hilbert space and $(x_n) \subset X$, $x, y \in X$. Then*

(i) $x_n \to x \Rightarrow x_n \rightharpoonup x$.

(ii) *If* $x_n \rightharpoonup x$ *and* $x_n \rightharpoonup y$ *then* $x = y$.

(iii) *If* $x_n \rightharpoonup x$ *then* (x_n) *is bounded, i.e.*

$$\sup_n \|x_n\| < \infty.$$

(iv) *If* $(y_n) \subset X$ *is bounded then* (y_n) *has a weakly convergent subsequence, i.e. there exists* $y \in X$ *and a subsequence* (y_{n_m}) *such that* $(y_{n_m}) \rightharpoonup y$.

(v) *If* $x_n \rightharpoonup x$ *and* $\|x_n\| \to \|x\|$ *then* $x_n \to x$.

(vi) *If* $x_n \rightharpoonup x$ *and* $\|x_n\| \leq \|x\|$ *then* $x_n \to x$.

(vii) *If* K *is a bounded linear operator on* X *and* $x_n \rightharpoonup x$ *then* $Kx_n \rightharpoonup Kx$.

Proof.

(i) This follows since $|(x_n - x, z)| \leq \|x_n - x\|\|z\|$.

(ii) If $x_n \rightharpoonup x$ then $(x_n - y, x - y) \to (x - y, x - y) = \|x - y\|^2$. If also $x_n \rightharpoonup y$ then $(x_n - y, x - y) \to 0$, so $x = y$.

(iii) For each $n \in \mathbb{N}$ define $\tilde{x}_n : X \to \mathbb{C}$ by

$$\tilde{x}_n(z) = \overline{(x_n, z)}, \qquad z \in X.$$

Then it is easy to see that $\tilde{x}_n$ is linear. It is also bounded, in fact, for all $z \in X$,

$$|\tilde{x}_n(z)| \leq \|x_n\|\|z\|,$$

by the Cauchy-Schwarz inequality, so that $\|\tilde{x}_n\| \leq \|x_n\|$. On the other hand $\tilde{x}_n(x_n) = \|x_n\|^2$, so that $\|\tilde{x}_n\| \geq \|x_n\|$. Thus

$$\|\tilde{x}_n\| = \|x_n\|.$$

Further, for every $z \in X$,

$$\tilde{x}_n(z) = \overline{(x_n, z)} \to (x, z)$$

as $n \to \infty$, so that

$$\sup_n |\tilde{x}_n(z)| < \infty, \qquad z \in X.$$

Since X is a Hilbert space, it follows from the Banach-Steinhaus theorem that

$$\sup_n \|x_n\| = \sup_{n\in\mathbb{N}} \|\tilde{x}_n\| < \infty,$$

i.e. (x_n) is bounded.

(iv) For a proof see [57, Theorem 2.C].

(v) From (2.2)

$$\|x_n - x\|^2 = \|x_n\|^2 - 2\Re(x_n, x) + \|x\|^2. \tag{2.5}$$

As $n \to \infty$, $(x_n, x) \to (x, x) = \|x\|^2$ and $\|x_n\| \to \|x\|$. Thus $\|x_n - x\|^2 \to 0$.

(vi) If $\|x_n\| \leq \|x\|$ and $x_n \rightharpoonup x$ then from (2.5),

$$\|x_n - x\|^2 \leq 2(\|x\|^2 - \Re(x_n, x)) \to 0$$

as $n \to \infty$.

(vii) For every $z \in X$,

$$(Kx_n - Kx, z) \;=\; (K(x_n - x), z) = (x_n - x, K^*z) \to 0$$

as $n \to \infty$.

□

2.2 Tikhonov Regularisation

Many inverse problems can be formulated as operator equations of the form

$$Kx = y, \tag{2.6}$$

with $x \in X, y \in Y$ and X and Y Hilbert spaces. If $K : X \to Y$ is bijective, in which case $K^{-1} : Y \to X$ exists and, by the open mapping theorem [39], is bounded, then equation (2.6) is well posed, that is equation (2.6) has exactly one solution $x \in X$ for every $y \in Y$ and the solution depends continuously on y since

$$\|x\| \leq C\|y\| \tag{2.7}$$

where $C = \|K^{-1}\|$. In many applications, for example those mentioned in section 4.1, while K is injective it is not surjective so that a solution to (2.6) does not exist for all $y \in Y$. More crucially K^{-1} is not bounded, i.e there does not exist a constant $C > 0$ for which (2.7) holds for all $y \in K(X)$. We shall see shortly that it is possible, when K^{-1} is not bounded but K has dense range, to construct a family of bounded approximations to K^{-1} satisfying the following strategy.

Definition 2.2.1 *[30] A* regularisation strategy *for $K : X \to Y$ is a family of linear bounded operators $R_\alpha : Y \to X$ for $\alpha > 0$ such that*

$$R_\alpha y \to K^{-1} y \qquad\qquad \text{as } \alpha \to 0$$

for all $y \in K(X)$.

In this section we show that Tikhonov regularisation, a procedure to cope with ill-posedness, is a regularisation stategy in the above sense. In contrast to the treatment in [30, 20, 34, 14] we assume nowhere in our analysis that K is a compact operator, assuming only that K is a linear bounded, injective operator with dense range.

When it is not clear whether a solution to (2.6) exists or not it is perhaps natural, as a first attempt at computing an approximate solution, to try and find x to minimise $\|Kx - y\|$.

Theorem 2.2.1 *[30] For every $y \in Y$, $\hat{x} \in X$ satisfies $\|K\hat{x} - y\| \leq \|Kx - y\|$ for all $x \in X$ if and only if $\hat{x} \in X$ solves the normal equation*

$$K^*K\hat{x} = K^*y, \tag{2.8}$$

where $K^* : Y \to X$ is the adjoint of K.

Equation (2.8) is ill-posed if (2.6) is ill-posed. But this ill-posedness can be removed by perturbing it slightly, replacing it with

$$\alpha x^\alpha + K^*Kx^\alpha = K^*y$$

for some small $\alpha > 0$.

Theorem 2.2.2 *[30] If $\alpha > 0$, the operator $(\alpha I + K^*K) : X \to X$ is boundedly invertible, with $\|(\alpha I + K^*K)^{-1}\| \leq \alpha^{-1}$.*

Proof. Let $A_\alpha = \alpha I + K^*K$. Then A_α is strictly coercive since, for all $x \in X$,

$$\begin{aligned} (A_\alpha x, x) &= \alpha\|x\|^2 + (K^*Kx, x) \\ &= \alpha\|x\|^2 + (Kx, Kx) \\ &= \alpha\|x\|^2 + \|Kx\|^2 \\ &\geq \alpha\|x\|^2. \end{aligned} \tag{2.9}$$

By Lemma 2.1.3 A_α has a bounded inverse. Further, if $y \in Y$ and $x = A_\alpha^{-1}y$, then, by (2.9), $\alpha\|x\|^2 \leq (y, x) \leq \|y\|\|x\|$ so $\|A_\alpha^{-1}y\| = \|x\| \leq \alpha^{-1}\|y\|$. Hence $\|A_\alpha^{-1}\| \leq \alpha^{-1}$. □

Given $K : X \to Y$, a linear bounded operator, and $y \in Y$, define the *Tikhonov functional* by

$$J_\alpha(x) := \|Kx - y\|^2 + \alpha\|x\|^2 \qquad \text{for } x \in X. \tag{2.10}$$

Theorem 2.2.3 *[30] For $\alpha > 0$ the Tikhonov functional J_α, defined by equation (2.10), has a unique minimum $x^\alpha \in X$ given as the unique solution of the second kind equation*

$$\alpha x^\alpha + K^*Kx^\alpha = K^*y. \tag{2.11}$$

The solution of equation (2.11) can be written as $x^\alpha = R_\alpha y$ with

$$R_\alpha := (\alpha I + K^*K)^{-1}K^* : Y \to X. \tag{2.12}$$

We call $x^\alpha = R_\alpha y$ the *Tikhonov regularisation solution* of (2.6) with *regularisation parameter* α.

Lemma 2.2.1 *For $\alpha > 0$ the operator R_α is bounded with*

$$\|R_\alpha\| \leq \frac{1}{\sqrt{\alpha}}.$$

Proof. By Theorem 2.2.2, R_α is bounded with $\|R_\alpha\| \leq \alpha^{-1}\|K^*\|$. To get a sharper bound note that, since $x^\alpha = R_\alpha y$ minimises $J_\alpha(x)$,

$$\begin{aligned} J_\alpha(x^\alpha) &\leq J_\alpha(0) \\ \Rightarrow \alpha\|x^\alpha\|^2 + \|Kx^\alpha - y\|^2 &\leq \|y\|^2 \\ \Rightarrow \alpha\|x^\alpha\|^2 &\leq \|y\|^2 \\ \Rightarrow \sqrt{\alpha}\|R_\alpha y\| &\leq \|y\| \\ \Rightarrow \|R_\alpha\| &\leq \frac{1}{\sqrt{\alpha}}. \end{aligned}$$

□

The proof of the next theorem is based, in large part, on that of [30, Theorem 2.16].

Theorem 2.2.4 *[30] Suppose that K is injective with dense range. If $y \in Y$, $y \neq 0$, $\alpha > 0$, and x^α is the unique solution of equation (2.11), then x^α depends continuously on α. The mapping $\alpha \to \|x^\alpha\|$ is strictly monotonically decreasing and*

$$\lim_{\alpha\to\infty} \|x^\alpha\| = 0.$$

The mapping $\alpha \to \|Kx^\alpha - y\|$ is strictly monotonically increasing and

$$\lim_{\alpha\to 0} \|Kx^\alpha - y\| = 0.$$

Proof. This is done in 6 steps.

(i) From Lemma 2.2.1 we see that

$$\|x^\alpha\| = \|R_\alpha y\| \leq \|R_\alpha\|\|y\| \leq \frac{1}{\sqrt{\alpha}}\|y\|.$$

This proves that $x^\alpha \to 0$ as $\alpha \to \infty$.

(ii) If we choose $\alpha > 0$ and $\beta > 0$ and subtract equation (2.11) for β from (2.11) for α then

$$\alpha(x^\alpha - x^\beta) + K^*K(x^\alpha - x^\beta) + (\alpha - \beta)x^\beta = 0. \tag{2.13}$$

Taking the inner product with $(x^\alpha - x^\beta)$ gives

$$\alpha\|x^\alpha - x^\beta\|^2 + \|K(x^\alpha - x^\beta)\|^2 = (\beta - \alpha)(x^\beta, x^\alpha - x^\beta). \tag{2.14}$$

From this equation we conclude that

$$\alpha\|x^\alpha - x^\beta\|^2 \leq |\beta - \alpha||(x^\beta, x^\alpha - x^\beta)| \leq |\beta - \alpha|\|x^\beta\|\|x^\alpha - x^\beta\|,$$

i.e.

$$\alpha\|x^\alpha - x^\beta\| \leq |\beta - \alpha|\|x^\beta\| \leq |\beta - \alpha|\frac{\|y\|}{\sqrt{\beta}}.$$

This proves the continuity of the mapping $\alpha \longmapsto x^\alpha$.

(iii) As $y \neq 0$ and K has dense range it follows that K^* is injective by Theorem 2.1.2, and so $K^*y \neq 0$. From (2.11) it follows that $x^\beta \neq 0$ for $\beta > 0$. Then, if $\alpha > 0$ and $\alpha \neq \beta$, it follows from (2.13) that $x^\alpha \neq x^\beta$ and so, from (2.14), that $(\beta - \alpha)(x^\beta, x^\alpha - x^\beta) > 0$.

(iv) Now let $\beta > \alpha > 0$. From (iii) we see that $(x^\beta, x^\alpha - x^\beta) > 0$. Thus $\|x^\beta\|^2 < (x^\beta, x^\alpha) \leq \|x^\beta\|\|x^\alpha\|$,i.e.$\|x^\beta\| < \|x^\alpha\|$, which proves strict monotonicity of $\alpha \longmapsto \|x^\alpha\|$.

(v) Taking the inner product of (2.11) for x^β with $(x^\alpha - x^\beta)$ gives

$$\beta(x^\beta, x^\alpha - x^\beta) + (Kx^\beta - y, K(x^\alpha - x^\beta)) = 0.$$

Now let $\alpha > \beta$. From (iii) we see that $(x^\beta, x^\alpha - x^\beta) < 0$, so that

$$0 < (Kx^\beta - y, K(x^\alpha - x^\beta)) = (Kx^\beta - y, Kx^\alpha - y) - \|Kx^\beta - y\|^2.$$

The Cauchy-Schwarz inequality yields $\|Kx^\beta - y\| < \|Kx^\alpha - y\|$. This shows strict monotonicity of the mapping $\alpha \longmapsto \|Kx^\alpha - y\|$.

(vi) Finally, let $\epsilon > 0$. Since the range of K is dense in Y there exists $x \in X$ such that $\|Kx - y\|^2 \leq \epsilon^2/2$. Choosing α_0 such that $\alpha_0\|x\|^2 \leq \epsilon^2/2$ we see that

$$\|Kx^\alpha - y\|^2 \leq J_\alpha(x^\alpha) \leq J_\alpha(x) \leq \epsilon^2.$$

Thus and by (v), $\|Kx^\alpha - y\| \leq \epsilon$ for all $\alpha \leq \alpha_0$.

□

If K is injective with dense range then from Theorem 2.2.4 we have that, for $y \neq 0$, the mapping $\alpha \to \|x^\alpha\|$ is strictly decreasing. Therefore either

$$\|x^\alpha\| \to \infty \qquad \text{as } \alpha \to 0$$

or

$$C := \lim_{\alpha \to 0} \|x^\alpha\|$$

exists and $\|x^\alpha\| < C$, $\alpha > 0$.

Theorem 2.2.5 *Suppose that K is injective with dense range. If $y \in K(X)$ then $\lim_{\alpha\to 0}\|x^\alpha\|$ exists and furthermore $x^\alpha \to x := K^{-1}y$ as $\alpha \to 0$. If $y \notin K(X)$ then $\|x^\alpha\| \to \infty$ as $\alpha \to 0$.*

Proof. First we point out that whenever $y \in K(X)$, defining $x^* = K^{-1}y$,

$$J(x^\alpha) \leq J(x^*)$$

$$\begin{aligned} \Rightarrow \alpha\|x^\alpha\|^2 + \|Kx^\alpha - y\|^2 &\leq \alpha\|x^*\|^2 \\ \Rightarrow \|x^\alpha\| &\leq \|x^*\| \end{aligned} \tag{2.15}$$

so that $\lim_{\alpha\to 0}\|x^\alpha\|$ exists.

Conversely suppose $C := \lim_{\alpha\to 0}\|x^\alpha\|$ exists and let $(\alpha_n) \subset (0,\alpha)$ be a null sequence (i.e. $\alpha_n \to 0$ as $n \to \infty$). Then

$$\|x^{\alpha_n}\| \to C \qquad \text{as } n \to \infty$$

so that (x^{α_n}) is bounded. By Theorem 2.1.4 (iv) (x^{α_n}) has a weakly convergent subsequence, $(x^{\alpha_{n_m}})$. For some $x^* \in X$, $x^{\alpha_{n_m}} \rightharpoonup x^* \in X$ and, by Theorem 2.1.4 (vii), $Kx^{\alpha_{n_m}} \rightharpoonup Kx^*$. On the other hand, by Theorem 2.2.4, $Kx^\alpha \to y$ as $\alpha \to 0$ and so $Kx^{\alpha_{n_m}} \to y$. Therefore, by Theorem 2.1.4 (i), $Kx^{\alpha_{n_m}} \rightharpoonup y$, and so, by (ii), $Kx^* = y$, so that $y \in K(X)$. Since K is injective x^* is the unique solution of $Kx = y$ in X.

We have shown that every null sequence (α_n) has a subsequence (α_{n_m}) such that $x^{\alpha_{n_m}} \rightharpoonup x^* = K^{-1}y$. It follows that $x^\alpha \rightharpoonup x^*$ by the following argument. Suppose this does not hold. Then there exists a null sequence (α_n) and a $z \in X$ such that

$$(x^{\alpha_n} - x^*, z) \not\to 0.$$

Further, we can choose the null sequence so that, for some $\epsilon > 0$,

$$|(x^{\alpha_n} - x^*, z)| \geq \epsilon, \qquad n \in \mathbb{N}.$$

It then follows that (α_n) has no subsequence (α_{n_m}) such that $x^{\alpha_{n_m}} \rightharpoonup x^*$, which is a contradiction. Hence $x^\alpha \rightharpoonup x^* = K^{-1}y$ and, since (2.15) holds, by Theorem 2.1.4 (v), $x^\alpha \to x^*$. □

Corollary 2.2.2 *If K is injective with dense range then Tikhonov regularisation is a regularisation strategy in the sense of Definition 2.2.1.*

Proof. By Lemma 2.2.1, R_α is bounded for every $\alpha > 0$. By Theorem 2.2.5, if $y \in K(X)$, then

$$x^\alpha := R_\alpha y \to x := K^{-1}y \qquad \text{as } \alpha \to 0.$$

□

Chapter 3

The Direct Scattering Problem

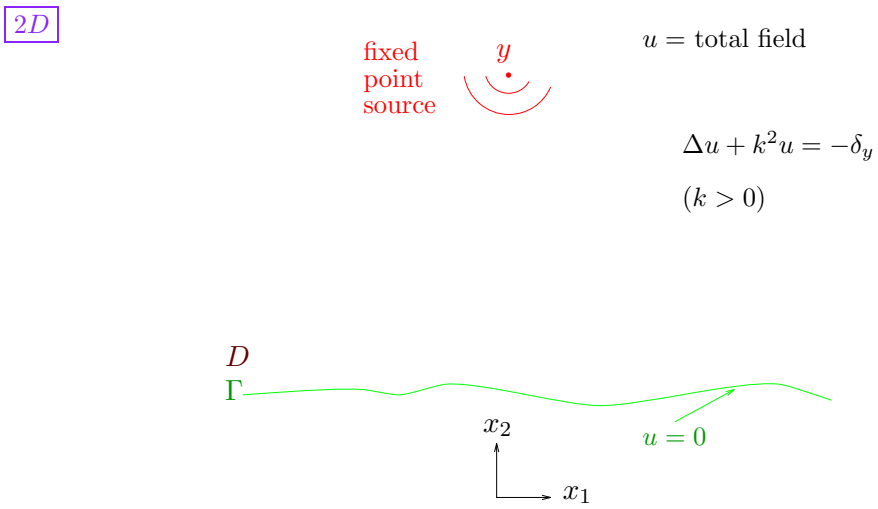

Figure 3.1: The direct problem geometry

3.1 The Main Boundary Value Problem

Consider the problem of scattering of a time-harmonic electromagnetic wave incident on an infinite perfectly conducting boundary, Γ. The region above Γ consists of a homogeneous, isotropic, non-magnetic, dielectric material of (constant) electric permittivity $\epsilon > 0$ and magnetic permeability $\mu > 0$. We adopt a Cartesian coordinate system $Ox_1x_2x_3$, and assume that the incident field, scattering surface and medium are invariant in the x_3 direction, so that the problem is two-dimensional. We restrict our attention to the case when the incident electromagnetic field is that from a time harmonic ($e^{-i\omega t}$ time dependence) monopole source in TE polarization. Thus the electric field E points along the x_3 axis. Define the scattering surface, Γ, for some $f \in C^{1,1}(\mathbb{R})$, by

$$\Gamma = \{(x_1, f(x_1))|\ x_1 \in \mathbb{R}\}. \tag{3.1}$$

Since $f \in C^{1,1}(\mathbb{R})$ it holds that, for some constants $f_-, f_+ \in \mathbb{R}$,

$$f_- \leq f(x_1) \leq f_+, \qquad x_1 \in \mathbb{R}. \tag{3.2}$$

Let the region above Γ be defined by

$$D := \{(x_1, x_2) |\ x_2 > f(x_1)\}. \tag{3.3}$$

Electromagnetic wave propagation is governed by the time harmonic Maxwell equations

$$\nabla \times E - i\omega\mu H = 0, \tag{3.4}$$

$$\nabla \times H + i\omega\epsilon E = 0, \tag{3.5}$$

where E and H are the electric field and magnetic field, respectively. Since the surface is perfectly conducting the appropriate boundary condition is that the tangential component of the electric field E vanishes, i.e.

$$n \times E = 0, \tag{3.6}$$

where n is the unit normal at the boundary. Using the notations $x = (x_1, x_2), y = (y_1, y_2) \in \mathbb{R}^2$, the electric field at $x \in D$ when the incident field is that due to a monopole source of unit strength at $y \in D$ is given by $E = (0, 0, G(x, y))$. It follows from equations (3.4) and (3.5) and the boundary condition (3.6) that $u := G(\cdot, y)$ satisfies the inhomogeneous Helmholtz equation,

$$\Delta u + k^2 u = -\delta_y \tag{3.7}$$

in D, with $k^2 = \omega^2\mu\epsilon$, and the Dirichlet boundary condition

$$u = 0 \text{ on } \Gamma$$

(see Figure 3.1). To ensure that the scattered field propagates outwards from the scattering surface and source position, a radiation condition must be imposed. Standard radiation conditions for scattering problems for the Helmholtz equation are the Sommerfeld radiation conditions. We shall say that u satisfies the Sommerfeld radiation conditions in D if

$$u(x) = O(r^{-\frac{1}{2}}),$$
$$\frac{\partial u(x)}{\partial r} - iku(x) = o(r^{-\frac{1}{2}}),$$

as $r := |x| \to \infty$, uniformly in $\hat{x} := x/|x|$.

Let

$$\Phi(x,y) := \frac{i}{4} H_0^{(1)}(k|x-y|), \qquad x, y \in \mathbb{R}^2, x \neq y. \tag{3.8}$$

Then $\Phi(\cdot, y)$ is the unique solution of (3.7) in $\mathbb{R}^2$ which satisfies the Sommerfeld radiation conditions. An alternative radiation condition for problems of scattering by infinite rough surfaces is the so-called upwards propagating radiation condition (UPRC) introduced in [9]. Define the infinite straight line Γ_h, for $h \in \mathbb{R}$, by

$$\Gamma_h := \{(x_1, h) | x_1 \in \mathbb{R}\}, \tag{3.9}$$

and the half plane above Γ_h by

$$U_h := \{(x_1, x_2) \in \mathbb{R}^2 |\ x_2 > h\}. \tag{3.10}$$

Following [9] we say that $u : D \to \mathbb{C}$ satisfies the UPRC in D if, for some $h \geq f_+$ and $\phi \in L^\infty(\Gamma_h)$,

$$u(x) = 2 \int_{\Gamma_h} \frac{\partial \Phi(x,y)}{\partial y_2} \phi(y) \mathrm{ds}(y), \qquad x \in U_h. \tag{3.11}$$

Remark 3.1.1 *It is shown in [9] that if $u \in C^2(D)$ satisfies the Helmholtz equation in D and the Sommerfeld radiation conditions then u satisfies the UPRC.*

We note that, for the problem we are considering, $\Phi(\cdot, y)$ is the incident field, that is the electric field in the absence of the scattering surface. Let $U^s(x,y) := G(x,y) - \Phi(x,y)$ denote the scattered part of the electric field. Then our problem of scattering by an infinite rough surface can be formulated as the following Dirichlet boundary-value problem for the scattered field $v := U^s(\cdot, y)$.

BVP1 (The Dirichlet Problem). *Find $v \in C^2(D) \cap C(\overline{D})$ such that*

$$\begin{aligned} \Delta v + k^2 v = 0 \quad & \text{in } D, \\ v = -\Phi(., y) \quad & \text{on } \Gamma, \\ v(x) = O(r^{-\frac{1}{2}}), & \\ \frac{\partial v(x)}{\partial r} - ikv(x) = o(r^{-\frac{1}{2}}), & \end{aligned}$$

as $r := |x| \to \infty$, *uniformly in* $\hat{x} = x/|x|$.

Remark 3.1.2 *We assume in BVP1 only that* $v \in C(\overline{D})$, *but note that, since* Γ *is of class* $C^{1,1}$ *and* $v + \Phi(\cdot, y) \in C^2(D\backslash\{y\}) \cap C(\overline{D}\backslash\{y\})$ *and satisfies the Helmholtz equation in* $D\backslash\{y\}$ *with zero Dirichlet data on* Γ, *it follows by standard elliptic regularity estimates up to the boundary [22] that in fact* $G(\cdot, y) = v + \Phi(\cdot, y) \in C^1(\overline{D}\backslash\{y\})$ *so that* $v \in C^1(\overline{D})$.

Within this section we look at two boundary value problems, which are vital to the inverse problem described in Chapter 4. The first direct scattering problem, which we are interested in throughout this thesis, is **BVP1**. We want to show the existence and uniqueness of solution to this problem and that the solution is continuously dependent upon the incident field values given on the surface Γ. In order to do this we first note that it follows from Remark 3.1.1 that if v satisfies BVP1 then v satisfies the following Dirichlet BVP with boundary data $g = -\Phi(\cdot, y) \in BC(\Gamma)$.

BVP2 *Given* $g \in BC(\Gamma)$ *determine* $v \in C^2(D) \cap C(\overline{D})$ *such that:*

$$\begin{aligned} \Delta v + k^2 v = 0 \quad & \text{in } D, \\ v = g \quad & \text{on } \Gamma, \\ \sup_{x \in D} x_2^{\beta} |v(x)| < \infty, \quad & \text{for some } \beta \in \mathbb{R}, \\ & v \text{ satisfies the UPRC in } D. \end{aligned}$$

For some $c_1 > 0$ let $B_1 := \{f \in C^{1,1}(\mathbb{R}) | \|f\|_{C^{1,1}(\mathbb{R})} \leq c_1\}$. The next two results follow from [8].

Theorem 3.1.1 *BVP2 has exactly one solution.*

Theorem 3.1.2 *For some constant* $C > 0$ *depending only on* c_1 *and* k, *the solution,* v, *of BVP2 satisfies*

$$|v(x)| \leq C(1 + x_2 - f_-)^{\frac{1}{2}} \|g\|_{\infty}, \qquad x \in \overline{D},$$

for all $f \in B_1$, $g \in BC(\Gamma)$.

From Theorem 3.1.1 it follows immediately that BVP1 has at most one solution. Moreover it is pointed out in [7] that if $g = -\Phi(\cdot, y)$ then the solution to BVP2 also satisfies the Sommerfeld radiation conditions. Thus the following result holds.

Theorem 3.1.3 *BVP1 has exactly one solution, which is the unique solution of BVP2 with* $g = -\Phi(\cdot, y)$.

Theorem 3.1.4 ***(Reciprocity Relation)*** *For* $x, y \in D$, $x \neq y$, *we have* $G(x, y) = G(y, x)$.

Proof. Define, for $\epsilon, R > 0$, the region $D_{R,\epsilon} := \{z \in D : |z| < R, |z - x| > \epsilon, |z - y| > \epsilon\}$. Choose ϵ sufficiently small so that $\overline{B_\epsilon(x)} \subset D$, $\overline{B_\epsilon(y)} \subset D$ and $\overline{B_\epsilon(x)} \cap \overline{B_\epsilon(y)} = \emptyset$ and choose $R > |x| + |y| + \epsilon$. Then, since $G(\cdot, y), G(\cdot, x) \in C^2(D_{R,\epsilon}) \cap C^1(\overline{D_{R,\epsilon}})$ by Remark 3.1.2, we can apply Green's second theorem in $D_{R,\epsilon}$ to give

$$0 = \int_{\partial D_{R,\epsilon}} \Big\{ \frac{\partial G(\cdot, y)}{\partial n} G(\cdot, x) - \frac{\partial G(\cdot, x)}{\partial n} G(\cdot, y) \Big\} \mathrm{ds}.$$

Letting $R \to \infty$, and defining $D^\epsilon := D \backslash \{\overline{B_\epsilon(x)} \cup \overline{B_\epsilon(y)}\}$, then, since $G(\cdot, x)$ and $G(\cdot, y)$ satisfy the Sommerfeld radiation conditions, it follows that

$$0 = \int_{\partial D^\epsilon} \Big\{ \frac{\partial G(\cdot, y)}{\partial n} G(\cdot, x) - \frac{\partial G(\cdot, x)}{\partial n} G(\cdot, y) \Big\} \mathrm{ds}.$$

Since $G(\cdot, x) = G(\cdot, y) = 0$ on Γ we have

$$0 = \int_{\partial B_\epsilon(y) \cup \partial B_\epsilon(x)} \Big\{ \frac{\partial G(\cdot, y)}{\partial n} G(\cdot, x) - \frac{\partial G(\cdot, x)}{\partial n} G(\cdot, y) \Big\} \mathrm{ds}. \tag{3.12}$$

Applying Green's second theorem to $U^s(\cdot, y)$ and $G(\cdot, x)$ in $B_\epsilon(y)$ gives

$$0 = \int_{\partial B_\epsilon(y)} \Big\{ \frac{\partial U^s(\cdot, y)}{\partial n} G(\cdot, x) - \frac{\partial G(\cdot, x)}{\partial n} U^s(\cdot, y) \Big\} \mathrm{ds}, \tag{3.13}$$

and then applying Green's second theorem in $B_\epsilon(x)$ gives

$$0 = \int_{\partial B_\epsilon(x)} \Big\{ \frac{\partial G(\cdot, y)}{\partial n} U^s(\cdot, x) - \frac{\partial U^s(\cdot, x)}{\partial n} G(\cdot, y) \Big\} \mathrm{ds}. \tag{3.14}$$

Now subtracting equations (3.14) and (3.13) from equation (3.12) and using Green's representation theorem [30] yields

$$\begin{aligned} 0 &= \int_{\partial B_\epsilon(y)} \Big\{ \frac{\partial \Phi(\cdot, y)}{\partial n} G(\cdot, x) - \frac{\partial G(\cdot, x)}{\partial n} \Phi(\cdot, y) \Big\} \mathrm{ds} \\ &+ \int_{\partial B_\epsilon(x)} \Big\{ \frac{\partial G(\cdot, y)}{\partial n} \Phi(\cdot, x) - \frac{\partial \Phi(\cdot, x)}{\partial n} G(\cdot, y) \Big\} \mathrm{ds} \\ &= G(y, x) - G(x, y). \end{aligned} \tag{3.15}$$

□

Now, for $h \in \mathbb{R}$, define

$$G_{1,h}(x, y) := \Phi(x, y) + \Phi(x, y'_h) + P(k(x - y'_h)), \quad x, y \in \overline{U_h}, \ \ x \neq y, \tag{3.16}$$

where

$$P(z) := \frac{e^{i|z|}}{\pi} \int_0^\infty \frac{t^{-\frac{1}{2}} e^{-|z|t} (1 + \gamma(1 + it))}{\sqrt{t - zi}(t - i(1 + \gamma))^2} \, \mathrm{dt}, \ \ z \in \overline{U_0},$$

with $\gamma := z_2/|z|$, and $y'_h = (y_1, 2h - y_2)$ the reflection of y in $\Gamma_h := \partial U_h$. It is shown in [5],[4] that $P \in C(\overline{U_0}) \cap C^\infty(\overline{U_0} \backslash \{0\})$ and satisfies the Helmholtz equation and Sommerfeld radiation conditions (with $k = 1$) in U_0. If $v := G_{1,h}(., y)$ we have that (see [4])

$$\begin{aligned} \Delta v + k^2 v &= -\delta_y \quad \text{in } U_h, \\ \frac{\partial v}{\partial x_2} + ikv &= 0 \quad \text{on } \Gamma_h, \end{aligned} \tag{3.17}$$

$$\left.\begin{aligned} v(x) &= O(r^{-\frac{1}{2}}) \\ \tfrac{\partial v(x)}{\partial r} - ikv(x) &= o(r^{-\frac{1}{2}}) \end{aligned}\right\} \text{ as } r := |x| \to \infty, \ \text{ uniformly in } \hat{x}. \tag{3.18}$$

Thus $G_{1,h}$ is the Green's function for the Helmholtz equation in the half-plane U_h which satisfies the impedance boundary condition (3.17). From [6], $G_{1,h}$ satisfies the bounds

$$|G_{1,h}(x,y)| \leq C(1+x_2-h)(1+y_2-h)|x-y|^{-\frac{3}{2}}, \quad x,y \in \overline{U_h}, \ x \neq y, \tag{3.19}$$

and

$$|\nabla_y G_{1,h}(x,y)| \leq C(1+x_2-h)(1+y_2-h)|x-y|^{-\frac{3}{2}}, \quad x,y \in \overline{U_h}, \ x \neq y, \tag{3.20}$$

for some constant $C > 0$ depending only on k, so that $G_{1,h}$ decays faster than required by the Sommerfeld radiation conditions, (3.18), if x_2 and y_2 stay close to the boundary Γ_h. Echoing earlier notation we define

$$U_1^s(x,y) := G(x,y) - G_{1,h}(x,y), \qquad x,y \in \overline{D}. \tag{3.21}$$

Then $U_1^s(\cdot,y)$ is the solution to the Dirichlet boundary value problem **BVP2** for boundary data $g = -G_{1,h}(\cdot,y)$ on Γ.

3.2 Two Other Boundary Value Problems

In this chapter so far we have discussed the main direct problem of concern in this thesis. The majority of the remainder of this thesis is concerned with the corresponding inverse problem but, in order to analyse the Point Source Method for this problem, we require results on two other boundary value problems.

The first of these is the impedance rough surface problem, which is required to complete the proof of Lemma 3.2.3. Let $n(x)$ stand for the unit normal at $x \in \Gamma$ pointing out of D and then denote $\mathcal{R}(D)$ as the set of functions $v \in C^2(D) \cap C(\overline{D})$ for which the normal derivative defined by

$$\frac{\partial v(x)}{\partial n} := \lim_{h \to 0+} n(x) \cdot \nabla v(x - hn(x))$$

exists for $x \in \Gamma$, with the convergence uniform in x on every compact subset of Γ. For $h > f_+$ let $D_h := D \backslash \overline{U}_h$.

BVP3 (The Impedance Rough Surface Problem). *Given $g \in BC(\Gamma)$, $\beta \in BC(\Gamma)$, determine $u \in \mathcal{R}(D)$ such that*

$$\begin{aligned} \Delta u + k^2 u &= 0 \qquad \text{in } D, \\ \frac{\partial u}{\partial n} + ik\beta u &= g \qquad \text{on } \Gamma, \\ \sup_{x \in D} x_2^a |u(x)| &< \infty, \qquad \text{for some } a \in \mathbb{R}, \\ u &\text{ satisfies the UPRC in } D, \end{aligned} \tag{3.22}$$

and, for some $\theta \in (0,1)$ and constant $C_\theta > 0$,

$$|\nabla u(x)| \;\leq\; C_\theta [x_2 - f(x_1)]^{\theta - 1}, \quad x \in D \backslash U_b, \tag{3.23}$$

where $b = f_+ + 1$.

Recall that $G_{1,h}$ is the impedance half-plane Green's function defined by equation (3.16). The following two theorems give an equivalent boundary integral equation formulation for **BVP3**.

Theorem 3.2.1 *[58] Let u be a solution of BVP3 and $h < \inf_{x_1 \in \mathbb{R}} f(x_1)$. Then*

$$u(x) = -\int_\Gamma \left[\frac{\partial G_{1,h}(x,y)}{\partial \upsilon(y)} - ik\beta(y) G_{1,h}(x,y) \right] u(y)\, ds(y) + \int_\Gamma G_{1,h}(x,y) g(y)\, ds(y), \; x \in D, \tag{3.24}$$

and

$$u(x) + 2\int_\Gamma \left[\frac{\partial G_{1,h}(x,y)}{\partial \upsilon(y)} - ik\beta(y) G_{1,h}(x,y) \right] u(y)\, ds(y) = 2\int_\Gamma G_{1,h}(x,y) g(y)\, ds(y), \; x \in \Gamma. \tag{3.25}$$

Theorem 3.2.2 *[58] If u satisfies (3.24) and (3.25) and $u|_\Gamma \in BC(\Gamma)$ then u satisfies the impedance problem BVP3 with $a = -1/2$ in (3.22) and with every $\theta \in (0,1)$ in (3.23).*

It has been shown in [58] that **BVP3** has at most one solution if $\Re\beta$ is strictly positive (the boundary is energy absorbing).

Theorem 3.2.3 *[58] If, for some $d > 0$, $\Re(\beta(x)) \geq d$ for all $x \in \Gamma$, then BVP3 has at most one solution.*

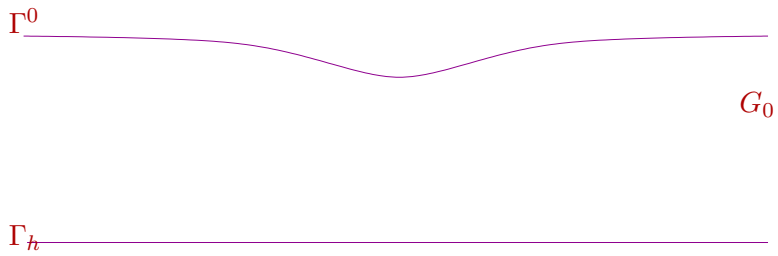

Figure 3.2: The duct-like region, G_0.

During the analysis of the inverse problem in Chapter 4, we need to study a further boundary value problem, namely **BVP5**. In section 4.1 we need to show that **BVP5** is uniquely solvable and to do this we need results for the following boundary value problem, **BVP4**.

Suppose that $h \in \mathbb{R}$, $f_0 \in C^{1,1}(\mathbb{R})$ with $\inf f_0 > h$, define

$$\Gamma^0 := \{(x_1, f_0(x_1)) : x_1 \in \mathbb{R}\}, \tag{3.26}$$

and consider the duct-like region $G_0 := \{(x_1, x_2) | h < x_2 < f_0(x_1), x_1 \in \mathbb{R}\}$, shown in Figure 3.2.

BVP4 (A Duct Problem). *Given $g \in L^2(\Gamma^0) \cap BC(\Gamma^0)$, find $u \in C^2(G_0) \cap C^1(G_0 \cup \Gamma_h) \cap BC(\overline{G_0})$ such that*

$$\begin{aligned} u &= g \quad \text{on } \Gamma^0, \\ \Delta u + k^2 u &= 0 \quad \text{in } G_0, \\ \frac{\partial u}{\partial x_2} + iku &= 0 \quad \text{on } \Gamma_h. \end{aligned}$$

Theorem 3.2.4 *The above boundary value problem has exactly one solution. Given $\epsilon > 0$, there exists a constant $C > 0$ such that for all $g \in L^2(\Gamma^0) \cap BC(\Gamma^0)$,*

$$|u(x)| \leq C \|g\|_{L^2(\Gamma^0)}, \quad h \leq x_2 \leq f_0(x_1) - \epsilon. \tag{3.27}$$

The proof of Theorem 3.2.4 depends on the following preliminary lemmas, of some interest in their own right.

Lemma 3.2.1 *The above boundary value problem has at most one solution.*

Proof. Let u_1 and u_2 be solutions to the above boundary value problem and define $u = u_1 - u_2$. Then u satisfies the above boundary value problem with $g = 0$. Further, by [58, Remark $C.1$], u satisfies the boundary value problem (MP) of [58] with the set of boundary conditions (iii)(b). Therefore, by [58, Theorem $C.1$], $u = 0$. □

To establish that a solution to **BVP4** exists and to show that Theorem 3.2.4 holds, it is helpful to look for a solution to **BVP4** in the form

$$u(x) = \int_{\Gamma^0} \Big[\frac{\partial G_{1,h}(x,y)}{\partial n(y)} + i\eta G_{1,h}(x,y)\Big]\phi(y)\mathrm{ds}(y), \qquad x \in G_0, \tag{3.28}$$

for some $\phi \in BC(\Gamma^0)$, where n is the unit normal on Γ^0 directed into G_0, and $\eta \in \mathbb{C}$ is a constant to be specified later.

Lemma 3.2.2 *The combined layer potential (3.28) with density $\phi \in BC(\Gamma^0)$ satisfies the above BVP iff ϕ satisfies the boundary integral equation*

$$g(x) = \frac{1}{2}\phi(x) + \int_{\Gamma^0} \Big[\frac{\partial G_{1,h}(x,y)}{\partial n(y)} + i\eta G_{1,h}(x,y)\Big]\phi(y)\,ds(y), \qquad x \in \Gamma^0. \tag{3.29}$$

Proof. By Lemmas A.1(i) and A.2(i) in Appendix A, if u is defined by (3.28) then $u \in C^2(G_0 \cup \Gamma_h)$ and

$$\Delta u + k^2 u = 0 \qquad \text{in } G_0.$$

By Lemma A.3 and (3.17) there holds

$$\frac{\partial u(x)}{\partial x_2} + iku(x) = 0, \qquad \text{for } x \in \Gamma_h.$$

By Lemmas A.1(ii) and A.2(ii) in Appendix A, u can be continuously extended from G_0 up to the boundary Γ^0 with the limiting value

$$u_-(x) = \int_{\Gamma^0} \Big[\frac{\partial G_{1,h}(x,y)}{\partial n(y)} + i\eta G_{1,h}(x,y)\Big]\phi(y)\mathrm{ds}(y) + \frac{1}{2}\phi(x), \qquad x \in \Gamma^0. \tag{3.30}$$

Thus u given by (3.28) satisfies **BVP4** iff $u_-(x) = g(x)$, $x \in \Gamma^0$, i.e. iff ϕ satisfies the BIE, (3.29). $\square$

Lemma 3.2.3 *If $\Re\eta < 0$, then the integral equation (3.29) has at most one solution in $BC(\Gamma^0)$.*

Proof. Suppose $\phi \in BC(\Gamma^0)$ satisfies (3.29) with $g = 0$ and define

$$\tilde{u}(x) := \begin{cases} -\int_{\Gamma^0}\left[\frac{\partial G_{1,h}(x,y)}{\partial n(y)} + i\eta G_{1,h}(x,y)\right]\phi(y)\mathrm{ds}(y), & x \in \overline{U}_h\backslash\Gamma^0, \\ \phi(x), & x \in \Gamma^0, \end{cases}$$

and let $\beta \in BC(\Gamma^0)$ be defined by $\beta(y) = -\eta/k$, $y \in \Gamma^0$. Then $\tilde{u}$ satisfies equations (3.24) and (3.25) with $g = 0$ and so, by Theorem 3.2.2, $\tilde{u}$ satisfies the impedance boundary value problem, **BVP3** with $D = U_h\backslash\overline{G}_0$. Since $Re(\eta) < 0$ Theorem 3.2.3 can be applied giving $\tilde{u} = 0$ in $U_h\backslash G_0$ so that $\phi = 0$. We have shown that $\phi = 0$ is the only solution of the homogenous version of the integral equation (3.29). Hence equation (3.29) has at most one solution. $\square$

Lemma 3.2.4 *If $g \in L^2(\Gamma^0)\cap BC(\Gamma^0)$ then equation (3.29) has exactly one solution $\phi \in L^2(\Gamma^0)\cap BC(\Gamma^0)$ and, for some constant $C > 0$ independent of g,*

$$\|\phi\|_{L^2(\Gamma^0)} \leq C\|g\|_{L^2(\Gamma^0)}.$$

Proof. Throughout the proof $C > 0$ denotes a constant independent of g, not necessarily the same at each occurrence. We can see that

$$\begin{aligned} \int_{\Gamma^0} |\phi(x)|^2 \mathrm{ds}(x) &= \int_{-\infty}^{+\infty} |\widetilde{\phi}(x_1)|^2 \sqrt{1 + (f'_{x^*}(x_1))^2}\mathrm{dx}_1 \\ &\leq \sqrt{1 + \|f'_0\|^2_\infty} \int_{-\infty}^{\infty} |\widetilde{\phi}(x_1)|^2 \mathrm{d}x_1, \end{aligned} \tag{3.31}$$

where $\tilde{\phi} := \phi((x_1, f_0(x_1)))$ for $x_1 \in \mathbb{R}$, so that

$$\|\phi\|_{L^2(\Gamma^0)} \leq C\|\widetilde{\phi}\|_2. \tag{3.32}$$

Similarly, where $\tilde{g} \in BC(\mathbb{R})$ is defined by $\tilde{g}(x_1) = g((x_1, f_0(x_1)))$, $x_1 \in \mathbb{R}$,

$$\begin{aligned}\int_{-\infty}^{\infty} |\widetilde{g}(x_1)|^2 \mathrm{d}x_1 &\leq \int_{-\infty}^{\infty} |\widetilde{g}(x_1)|^2 \sqrt{1 + (f_0'(x_1))^2}\mathrm{d}x_1 \\ &= \int_{\Gamma^0} |g(x)|^2 \mathrm{ds}(x),\end{aligned}$$

so that

$$\|\widetilde{g}\|_2 \leq \|g\|_{L^2(\Gamma^0)}. \tag{3.33}$$

Now (3.29) can be rewritten as

$$2\int_{-\infty}^{\infty} \Big[\frac{\partial G_{1,h}(x,y)}{\partial n(y)} + i\eta G_{1,h}(x,y)\Big]\widetilde{\phi}(t)\sqrt{1 + (f_0'(t))^2}\mathrm{d}t + \widetilde{\phi}(s) = 2\widetilde{g}(s), \quad s \in \mathbb{R}, \tag{3.34}$$

where $x = (s, f_0(s))$, $y = (t, f_0(t))$. Let

$$k(s,t) := 2\Big[\frac{\partial G_{1,h}(x,y)}{\partial n(y)} + i\eta G_{1,h}(x,y)\Big]\sqrt{1 + (f_0'(t))^2}, \qquad s, t \in \mathbb{R}, s \neq t,$$

and define the integral operator K by

$$K\widetilde{\phi}(s) := \int_{-\infty}^{\infty} k(s,t)\widetilde{\phi}(t)\mathrm{d}t.$$

Then (3.29) may be written as

$$(1 + K)\widetilde{\phi} = 2\widetilde{g}. \tag{3.35}$$

This equation is similar to [2, equation (4.6)] which takes the same form as (3.35), but with a slightly different kernel function k. In [2, Corollory 4.5] it is shown that, for every $\tilde{g} \in L^2(\mathbb{R}) \cap BC(\mathbb{R})$, [2, equation (4.6)] has exactly one solution, $\tilde{\phi} \in L^2(\mathbb{R}) \cap BC(\mathbb{R})$, with $\|\tilde{\phi}\|_2 \leq C\|\tilde{g}\|_2$. The proof given for [2, Corollory 4.5] works, with slight modifications, in our case. In more detail, the proof of [2, Corollory 4.5] is based on [2, lemmas 4.2, 4.3 and 4.4], establishing properties of the kernel k, and, as discussed below, the same properties hold for our case.

The first property of k required is that equation (3.35) has at most one solution in $BC(\mathbb{R})$. Equation (3.35) is equivalent to equation (3.29) so that it has been proved

in Lemma 3.2.3 that there is at most one solution to (3.35) in $BC(\mathbb{R})$. The second property is that

$$|k(s,t)| \leq \kappa(s-t), \qquad s,t \in \mathbb{R}, s \neq t, \tag{3.36}$$

for some $\kappa \in L^1(\mathbb{R})$. That this is true follows from [58, Lemma $B.2$] with $\kappa(s) = C\tilde{\kappa}(s)$, for some $C > 0$, and

$$\tilde{\kappa}(s) := \begin{cases} 1 - \log|s|, & 0 < s \leq 1, \\ |s|^{-\frac{3}{2}}, & |s| > 1, \end{cases}$$

The final property required is to check that [2, Lemma 4.4] holds in our case, which follows using the proof given in [10, Lemma 4.6]. Thus, by modifying the proof of [2, corollary 4.5], it follows that (3.35) has exactly one solution $\widetilde{\phi} \in L^2(\mathbb{R})$ for every $\widetilde{g} \in L^2(\mathbb{R})$, and that there exists $C > 0$ such that

$$\|\widetilde{\phi}\|_2 \leq C\|\widetilde{g}\|_2. \tag{3.37}$$

Now from (3.32) and (3.33), together with (3.37) we have

$$\|\phi\|_{L^2(\Gamma^0)} \leq C\|\widetilde{\phi}\|_2 \leq C\|\widetilde{g}\| \leq C\|g\|_{L^2(\Gamma^0)}.$$

□

Corollary 3.2.5 ***BVP4*** *has exactly one solution and this solution is given by (3.28) with ϕ the unique solution of (3.29) in $L^2(\Gamma^0) \cap BC(\Gamma^0)$.*

Proof. From Lemma 3.2.1 we know that the boundary value problem has at most one solution. From Lemma 3.2.2 we have that the combined layer potential (3.28) satisfies the boundary value problem iff $\phi \in BC(\Gamma^0)$ satisfies the boundary integral equation (3.29). Then Lemma 3.2.4 says that (3.29) has a solution and that this solution is unique. □

Proof of Theorem 3.2.4 By Corollary 3.2.5 the boundary value problem has exactly one solution and this solution is given by (3.28) with $\phi \in L^2(\Gamma^0) \cap BC(\Gamma^0)$ the unique solution of (3.29). Further, from Lemma 3.2.4, for some constant $C' > 0$ independent of g,

$$\|\phi\|_{L^2(\Gamma^0)} \leq C' \|g\|_{L^2(\Gamma^0)}. \tag{3.38}$$

From (3.28), if $\epsilon > 0$ and $x \in G_0$ with $h \leq x_2 \leq f_0(x_1) - \epsilon$ we see that

$$\begin{aligned}
|u(x)| &= \Big| \int_{\Gamma^0} \Big(\nabla_y G_{1,h}(x,y).n(y) + i\eta G_{1,h}(x,y) \Big) \phi(y) \mathrm{ds}(y) \Big| \\
&\leq \Big(\int_{\Gamma^0} \Big| \nabla_y G_{1,h}(x,y).n(y) + i\eta G_{1,h}(x,y) \Big|^2 \mathrm{ds}(y) \Big)^{\frac{1}{2}} \Big(\int_{\Gamma^0} |\phi(y)|^2 \mathrm{ds}(y) \Big)^{\frac{1}{2}} \\
&\leq \|\phi\|_{L^2(\Gamma^0)} \Big(\int_{\Gamma^0} \Big(|\nabla_y G_{1,h}(x,y)| + |\eta| |G_{1,h}(x,y)| \Big)^2 \mathrm{ds}(y) \Big)^{\frac{1}{2}} \\
&\leq \|\phi\|_{L^2(\Gamma^0)} \Big(\int_{\Gamma^0} \Big(\frac{C^*(1 + x_2 - h)(1 + y_2 - h)}{|x - y|^{\frac{3}{2}}} \Big)^2 \mathrm{ds}(y) \Big)^{\frac{1}{2}},
\end{aligned}$$

by the Cauchy-Schwarz inequality and equations (3.19) and (3.20), where $C^* = C(1 + |\eta|)$. Making the substitution $y = (t, f_0(t))$ and $\mathrm{ds}(y) = \sqrt{1 + (f_0'(t))^2} \mathrm{d}t$ we get

$$\begin{aligned}
|u(x)| &\leq \|\phi\|_{L_2(\Gamma^0)} \Big(\int_{-\infty}^{\infty} \frac{(C^*)^2 (1 + x_2 - h)^2 (1 + f_0(t) - h)^2 \sqrt{1 + (f_0'(t))^2} \mathrm{d}t}{[(x_1 - t)^2 + (x_2 - f_0(t))^2]^{\frac{3}{2}}} \Big)^{\frac{1}{2}} \\
&\leq D I^{\frac{1}{2}} \|\phi\|_{L_2(\Gamma^0)}
\end{aligned}$$

where $D = C^*(1 + \|f_0\|_\infty)^2 (1 + \|f_0'\|_\infty^2)^{\frac{1}{4}}$ and

$$I = \int_{-\infty}^{\infty} \frac{\mathrm{d}t}{[(x_1 - t)^2 + (x_2 - f_0(t))^2]^{\frac{3}{2}}}. \tag{3.39}$$

Now, for $\tau > 0$, $I = I_1 + I_2$ where

$$I_1 = \int_{x_1 + \tau}^{\infty} \frac{\mathrm{d}t}{[(x_1 - t)^2 + (x_2 - f_0(t))^2]^{\frac{3}{2}}} + \int_{-\infty}^{x_1 - \tau} \frac{\mathrm{d}t}{[(x_1 - t)^2 + (x_2 - f_0(t))^2]^{\frac{3}{2}}},$$

and

$$I_2 = \int_{x_1 - \tau}^{x_1 + \tau} \frac{\mathrm{d}t}{[(x_1 - t)^2 + (x_2 - f_0(t))^2]^{\frac{3}{2}}}. \tag{3.40}$$

Further,

$$\begin{aligned} I_1 &\leq \int_{x_1+\tau}^{\infty} \frac{\mathrm{dt}}{|x_1-t|^3} + \int_{-\infty}^{x_1-\tau} \frac{\mathrm{dt}}{|x_1-t|^3}, \\ &= 2\int_{x_1+\tau}^{\infty} \frac{\mathrm{d}t}{(t-x_1)^3} = \frac{1}{\tau^2}. \end{aligned}$$

Now choose $\tau = \epsilon/(2m)$, where $m = \|f_0'\|_\infty$. Then, for $|x_1 - t| \leq \tau$, it holds that $|f_0(x_1) - f_0(t)| \leq \tau m = \frac{\epsilon}{2}$, so that

$$\begin{aligned} f_0(t) &\geq f_0(x_1) - |f_0(t) - f_0(x_1)| \\ &\geq \epsilon + x_2 - \frac{\epsilon}{2} \\ &= x_2 + \frac{\epsilon}{2}. \end{aligned}$$

Thus

$$\begin{aligned} I_2 &\leq \int_{x_1-\tau}^{x_1+\tau} \frac{\mathrm{dt}}{[(x_1-t)^2 + (\frac{\epsilon}{2})^2]^{\frac{3}{2}}}, \\ &\leq 2\tau\Big(\frac{\epsilon}{2}\Big)^{-3} \end{aligned}$$

and so

$$\begin{aligned} I &\leq \frac{1}{\tau^2} + 2\tau\Big(\frac{\epsilon}{2}\Big)^{-3} \\ &= \frac{4}{\epsilon^2}[m^2 + \frac{2}{m}]. \end{aligned} \tag{3.41}$$

So

$$|u(x)| \leq D^* \|\phi\|_{L_2(\Gamma_0)}$$

where $D^* = 2D\frac{\sqrt{m^2+\frac{2}{m}}}{\epsilon}$, and then using (3.38),

$$|u(x)| \leq \hat{C}\|g\|_{L^2(\Gamma_0)},$$

with $\hat{C} = D^*C'$, independent of g. □

Chapter 4

The Point Source Method

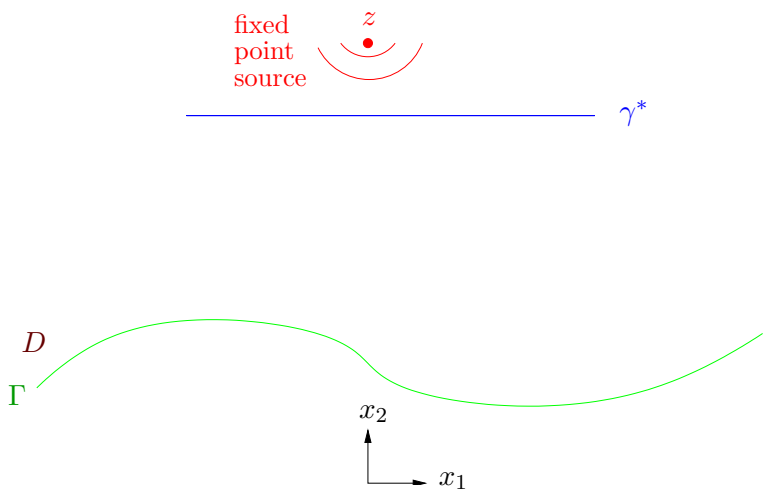

Figure 4.1: The inverse problem geometry

In Chapter 3 we discuss the $2D$ problem of an electromagnetic wave, from a point source, incident on an infinite perfectly conducting rough surface. We formulate the *direct problem* of computing the scattered field given the boundary Γ as the boundary value problem **BVP1**. In this chapter we are concerned with the corresponding inverse problem. We remind the reader that Γ and D are defined by equations (3.1) and (3.3) respectively and the total field at a point $x \in D$ due to a point source at $z \in D$ is denoted by $G(x, z)$. Now let $A > 0$, $H > \sup f$, and let γ^* denote the finite horizontal line

$$\gamma^* = \{(x_1, H) | |x_1| \leq A\}. \tag{4.1}$$

Then the specific inverse problem we will be studying is as follows (see Figure 4.1):

The Inverse Problem. *Given measurements of the total field $G(x, z)$, for $x \in \gamma^*$ and a single source position $z \in D \backslash \gamma^*$, determine f, i.e. the location of the infinite surface Γ.*

It is an open question whether this inverse problem is uniquely solvable.

4.1 An overview of the Point Source Method

The method we will formulate for computing a solution to this inverse problem is based on the Point Source Method of Potthast [44, 45] for scattering by bounded obstacles. The idea of this method is to construct, from the measured data, namely $G(x,z)$ for x on γ^*, an approximation $G^\alpha(x,z)$ to the total field $G(x,z)$ for all $x \in D$. Since $G(\cdot,z)$ vanishes on Γ and provided $G(\cdot,z)$ does not vanish on other curves in D, a possibility is to look for the surface as a minimum of $|G^\alpha(\cdot,z)|$, and this is the approach adopted in the Point Source Method.

The first step in constructing $G^\alpha(\cdot,z)$ is to note the reciprocity result shown in Theorem 3.1.4, that

$$G(x^*,z) = G(z,x^*), \qquad x^*, z \in D.$$

It follows that we can proceed by constructing an approximation to $G(z,x^*)$ for $x^* \in D$.

Suppose $x^* \in D\backslash\{z\}$ and $f_0 \in C^{1,1}(\mathbb{R})$ with $f_0(0) < 0$, and define $f_{x^*} \in C^{1,1}(\mathbb{R})$ by $f_{x^*}(x_1) := f_0(x_1 - x_1^*) + x_2^*$, $x_1 \in \mathbb{R}$, and suppose that

$$\Gamma_{x^*} := \{(x_1, f_{x^*}(x_1))|\ x_1 \in \mathbb{R}\} \subset D. \tag{4.2}$$

We assume that values f_- and f_+ for which (3.2) holds are known and define $\epsilon_+ := \sup_{x_1\in\mathbb{R}} f_0(x_1)$ and $\epsilon_- := -\inf_{x_1\in\mathbb{R}} f_0(x_1)$. We assume further that f_0 and H are chosen so that $H > f_+ + \epsilon_+$. Then, for $x^* \in \overline{U}_{f_-}\backslash U_{f_+}$, i.e. $f_- \le x_2^* \le f_+$, Γ_{x^*} lies below $\Gamma_H \supset \gamma^*$. Choose $d > \max(f_+ - f_-, \epsilon_-)$ and let $h^* := x_2^* - d$ so that $h^* < f_-$ and $\Gamma_{x^*} \subset U_{h^*}$, for $f_- \le x_2^* \le f_+$ (see Figure 4.2).

Consider the first kind integral equation

$$\int_{\gamma^*} G_{1,h^*}(x,y)\phi_{x^*}(y)\ \mathrm{ds}(y) = g_{x^*}(x) := G_{1,h^*}(x,x^*), \quad x \in \Gamma_{x^*}, \tag{4.3}$$

where G_{1,h^*} is defined by equation (3.16). We will see shortly that (4.3) does not have a solution but we can find a function $\phi_{x^*}^\alpha \in L^2(\gamma^*)$ which will solve it approximately

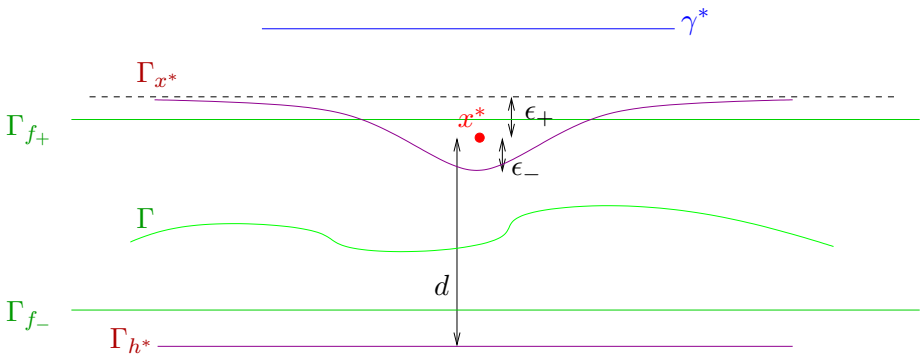

Figure 4.2: Geometric description of solution of the integral equation 4.3

to arbitrary accuracy. Precisely, defining the residual in (4.3) by

$$u(x) := \int_{\gamma^*} G_{1,h^*}(x,y)\phi^{\alpha}_{x^*}(y)\mathrm{ds}(y) - G_{1,h^*}(x,x^*), \qquad x \in \overline{U}_{h^*}, \tag{4.4}$$

we can make u as small as we like in the L^2 norm on Γ_{x^*}. Using this and properties of $G_{1,h^*}(\cdot,y)$, for $y \in D$, we will go on to show that u satisfies **BVP5** in section 4.2 below, with $g = u|_{\Gamma_{x^*}}$. Note that we take $f_- \leq x_2^* \leq f_+$ which ensures that Γ_{h^*} lies below Γ. We will see that the condition that u is small on Γ_{x^*} implies that u is small within the duct, and hence that u is small on Γ itself, provided Γ lies between Γ_{h^*} and Γ_{x^*}. Replacing $G_{1,h^*}(x,\cdot)$ with $U_1^s(x,\cdot)$ in (4.4) we define

$$w(x) := \int_{\gamma^*} U_1^s(x,y)\phi^{\alpha}_{x^*}(y)\ \mathrm{ds}(y) - U_1^s(x,x^*), \qquad x \in \overline{D},$$

and show that w satisfies **BVP2** with boundary data $g = -u|_{\Gamma}$, and therefore, using Theorems 3.1.2 and 4.2.4, we conclude, since the boundary data is small, that w is small in D, in particular that w is small at z, i.e. $w(z) \approx 0$, in other words

$$U_1^s(z,x^*) \approx \int_{\gamma^*} U_1^s(z,y)\phi^{\alpha}_{x^*}(y)\mathrm{ds}(y). \tag{4.5}$$

From equation (4.5) and Theorem 3.1.4 it follows that

$$\begin{aligned} G(x^*, z) &= G(z, x^*) \\ &= G_{1,h^*}(z, x^*) + U_1^s(z, x^*) \\ &\approx G_{1,h^*}(z, x^*) + \int_{\gamma^*} U_1^s(z, y)\phi_{x^*}^{\alpha}(y)\ \mathrm{ds}(y) \\ &= G_{1,h^*}(z, x^*) + \int_{\gamma^*} (G(y, z) - G_{1,h^*}(z, y))\phi_{x^*}^{\alpha}(y)\ \mathrm{ds}(y). \end{aligned} \tag{4.6}$$

Hence we define, as our approximation to $G(x^*, z)$, the quantity

$$G^{\alpha}(x^*, z) := G_{1,h^*}(z, x^*) + \int_{\gamma^*} \left(G(y, z) - G_{1,h^*}(z, y)\right) \phi_{x^*}^{\alpha}(y)\ \mathrm{ds}(y),\ \ x^* \in \overline{U}_{f_-} \backslash U_{f_+} \tag{4.7}$$

Thus our Point Source Method is, given a source position z, and the total field $G(y, z)$, for $y \in \gamma^*$, compute $G^{\alpha}(x^*, z)$ for $x^* \in \overline{U}_{f_-} \backslash U_{f_+}$, and look for the location of the surface as the minimum of $|G^{\alpha}(x^*, z)|$.

4.2 Rigorous Analysis of the Point Source Method

Within this section we will analyse, in depth, the Point Source Method suggested above. Note that equation (4.3) can be written in operator form as

$$K\phi_{x^*} = g_{x^*}, \tag{4.8}$$

where the integral operator K is defined by

$$K\psi(x) = \int_{\gamma^*} G_{1,h^*}(x, y)\psi(y)\mathrm{ds}(y), \quad x \in \Gamma_{x^*}, \tag{4.9}$$

for $\psi \in L^2(\gamma^*)$.

Theorem 4.2.1 *$K : L^2(\gamma^*) \to L^2(\Gamma_{x^*})$ and is bounded.*

Proof. Define γ^* and Γ_{x^*} by (4.1) and (4.2) respectively. Note that $\Gamma_{x^*} \subset U_{h^*}$ and $\sup f_{x^*} < H$. Since $G_{1,h^*}(x, y)$ is continuous for $x \neq y$ and the bound (3.19) holds, it is clear that

$$\phi(x) = K\psi(x) = \int_{\gamma^*} G_{1,h^*}(x, y)\psi(y)\mathrm{ds}(y) \tag{4.10}$$

exists for all $\psi \in L^2(\gamma^*)$ and $x \in \overline{U}_{h^*} \backslash \gamma^* \supset \Gamma_{x^*}$. Further, if $\psi \in L^2(\gamma^*)$, $0 < \epsilon < \text{dist}(x, \Gamma_{x^*})$ and $|x - x'| < \epsilon$, then

$$\begin{aligned} |\phi(x) - \phi(x')| &\leq \int_{\gamma^*} |G_{1,h^*}(x,y) - G_{1,h^*}(x',y)||\psi(y)|\mathrm{ds}(y) \\ &\leq \left\{ \int_{\gamma^*} |G_{1,h^*}(x,y) - G_{1,h^*}(x',y)|^2 \mathrm{ds}(y) \right\}^{\frac{1}{2}} \|\psi\|_{L^2(\gamma^*)} \\ &\leq |x - x'| \left\{ \int_{\gamma^*} \left[\max_{z \in \overline{B_\epsilon(x)}} |\nabla_z G_{1,h^*}(z,y)| \right]^2 \mathrm{ds}(y) \right\}^{\frac{1}{2}} \|\psi\|_{L^2(\gamma^*)}. \end{aligned}$$

Note that the integral in this expression is finite thanks to the bound (3.20) on $\nabla_z G_{1,h^*}(z,y)$. Thus $\phi(x') \to \phi(x)$ as $x' \to x$ so that $K\psi \in C(\Gamma_{x^*})$ and so $K\psi$ is measurable.

To show that $K\psi \in L^2(\Gamma_{x^*})$ and that the mapping $K : L^2(\gamma^*) \to L^2(\Gamma_{x^*})$ is bounded we use the following standard estimates. First of all, as seen by equation (3.31),

$$\int_{\Gamma_{x^*}} |K\psi(x)|^2 \mathrm{ds}(x) \leq \sqrt{1 + \|f'_{x^*}\|^2_\infty} \int_{-\infty}^{+\infty} |\widetilde{\phi}(x_1)|^2 \mathrm{dx}_1, \tag{4.11}$$

where

$$\widetilde{\phi}(x_1) := \phi\left((x_1, f_{x^*}(x_1))\right), \quad x_1 \in \mathbb{R}. \tag{4.12}$$

Also

$$|\widetilde{\phi}(x_1)| = \Big| \int_{-A}^{A} k_1(x_1, y_1) \widetilde{\psi}(y_1) \mathrm{dy}_1 \Big|$$

where $\widetilde{\psi}(y_1) = \psi\left((y_1, H)\right)$ and

$$k_1(x_1, y_1) = G_{1,h^*}(x,y)\Big|_{x=(x_1, f_{x^*}(x_1)), y=(y_1,H)}.$$

From (3.19),

$$\begin{aligned} |k_1(x_1,y_1)| &\leq C(1+H)(1+\|f_{x^*}\|_\infty)|x-y|^{-\frac{3}{2}} \\ &\leq C(1+H)(1+\|f_{x^*}\|_\infty)(c^2 + |x_1 - y_1|^2)^{-\frac{3}{4}} \end{aligned}$$

where $c = H - \sup_{x_1 \in \mathbb{R}} f_{x^*}(x_1)$. Thus

$$|\widetilde{\phi}(x_1)| \leq \int_{-\infty}^{+\infty} \kappa_1(x_1 - y_1)|\widetilde{\psi}(y_1)|\mathrm{d}y_1,$$

where

$$\kappa_1(s) := C(1+H)(1+\|f_{x^*}\|_\infty)(c^2+s^2)^{-\frac{3}{4}}.$$

Now $\kappa_1 \in L^1(\mathbb{R})$. Since $\widetilde{\psi} \in L^2(\mathbb{R})$, it follows by Theorem 1.3.1 that $\widetilde{\phi} \in L^2(\mathbb{R})$ with

$$\|\widetilde{\phi}\|_2 \leq \|\kappa_1\|_1 \|\widetilde{\psi}\|_2 = \|\kappa_1\|_1 \|\psi\|_{L^2(\gamma^*)}. \tag{4.13}$$

Thus, by (4.11), $K\psi \in L^2(\Gamma_{x^*})$ with $\|K\psi\|_{L^2(\Gamma_{x^*})} \leq (1+\|f'_{x^*}\|_\infty^2)^{\frac{1}{2}} \|\widetilde{\phi}\|_2$ and so from (4.13)

$$\|K\psi\|_{L^2(\Gamma_{x^*})} \leq (1+\|f'_{x^*}\|_\infty^2)^{\frac{1}{2}} \|\kappa_1\|_1 \|\psi\|_{L^2(\gamma^*)}.$$

□

Lemma 4.2.1 *For all $x^* \in \overline{U}_{f_-} \backslash U_{f_+}$, $g_{x^*} \in L^2(\Gamma_{x^*})$ is not in the range of K and hence equation (4.3) does not have a solution $\phi_{x^*} \in L^2(\gamma^*)$.*

Proof. In view of the bound (3.19), $g_{x^*} \in L^2(\Gamma_{x^*})$. Now assume equation (4.3) has a solution $\phi \in L^2(\gamma^*)$ for some $x^* \in D$. Then

$$\int_{\gamma^*} G_{1,h^*}(x,y)\phi_{x^*}(y)\ \mathrm{ds}(y) - G_{1,h^*}(x,x^*) = 0, \quad x \in \Gamma_{x^*}.$$

Define $v \in C^2(\overline{U}_{h^*} \backslash (\gamma^* \cup \{x^*\}))$ by

$$v(x) := \int_{\gamma^*} G_{1,h^*}(x,y)\phi_{x^*}(y)\ \mathrm{ds}(y) - G_{1,h^*}(x,x^*), \quad x \in \overline{U}_{h^*} \backslash (\gamma^* \cup \{x^*\}),$$

and the region G^* by

$$G^* := \{(x_1,x_2) | h^* < x_2 < f_{x^*}(x_1), x_1 \in \mathbb{R}\}. \tag{4.14}$$

Then, recalling the properties of G_{1,h^*} stated in Chapter 3, in particular that G_{1,h^*} is the Green's function for the Helmholtz equation in the half plane U_{h^*} which satisfies the impedance boundary condition (3.17) on Γ_{h^*}, it follows that

$$\begin{aligned} v &= 0 \qquad \text{on } \Gamma_{x^*}, \\ \Delta v + k^2 v &= 0 \qquad \text{in } U_{h^*}, \\ \frac{\partial v}{\partial x_2} + ikv &= 0 \qquad \text{on } \Gamma_{h^*}, \end{aligned}$$

and v is bounded in G^*. Thus, by Theorem 3.2.4, $v = 0$ in G^* and then, by Theorem 1.3.3, $v = 0$ in $U_{h^*}\backslash(\gamma^* \cup \{x^*\})$. Thus

$$G_{1,h^*}(x, x^*) = \int_{\gamma^*} G_{1,h^*}(x, y)\phi_{x^*}(y)\ \mathrm{ds}(y), \qquad x \in U_{h^*}\backslash(\gamma^* \cup \{x^*\}).$$

But $|G_{1,h^*}(x, x^*)| \to \infty$ as $x \to x^*$, whereas the integral on the right hand side is bounded in a neighborhood of x^*, thanks to the bound (3.19), giving a contradiction. □

Though we have just shown that (4.3) has no solution $\phi_{x^*} \in L^2(\gamma^*)$, we will go on to show that K has dense range and so equation (4.3) can be solved with arbitrary accuracy. We also go on to show further properties of K in order to justify the application of the regularisation strategy described in Chapter 2.

Theorem 4.2.2 *K is injective.*

Proof. Suppose $\phi \in L^2(\gamma^*)$ and $K\phi = 0$. Then

$$\int_{\gamma^*} G_{1,h^*}(x, y)\phi(y)\ \mathrm{ds}(y) = 0, \qquad x \in \Gamma_{x^*},$$

and, defining $u \in C^2(\overline{U}_{h^*}\backslash\gamma^*)$ by

$$u(x) := \int_{\gamma^*} G_{1,h^*}(x, y)\phi(y)\ \mathrm{ds}(y), \qquad x \in \overline{U}_{h^*},$$

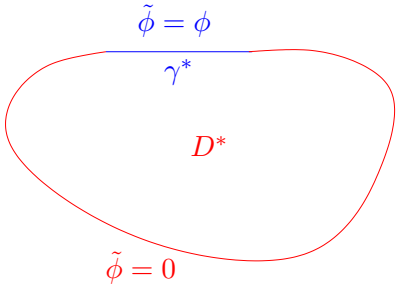

Figure 4.3: The boundary ∂D^*

it follows that

$$\begin{aligned} u &= 0 \quad \text{on } \Gamma_{x^*}, \\ \Delta u + k^2 u &= 0 \quad \text{in } U_{h^*} \backslash \gamma^*, \\ \frac{\partial u}{\partial x_2} + iku &= 0 \quad \text{on } \Gamma_{h^*}, \end{aligned}$$

and v is bounded in G^*, where $G^* := \{(x_1, x_2) | h^* < x_2 < f_{x^*}(x_1), x_1 \in \mathbb{R}\}$. Therefore, by Theorem 3.2.4, $u = 0$ in G^*, and then, by Theorem 1.3.3, $u = 0$ in $U_{h^*} \backslash \gamma^*$. Let D^* be a bounded region, with smooth boundary ∂D^*, such that $\gamma^* \subset \partial D^*$ and $\overline{D}^* \subset U_{h^*}$, as shown in Figure 4.3. Define

$$\widetilde{\phi}(x) := \begin{cases} \phi(x), & x \in \gamma^*, \\ 0, & x \in \partial D^* \backslash \gamma^*. \end{cases}$$

Then $\widetilde{\phi} \in L^2(\partial D^*)$ and

$$u(x) = \int_{\partial D^*} G_{1,h^*}(x, y) \widetilde{\phi}(y) \, \mathrm{ds}(y), \qquad x \in \overline{U}_{h^*}.$$

Thus, by [45, Theorem 1.2.4],

$$\lim_{h \to 0^+} \int_{\partial D^*} \left| \frac{\partial u(x \pm h n(x))}{\partial n} - \int_{\partial D^*} \frac{\partial G_{1,h^*}(x, y)}{\partial n(x)} \widetilde{\phi}(y) \, \mathrm{ds}(y) \pm \frac{1}{2} \widetilde{\phi}(x) \right|^2 \mathrm{ds}(x) = 0.$$

Defining

$$p(x) = \int_{\partial D^*} \frac{\partial G_{1,h^*}(x,y)}{\partial n(y)} \widetilde{\phi}(y)\ \mathrm{ds}(y), \qquad x \in \partial D^*,$$

and, for $h > 0$,

$$W_{\pm h}(x) := \frac{\partial u(x \pm hn(x))}{\partial n}, \qquad x \in \partial D^*,$$

we have that $W_h = W_{-h} = 0$ for $h > 0$ sufficiently small and

$$\|W_{\pm h} - p \pm \frac{1}{2}\widetilde{\phi}\|_2^2 \to 0 \qquad \text{as } h \to 0^+.$$

Thus

$$\begin{aligned} \|\phi\|_2 &= \|\widetilde{\phi}\|_2 \\ &= \|W_h - W_{-h} + \widetilde{\phi}\|_2 \\ &= \|(W_h - p + \frac{1}{2}\widetilde{\phi}) - (W_{-h} - p - \frac{1}{2}\widetilde{\phi})\|_2 \\ &\leq \|(W_h - p + \frac{1}{2}\widetilde{\phi})\|_2 + \|(W_{-h} - p - \frac{1}{2}\widetilde{\phi})\|_2 \to 0, \end{aligned}$$

as $h \to 0^+$. Thus $\phi = 0$. □

Theorem 4.2.3 *K has dense range.*

Proof. For $\phi \in L^2(\Gamma_{x^*})$, define $\tilde{K} : L^2(\Gamma_{x^*}) \to L^2(\gamma^*)$ by

$$\tilde{K}\phi(x) = \int_{\Gamma_{x^*}} \overline{G}_{1,h^*}(y,x)\phi(y)\mathrm{ds}(y), \qquad x \in \gamma^*. \tag{4.15}$$

Then

$$(\psi, \tilde{K}\phi) = \int_{\gamma^*} \psi(x) \left\{ \int_{\Gamma_{x^*}} G_{1,h^*}(x,y)\overline{\phi}(y)\mathrm{ds}(y) \right\} \mathrm{ds}(x). \tag{4.16}$$

Define

$$\chi(x) = \int_{\Gamma_{x^*}} |G_{1,h^*}(x,y)||\overline{\phi}(y)|\mathrm{ds}(y), \qquad x \in \gamma^*.$$

Let $0 < \epsilon < \text{dist}(x, \gamma^*)$ and $|x - x'| < \epsilon$. Then, since $\overline{\phi} \in L^2(\gamma^*)$,

$$\begin{aligned} |\chi(x) - \chi(x')| &\leq \int_{\Gamma_{x^*}} |G_{1,h^*}(x,y) - G_{1,h^*}(x',y)||\overline{\phi}(y)|\text{ds}(y) \\ &\leq |x - x'|\left\{ \int_{\Gamma_{x^*}} \left[\max_{z \in \overline{B_\epsilon(x)}} |\nabla_z G_{1,h^*}(z,y)| \right]^2 \text{ds}(y) \right\}^{\frac{1}{2}} \|\overline{\phi}\|_{L^2(\gamma^*)}. \end{aligned}$$

Note that the integral in this expression is finite thanks to the bound (3.20) on $\nabla_z G_{1,h^*}(z,y)$. Thus $\chi(x') \to \chi(x)$ as $x' \to x$ so that $\chi \in C(\gamma^*) \subset L^2(\gamma^*)$. Hence, by Cauchy-Schwarz, $|\psi|\chi \in L^1(\gamma^*)$. Since $\psi \in L^2(\gamma^*)$ and $\phi \in L^2(\Gamma_x^*)$, we have that $\psi(x)\overline{\phi}(y)$ is measurable on $\gamma^* \times \Gamma_{x^*}$. Hence, and since $G_{1,h^*} \in C(\gamma^* \times \Gamma_{x^*})$, $\psi(x)G_{1,h^*}(x,y)\overline{\phi}(y)$ is measurable on $\gamma^* \times \Gamma_{x^*}$. Thus, by Tonelli's Theorem,

$$\int_{\gamma^* \times \Gamma_{x^*}} |\psi(x)G_{1,h^*}(x,y)\overline{\phi}(y)|\text{ds}(y)\text{ds}(x) = \int_{\gamma^*} |\psi|\chi\text{ds} < \infty, \tag{4.17}$$

so that $\psi(x)G_{1,h^*}(x,y)\overline{\phi}(y) \in L^1(\gamma^* \times \Gamma_{x^*})$. Hence, by Fubini's Theorem, the order of integration in equation (4.16) can be interchanged, giving

$$\begin{aligned} (\psi, \tilde{K}\phi) &= \int_{\Gamma_{x^*}} \overline{\phi}(y) \left\{ \int_{\gamma^*} G_{1,h^*}(x,y)\psi(x)\text{ds}(x) \right\} \text{ds}(y) \\ &= (K\psi, \phi), \end{aligned}$$

and so, by the definition in Theorem 2.1.1, $\tilde{K} = K^*$, the adjoint of K.

By Theorem 2.1.2, to show that K has dense range all that remains is to show that K^* is injective. This can be proved in a similar way to the proof of Theorem 4.2.2, as follows.

Suppose $\phi \in L^2(\Gamma_{x^*})$ and $K^*\phi = 0$. Then

$$\int_{\Gamma_{x^*}} \overline{G}_{1,h^*}(x,y)\phi(y)\text{ds}(y) = 0, \qquad x \in \gamma^*.$$

Define $v \in C(\overline{U}_{h^*}) \cap C^2(\overline{U}_{h^*} \backslash \Gamma_{x^*})$ by

$$v(x) := \int_{\Gamma_{x^*}} G_{1,h^*}(x,y)\overline{\phi}(y)\text{ds}(y), \qquad x \in \overline{U}_{h^*}.$$

Then $v = 0$ on $\gamma^* \subset \Gamma_H \subset U_{h^*} \backslash \Gamma_{x^*}$ and $\Delta v + k^2 v = 0$ in $U_{h^*} \backslash \Gamma_{x^*}$. Therefore, by analytic continuation, $v = 0$ on Γ_H and so v satisfies **BVP2** with $D = U_H$ and $g = 0$.

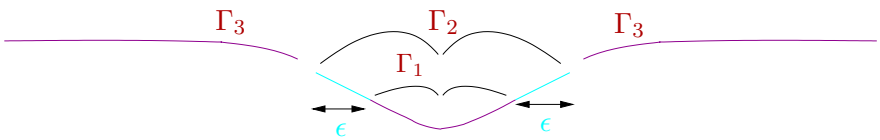

Figure 4.4: Γ_1, Γ_2 and Γ_3

Hence, by Theorem 3.1.1, $v = 0$ in U_H. Furthermore, by Theorem 1.3.3, $v = 0$ in $U_{h^*} \backslash \overline{G}^*$, where the region G^* is defined by

$$G^* := \{(x_1, x_2) | h^* < x_2 < f_{x^*}(x_1), x_1 \in \mathbb{R}\},$$

and since $v \in C(\overline{U}_{h^*})$, $v = 0$ on Γ_{x^*}. So by Theorem 3.2.4 $v = 0$ in G^* and therefore we have $v = 0$ in U_{h^*}.

If we split up Γ_{x^*} into three parts, defined, for some $A^* > 0$ and $\epsilon > 0$, by

$$\begin{aligned} \Gamma_2 &:= \{(x_1, f_{x^*}(x_1))| \ |x_1| \leq A^*\}, \\ \Gamma_1 &:= \{(x_1, f_{x^*}(x_1))| \ |x_1| \leq A^* - \epsilon\}, \end{aligned}$$

and

$$\Gamma_3 := \{(x_1, f_{x^*}(x_1))| \ |x_1| > A^*\},$$

(see Figure 4.4), then we can write $v = v_2 + v_3$ where

$$v_2(x) := \int_{\Gamma_2} G_{1,h^*}(x, y)\overline{\phi}(y)\mathrm{ds}(y), \qquad x \in \overline{U}_{h^*},$$

and

$$v_3(x) := \int_{\Gamma_3} G_{1,h^*}(x, y)\overline{\phi}(y)\mathrm{ds}(y), \qquad x \in \overline{U}_{h^*}.$$

Using a similar argument to that in the proof of Theorem 4.2.2, based on [45, Theorem 1.2.4], we see that

$$\lim_{h\to 0^+}\int_{\Gamma_2}\left|\frac{\partial v_2(y+hn(y))}{\partial n}-\frac{\partial v_2(y-hn(y))}{\partial n}+\overline{\phi}(y)\right|^2\,\mathrm{ds}(y)=0,$$

and, since $v_3\in C^2(\overline{U}_{h^*}\backslash\Gamma_3)$,

$$\lim_{h\to 0^+}\int_{\Gamma_1}\left|\frac{\partial v_3(y+hn(y))}{\partial n}-\frac{\partial v_3(y-hn(y))}{\partial n}\right|^2\,\mathrm{ds}(y)=0.$$

Thus

$$\lim_{h\to 0^+}\int_{\Gamma_1}\left|\frac{\partial v(y+hn(y))}{\partial n}-\frac{\partial v(y-hn(y))}{\partial n}+\overline{\phi}(y)\right|^2\mathrm{ds}(y)=0,$$

and, since $v=0$ in U_{h^*},

$$\int_{\Gamma_1}|\overline{\phi}(y)|^2\mathrm{ds}(y)=0,$$

i.e. $\phi=0$ almost everywhere on Γ_1. Since Γ_1 is an arbitrarily large part of Γ_{x^*}, $\phi=0$ almost everywhere on Γ_{x^*}. $\square$

Having ascertained these important properties of K we are now in a position to analyse the approximate solution of equation (4.3). Although by Lemma 4.2.1 there is no solution $\phi\in L^2(\gamma^*)$ which satisfies equation (4.3) exactly, since K has dense range we can find $\phi_{x^*}\in L^2(\gamma^*)$ with $\|K\phi_{x^*}-g_{x^*}\|_{L^2(\Gamma_{x^*})}$ as small as desired. In particular, this can be achieved by solving equation (4.3) by Tikhonov regularisation with regularisation parameter $\alpha>0$, computing $\phi^\alpha_{x^*}$ as the unique solution of

$$\alpha\phi^\alpha_{x^*}+K^*K\phi^\alpha_{x^*}=K^*g_{x^*}.$$

By Theorem 2.2.4 we have $\|K\phi^\alpha_{x^*}-g_{x^*}\|_{L^2(\Gamma_{x^*})}\to 0$ as $\alpha\to 0$, though since g_{x^*} is not in the range of K, $\|\phi^\alpha_{x^*}\|_{L^2(\gamma^*)}\to\infty$ as $\alpha\to 0$ by Theorem 2.2.5.

Let $G^*:=\{(x_1,x_2)|h^*<x_2<f_{x^*}(x_1)\}$ and

$$u(x):=\int_{\gamma^*}G_{1,h^*}(x,y)\phi^\alpha_{x^*}(y)\mathrm{ds}(y)-G_{1,h^*}(x,x^*),\qquad x\in\overline{G}^*.$$

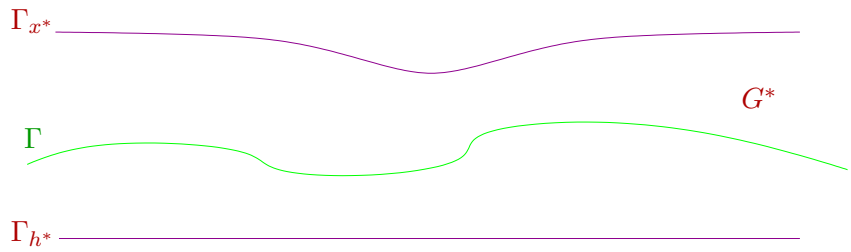

Figure 4.5: The duct geometry. Shown is the case in which $\Gamma \subset G^*$

We can see that if we define $\psi^\alpha := u|_{\Gamma_{x^*}}$ then $\psi^\alpha = K\phi^\alpha_{x^*} - g_{x^*} \in L^2(\Gamma_{x^*}) \cap BC(\Gamma_{x^*})$ and $\|\psi^\alpha\|_{L^2(\Gamma_{x^*})} \to 0$ as $\alpha \to 0$. Further u satisfies the following BVP (see Figure 4.5).

BVP5 Find $u \in C^2(G^*) \cap C^1(G^* \cup \Gamma_{h^*}) \cap BC(\overline{G^*})$ such that

$$\begin{aligned} u &= \psi^\alpha \quad \text{on } \Gamma_{x^*}, \\ \Delta u + k^2 u &= 0 \quad \text{in } G^*, \\ \frac{\partial u}{\partial x_2} + iku &= 0 \quad \text{on } \Gamma_{h^*}, \end{aligned} \tag{4.18}$$

this last condition inherited from the boundary condition (3.17) on Γ_{h^*} satisfied by G_{1,h^*}. The following continuous dependence result for the above BVP in the unbounded domain G^* bounds u in G^* in terms of ψ^α. The (energy absorbing) impedance boundary condition (4.18) is key to ensuring that the BVP is uniquely solvable.

Theorem 4.2.4 *The above boundary value problem (**BVP5**) has exactly one solution. Given $\epsilon > 0$, there exists a constant $C_\epsilon > 0$, such that for $x^* \in \overline{U}_{f_-} \backslash U_{f_+}$,*

$$|u(x)| \le C_\epsilon \|\psi^\alpha\|_{L^2(\Gamma_{x^*})}, \quad h^* \le x_2 \le f_{x^*}(x_1) - \epsilon. \tag{4.19}$$

Proof. Let $G_0 = \{x : -d < x_2 < f_0(x_1)\}$ and define $U(x) = u(x + x^*)$, $x \in \overline{G}_0$, $g(x) = \psi^\alpha(x + x^*)$, $x \in \Gamma^0 := \{(x_1, f_0(x_1))|\ x_1 \in \mathbb{R}\}$. Then U satisfies **BVP4** of section 3.2 and the theorem follows from Theorem 3.2.4.□

Now, denoting $G_\epsilon := \{x \in G^* | x_2 < f_{x^*}(x_1) - \epsilon\}$, provided $\Gamma \subset G_\epsilon$ we have from Theorem 4.2.4, that

$$|u(x)| \leq C_\epsilon \|\psi^\alpha\|_{L^2(\Gamma_{x^*})}, \qquad x \in \Gamma, \tag{4.20}$$

so that u is small on the surface Γ if it is small on Γ_{x^*}. Let

$$w(x) := \int_{\gamma^*} U_1^s(x,y)\phi_{x^*}^\alpha(y)\ \mathrm{ds}(y) - U_1^s(x,x^*), \quad x \in D. \tag{4.21}$$

The following standard elliptic regularity result is a consequence of [9, Lemma 2.7].

Theorem 4.2.5 *Suppose $y \in \mathbb{R}^2$, $\epsilon > 0$, and $u \in C^2(\overline{B_\epsilon(y)})$, where $B_\epsilon(y)$ is the ball of radius ϵ centred on y. If $\Delta u + k^2 u = 0$ in $B_\epsilon(y)$ then*

$$|\nabla u(y)| \leq C \max_{x \in \overline{B_\epsilon(y)}} |u(x)|,$$

where the constant $C > 0$ depends only on ϵ and k.

Lemma 4.2.2 *w satisfies **BVP2** with boundary data $g(x) = -u(x)$, $x \in \Gamma$.*

Proof. We recall that $U_1^s(\cdot, y)$ is the solution to **BVP2** with boundary data $g = -G_{1,h^*}(\cdot, y)$, and in particular that $U_1^s(\cdot, y) \in C^2(D) \cap C(\overline{D})$, for $y \in D$. In fact, by standard elliptic regularity results [22], $U_1^s(\cdot, y) \in C^\infty(D)$ for $y \in D$.

We next note that

$$|U_1^s(x,y) - U_1^s(\tilde{x},\tilde{y})| \leq |U_1^s(x,y) - U_1^s(\tilde{x},y)| + |U_1^s(\tilde{x},y) - U_1^s(\tilde{x},\tilde{y})|$$

for $x, \tilde{x} \in \overline{D}$, $y, \tilde{y} \in D$. Now, for every $x \in \overline{D}$, $y \in D$ and $\epsilon > 0$, there exists $\delta > 0$ such that

$$|U_1^s(x,y) - U_1^s(\tilde{x},y)| < \epsilon$$

if $|x - \tilde{x}| < \delta$. Further, by Theorem 3.1.2,

$$|U_1^s(\tilde{x},y) - U_1^s(\tilde{x},\tilde{y})| \leq C(1 + \tilde{x}_2 - f_-)^{\frac{1}{2}} \|G_{1,h}(\cdot, y) - G_{1,h}(\cdot, \tilde{y})\|_{\infty,\Gamma}.$$

Since

$$\|G_{1,h^*}(\cdot,y) - G_{1,h^*}(\cdot,\tilde{y})\|_{\infty,\Gamma} \to 0 \qquad \text{as } y \to \tilde{y},$$

we can choose δ such that

$$|U_1^s(\tilde{x},y) - U_1^s(\tilde{x},\tilde{y})| \leq \epsilon$$

if $|x-\tilde{x}| < \delta$ and $|y-\tilde{y}| < \delta$. Therefore

$$|U_1^s(x,y) - U_1^s(\tilde{x},\tilde{y})| \leq 2\epsilon$$

if $\max\{|x-\tilde{x}|, |y-\tilde{y}|\} < \delta$. Thus $U_1^s \in C(\overline{D} \times D)$ and so $w \in C(\overline{D})$.

Using a similar argument to that used above we note that

$$|\nabla_x U_1^s(x,y) - \nabla_x U_1^s(\tilde{x},\tilde{y})| \leq |\nabla_x U_1^s(x,y) - \nabla_x U_1^s(\tilde{x},y)| + |\nabla_x U_1^s(\tilde{x},y) - \nabla_x U_1^s(\tilde{x},\tilde{y})|$$

for $x, y, \tilde{x}, \tilde{y} \in D$. Now for all $x, y \in D$ and $\epsilon > 0$, there exists $\delta > 0$ such that

$$|\nabla_x U_1^s(x,y) - \nabla_x U_1^s(\tilde{x},y)| < \epsilon$$

if $|x-\tilde{x}| < \delta$. Further, by Theorem 4.2.5, if δ is chosen small enough such that $B_{2\delta}(x) \subset D$ and if $|x-\tilde{x}| < \delta$, then, for some constant $C > 0$ dependent on k and δ,

$$|\nabla_x U_1^s(\tilde{x},y) - \nabla_x U_1^s(\tilde{x},\tilde{y})| \;\leq\; C \max_{z \in \overline{B_\delta(\tilde{x})}} |U_1^s(z,y) - U_1^s(z,\tilde{y})|,$$

and then, by Theorem 3.1.2,

$$|\nabla_x U_1^s(\tilde{x},y) - \nabla_x U_1^s(\tilde{x},\tilde{y})| \leq C(1+\tilde{x}_2+\delta-f_-)^{\frac{1}{2}} \|G_{1,h}(\cdot,y) - G_{1,h}(\cdot,\tilde{y})\|_{\infty,\Gamma}.$$

Repeating the argument above, since

$$\|G_{1,h^*}(\cdot,y) - G_{1,h^*}(\cdot,\tilde{y})\|_{\infty,\Gamma} \to 0 \qquad \text{as } y \to \tilde{y},$$

we can choose δ such that

$$|\nabla_x U_1^s(\tilde{x},y) - \nabla_x U_1^s(\tilde{x},\tilde{y})| < \epsilon$$

if $|x-\tilde{x}|<\delta$ and $|y-\tilde{y}|<\delta$. Therefore

$$|\nabla_x U_1^s(x,y)-\nabla_x U_1^s(\tilde{x},\tilde{y})|\leq 2\epsilon$$

if $\max\{|x-\tilde{x}|,|y-\tilde{y}|\}<\delta$. Thus $\nabla_x U_1^s(x,y)\in C(D\times\gamma^*)$. Now defining

$$v(x)=\int_{\gamma^*} U_1^s(x,y)\phi_{x^*}^{\alpha}(y)\ \mathrm{ds}(y), \qquad x\in D,$$

by Theorem 1.3.2 we have that $v\in C^1(D)$ and

$$\nabla v(x)=\int_{\gamma^*} \nabla_x U_1^s(x,y)\phi_{x^*}^{\alpha}(y)\mathrm{ds}(y), \qquad x\in D.$$

If we now define

$$\nu_j(x,y):=\frac{\partial U_1^s(x,y)}{\partial x_j}$$

for $j=1,2$, we see that if we follow the above argument, replacing $U_1^s(x,y)$ by $\nu_j(x,y)$, we obtain that $\nabla_x\nu_j(x,y)\in C(D\times\gamma^*)$, for $j=1,2$. Therefore using Theorem 1.3.2 we see that $v\in C^2(D)$, so that $w\in C^2(D)$, and

$$\Delta v(x)=\int_{\gamma^*} \Delta_x U_1^s(x,y)\phi_{x^*}^{\alpha}(y)\mathrm{ds}(y), \qquad x\in D.$$

Thus

$$\begin{aligned}\Delta w(x) &= \Delta_x U_1^s(x,y)-\Delta_x v(x)\\ &= \Delta_x U_1^s(x,y)-\int_{\gamma^*}\Delta_x U_1^s(x,y)\phi_{x^*}^{\alpha}(y)\mathrm{ds}(y).\end{aligned}$$

Since $U_1^s(\cdot,y)$ is a solution of **BVP2**, $\Delta U_1^s(\cdot,y)=-k^2U_1^s(\cdot,y)$ and so

$$\begin{aligned}\Delta w(x) &= -k^2U_1^s(x,y)+\int_{\gamma^*}k^2U_1^s(x,y)\phi_{x^*}^{\alpha}(y)\mathrm{ds}(y),\\ &= -k^2w(x).\end{aligned}$$

Divide γ^* into n equal parts of length $2A/n$, denoted by γ_j^* for $j=1,\ldots,n$, and then define $w_n(x)\approx w(x)$ by

$$w_n(x)=\sum_{j=1}^{n}U_1^s(x,y_j)\int_{\gamma_j^*}\phi_{x^*}^{\alpha}(y)\mathrm{ds}(y)-U_1^s(x,x^*),$$

where $y_j \in \gamma_j^*$. Now, by Theorem 3.1.2, for $x \in D$,

$$\begin{aligned}
|w_n(x)| &\leq |U_1^s(x,x^*)| + \sum_{j=1}^{n} \Big| \int_{\gamma_j^*} U_1^s(x,y)\phi_{x^*}^{\alpha}(y)\mathrm{ds}(y) \Big| \\
&\leq C(1+x_2-f_-)^{\frac{1}{2}} \|G_{1,h^*}(\cdot,x^*)\|_{\infty,\Gamma} + \sum_{j=1}^{n} \max_{y\in\gamma^*} |U_1^s(x,y)| \int_{\gamma_j^*} |\phi_{x^*}^{\alpha}(y)|\mathrm{ds}(y) \\
&= C(1+x_2-f_-)^{\frac{1}{2}} \|G_{1,h^*}(\cdot,x^*)\|_{\infty,\Gamma} + \max_{y\in\gamma^*} |U_1^s(x,y)| \int_{\gamma^*} |\phi_{x^*}^{\alpha}(y)|\mathrm{ds}(y) \\
&\leq C(1+x_2-f_-)^{\frac{1}{2}} \Big[\|G_{1,h^*}(\cdot,x^*)\|_{\infty,\Gamma} + \max_{y\in\gamma^*} \|G_{1,h^*}(\cdot,y)\|_{\infty,\Gamma} \sqrt{2A} \|\phi_{x^*}^{\alpha}\|_2 \Big].
\end{aligned}$$

Hence

$$\sup_{x\in D, n\in\mathbb{N}} (1+x_2-f_-)^{-\frac{1}{2}} |w_n(x)| < \infty. \tag{4.22}$$

Now, by Theorem 3.1.2,

$$\begin{aligned}
w(x) - w_n(x) &= \sum_{j=1}^{n} \int_{\gamma_j^*} \Big(U_1^s(x,y) - U_1^s(x,y_j) \Big) \phi_{x^*}^{\alpha}(y)\mathrm{ds}(y) \\
&\leq C(1+x_2-f_-)^{\frac{1}{2}} \sum_{j=1}^{n} \int_{\gamma_j^*} \|G_{1,h}(\cdot,y) - G_{1,h}(\cdot,y_j)\|_{\infty,\Gamma} |\phi_{x^*}^{\alpha}(y)|\mathrm{ds}(y) \\
&\leq C(1+x_2-f_-)^{\frac{1}{2}} \max_{y,\tilde{y}\in\gamma^*, |y-\tilde{y}|\leq 2A/n} \|G_{1,h}(\cdot,y) - G_{1,h}(\cdot,\tilde{y})\|_{\infty,\Gamma} \|\phi_{x^*}^{\alpha}\|_1.
\end{aligned}$$

Now, for $y \in \gamma^*$,

$$\|G_{1,h^*}(\cdot,y) - G_{1,h^*}(\cdot,\tilde{y})\|_{\infty,\Gamma} \to 0$$

as $|y-\tilde{y}| \to 0$ with $\tilde{y} \in \gamma^*$, i.e. the mapping $\gamma^* \to BC(\Gamma)$, $y \to G_{1,h^*}(\cdot,y)$ is continuous. Since γ^* is compact, the mapping is in fact uniformly continuous, so that

$$\max_{y,\tilde{y}\in\gamma^*, |y-\tilde{y}|\leq \frac{2A}{n}} \|G_{1,h^*}(\cdot,y) - G_{1,h^*}(\cdot,\tilde{y})\|_{\infty,\Gamma} \to 0$$

as $n \to \infty$. Thus $w_n(x) \to w(x)$ as $n \to \infty$, uniformly on bounded subsets of D. Hence, using the equivalence of (i) and (ii) in [9, Theorem 2.9], w satisfies the UPRC, (3.11). Further from (4.22) and that $w_n(x) \to w(x)$ as $n \to \infty$, it follows that

$$\sup_{x\in D} (1+x_2-f_-)^{\frac{1}{2}} |w(x)| < \infty.$$

□

From Lemma 4.2.2 we have seen that w satisfies **BVP2** in Chapter 3 with boundary data $-u(x)$, $x \in \gamma$. Therefore, by Theorem 3.1.2, we have that there exists a constant $C > 0$, dependent only on c_1 and k, such that, provided $f \in B_1$ it holds that

$$|w(x)| \leq C(1 + x_2 - f_-)^{\frac{1}{2}} \sup_{x \in \Gamma} |u(x)|. \tag{4.23}$$

Combining the bounds (4.23) and (4.20) we have that, for $x \in D$, and provided $\Gamma \subset G_\epsilon$ for some $\epsilon > 0$,

$$|w(x)| \leq CC_\epsilon(1 + x_2 - f_-)^{\frac{1}{2}} \|\psi^\alpha\|_{L^2(\Gamma_{x^*})} \to 0$$

as $\alpha \to 0$. In particular this inequality holds for $x^* = z$ so that

$$|U_1^s(z, x^*) - \int_{\gamma^*} U_1^s(z, y)\phi_{x^*}^\alpha(y)\mathrm{ds}(y)| \leq CC_\epsilon(1 + z_2 - f_-)^{\frac{1}{2}} \|\psi^\alpha\|_{L^2(\Gamma_{x^*})} \to 0 \tag{4.24}$$

as $\alpha \to 0$. Thus, for α small enough,

$$U_1^s(z, x^*) \approx \int_{\gamma^*} U_1^s(z, y)\phi_{x^*}^\alpha(y)\mathrm{ds}(y). \tag{4.25}$$

Now, using Theorem 3.1.4, equations (4.25) and (4.6), it follows that

$$G(x^*, z) \approx G_{1,h^*}(z, x^*) + \int_{\gamma^*} (G(y, z) - G_{1,h^*}(z, y))\phi_{x^*}^\alpha(y)\ \mathrm{ds}(y).$$

As stated already, this is the approximation to the total field we use in our Point Source Method, i.e. we use the approximation

$$G^\alpha(x^*, z) := G_{1,h^*}(z, x^*) + \int_{\gamma^*} (G(y, z) - G_{1,h^*}(z, y))\ \phi_{x^*}^\alpha(y)\ \mathrm{ds}(y). \tag{4.26}$$

Given the source position z and the total field $G(y, z)$, for $y \in \gamma^*$, we look for Γ (the surface) as the minimum of the function $|G^\alpha(x^*, z)|$. From (4.24) we obtain the following bound on $G(x^*, z) - G^\alpha(x^*, z)$.

Theorem 4.2.6 *For $x^* \in D\backslash\overline{U_{f_+}}$, $c > 0$ and every $\epsilon > 0$ there exists $C > 0$, dependent only on k, f_0, ϵ, d, and c, such that, provided* $\inf(f_{x^*} - f) > \epsilon$ *and* $\|f\|_{C^{1,1}(\mathbb{R})} \leq c$, *it holds that*

$$|G(x^*, z) - G^\alpha(x^*, z)| \leq C(1 + z_2 - f_-)^{\frac{1}{2}} \|K\phi^\alpha_{x^*} - g_{x^*}\|_{L^2(\Gamma_{x^*})} \to 0 \tag{4.27}$$

as $\alpha \to 0$.

The analysis up to this point neglects the effect of noise in the measured data. In practice we expect to measure $G_\delta(y, z)$ for $y \in \gamma^*$ rather than $G(y, z)$, with $\|G_\delta(\cdot, z) - G(\cdot, z)\|_{L^2(\gamma^*)} = \delta$. Then we compute $G^\alpha_\delta(x^*, z)$, defined by (4.26) with $G(y, z)$ replaced by the noisy data $G_\delta(y, z)$, rather than computing $G^\alpha(x^*, z)$. From (4.26) and (4.27) it follows that

$$|G(x^*, z) - G^\alpha_\delta(x^*, z)| \leq C(1 + z_2 - f_-)^{\frac{1}{2}} \|K\phi^\alpha_{x^*} - g_{x^*}\|_{L^2(\Gamma_{x^*})} + \delta\|\phi^\alpha_{x^*}\|_{L^2(\gamma^*)}. \tag{4.28}$$

By Theorems 2.2.4 and 4.2.6 we see that the first and second terms on the right hand side of this inequality tend, respectively, to zero and infinity as $\alpha \to 0$ with δ fixed. From Lemma 2.2.1,

$$\|\phi^\alpha_{x^*}\|_{L^2(\gamma^*)} \leq \frac{1}{\sqrt{\alpha}} \|g_{x^*}\|_{L^2(\Gamma_{x^*})}, \tag{4.29}$$

so that

$$|G^\alpha(x^*, z) - G^\alpha_\delta(x^*, z)| \leq C(1 + z_2 - f_-)^{\frac{1}{2}} \|K\phi^\alpha_{x^*} - g_{x^*}\|_{L^2(\Gamma_{x^*})} + \frac{\delta}{\sqrt{\alpha}} \|g_{x^*}\|_{L^2(\Gamma^*_x)} \ . \tag{4.30}$$

Thus, if we choose $\alpha = \alpha(\delta)$ such that

$$\frac{\delta^2}{\alpha(\delta)} \to 0 \qquad \text{and } \alpha(\delta) \to 0$$

as $\delta \to 0$, then

$$|G^\alpha(x^*, z) - G^\alpha_\delta(x^*, z)| \to 0$$

as $\delta \to 0$.

4.3 Numerical Examples

4.3.1 Reconstructions of the total field

In the first set of numerical experiments we use a frequency of $f = 500$ MHz and a wave speed $c = c_0/\sqrt{10}$, where $c_0 = 3 \times 10^8 ms^{-1}$ is the velocity of light in vacuo. This wave speed is appropriate for electromagnetic propagation in dry sandy coastal land [23], and gives a wavelength of $\lambda = c/f = 0.19$m. For all the experiments shown in this section the following holds. For each $x^* = (x_1^*, x_2^*) \in \mathbf{R}^2$, we make the choice $\Gamma_{x^*} = \{(x_1, f_{x^*}(x_1)) | x_1 \in \mathbb{R}\}$, with

$$f_{x^*}(x) = -\frac{3\lambda}{4} \exp\Big[-(\frac{x_1 - x_1^*}{8\lambda})^2 \Big] + \frac{\lambda}{4} + x_2^*,$$

so that, in particular, $f_0(x_1) = -\frac{3\lambda}{4} \exp\Big[-(\frac{x_1}{8\lambda})^2 \Big] + \frac{\lambda}{4}$. The measurement line in the inverse problem is $\gamma^* = \{(x_1, H) |\, |x_1| \leq 10\lambda = 1.9\text{m}\}$ and we fix the height of the measurement line as $H = 4\lambda = 0.76$m. We choose $h^* = x_2^* - d$ with $d = \max(f_+ - f_-, \epsilon) + \lambda/4$ and $\epsilon = \lambda/2$, and the source of the incident field is positioned at $z = (0, 4\lambda) = (0, 0.76)$m. In the numerical implementation we approximate the integral in (4.3) by the trapezium rule with step length $h = \lambda/10$ and collocate at equally spaced points x, with the same spacing h, only on the part of Γ_{x^*}, $\{x \in \Gamma_{x^*} |\, |x_1| \leq 19\lambda\}$. Numerical experiments suggest that, for this particular configuration, accuracy of reconstructions in the region below γ^* is not significantly improved by collocating on a larger part of Γ_{x^*}. This then leads to an approximation of (4.3) as a square linear system, with coefficient matrix $\mathbf{K}$. We regularise this linear system, forming the discrete analogue of (2.11), replacing K and K^* by $\mathbf{K}$ and $\mathbf{K}^*$. In Figure 4.6, for the case when $x* = (0, 3\lambda/2)$, we plot the norm of the residual and the norm of the solution as a function of the regularisation parameter α. As expected from Theorem 2.2.4 we can see that as $\alpha \to 0$ the residual $\|K\phi_{x^*}^\alpha - g_{x^*}\|_{L^2(\Gamma_{x^*})} \to 0$ but $\|\phi_{x^*}^\alpha\|_{L^2(\gamma^*)} \to \infty$, and both the norm of the residual and the norm of the solution are monotonic functions of α. Based on Figure 4.6 and similar calculations we choose

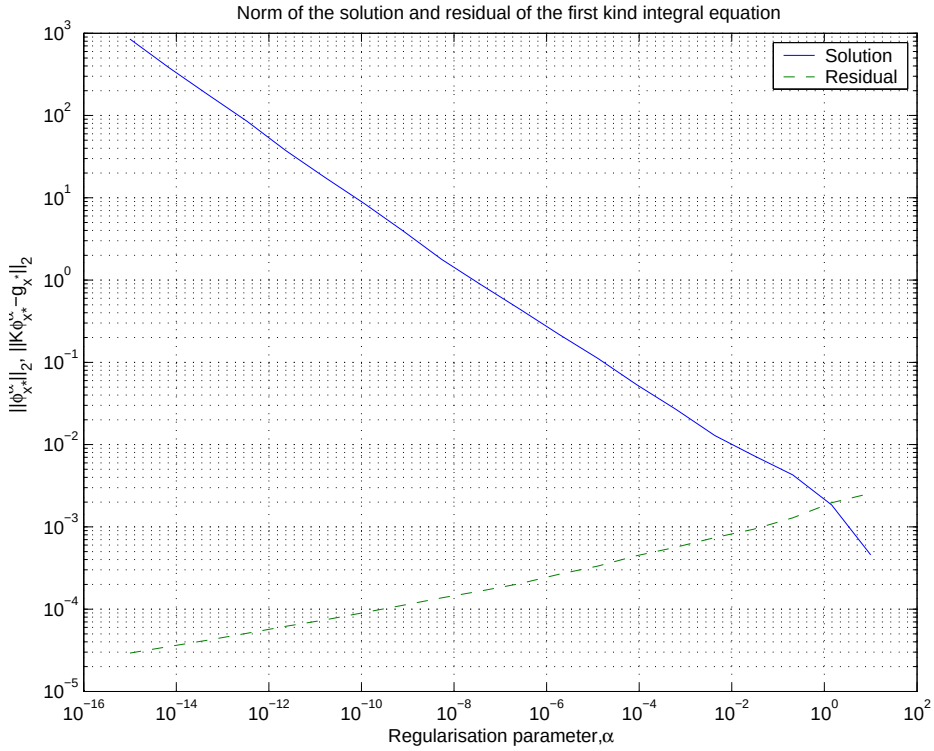

Figure 4.6: Solution of the integral equation (4.3) by Tikhonov regularisation showing the dependance of the norm of the solution, $\|\phi^{\alpha}_{x^*}\|_{L^2(\gamma^*)}$, and the norm of the residual, $\|K\phi^{\alpha}_{x^*} - g_{x^*}\|_{L^2(\Gamma_{x^*})}$, on α

$\alpha = 10^{-4}$, except where otherwise indicated, in the remainder of this thesis, since although we want the solution of the integral equation (4.3) to be as accurate as possible, if the size of $\|\phi^{\alpha}_{x^*}\|_{L^2(\gamma^*)}$ is allowed to increase too much, any errors in the measurements will be exaggerated.

In all the reconstructions shown we use "measured" values $G(x, z)$ for $x \in \gamma^*$, computed by the boundary integral equation method and super-algebraically convergent Nyström method proposed in [41], with horizontal spacing between quadrature points of $\lambda/10$, and truncating the boundary integral so that Γ is replaced by $\{x \in \Gamma | |x_1| \leq 100\lambda\}$ (see [40] for further details). Calculations of $G^{\alpha}(x, z)$ are made

for $|x_1| \leq 10\lambda$ and $f_- \leq x_2 \leq f_+$ at 5 points per wavelength (λ) in both directions with $f_- = \lambda$ and $f_+ = 3\lambda$ for the first three surfaces, and $f_- = 0$ and $f_+ = 3\lambda$ for the two higher amplitude surfaces.

In figures 4.7 to 4.11 the top left hand graphs are plots of the absolute value of the reconstructed total field, $|G^\alpha(x,z)|$, as a function of $x = (x_1, x_2)$. The bottom two plots are the real and imaginary parts of the reconstructed total field calculated using the Point Source Method, compared with the total field calculated by the super-algebraically convergent Nyström method proposed in [41]. Note that this is the same method as that used to generate the measured data for the Point Source Method. The total values are compared along the lines shown in the plots on the top right hand side of these figures. Figure 4.7 illustrates the case when

$$f(x_1) = \frac{3\lambda}{2} + \frac{\lambda}{8}\cos\Big(\frac{2x_1}{\lambda}\Big), \qquad x_1 \in \mathbf{R}, \tag{4.31}$$

so that the boundary Γ is a sinusoidal scattering surface. Figure 4.8 illustrates the case when

$$f(x_1) = \frac{3\lambda}{2} + \frac{\lambda}{4}\cos\Big(\frac{2x_1}{\lambda}\Big), \qquad x_1 \in \mathbf{R}, \tag{4.32}$$

so that the boundary Γ has twice the amplitude of the first surface, and we double the amplitude again for the case shown in Figure 4.9, using

$$f(x_1) = \frac{3\lambda}{2} + \frac{\lambda}{2}\cos\Big(\frac{2x_1}{\lambda}\Big), \qquad x_1 \in \mathbf{R}. \tag{4.33}$$

In figures 4.10 and 4.15 we investigate the behaviour of the Point Source Method for non-sinusoidal surfaces, with

$$f(x_1) = \frac{3\lambda}{2} + \frac{\lambda}{8}\cos\Big(\frac{2x_1}{\lambda}\Big) + \frac{\lambda}{4}\sin\Big(\frac{2x_1}{3\lambda}\Big), \qquad x_1 \in \mathbf{R}, \tag{4.34}$$

and, for the case illustrated in figures 4.11 and 4.16,

$$f(x_1) = \frac{3\lambda}{2} + \frac{\lambda}{4}\cos(\frac{2x_1}{\lambda}) + \frac{\lambda}{4}\sin(\frac{2x_1}{3\lambda}) \qquad x_1 \in \mathbf{R}. \tag{4.35}$$

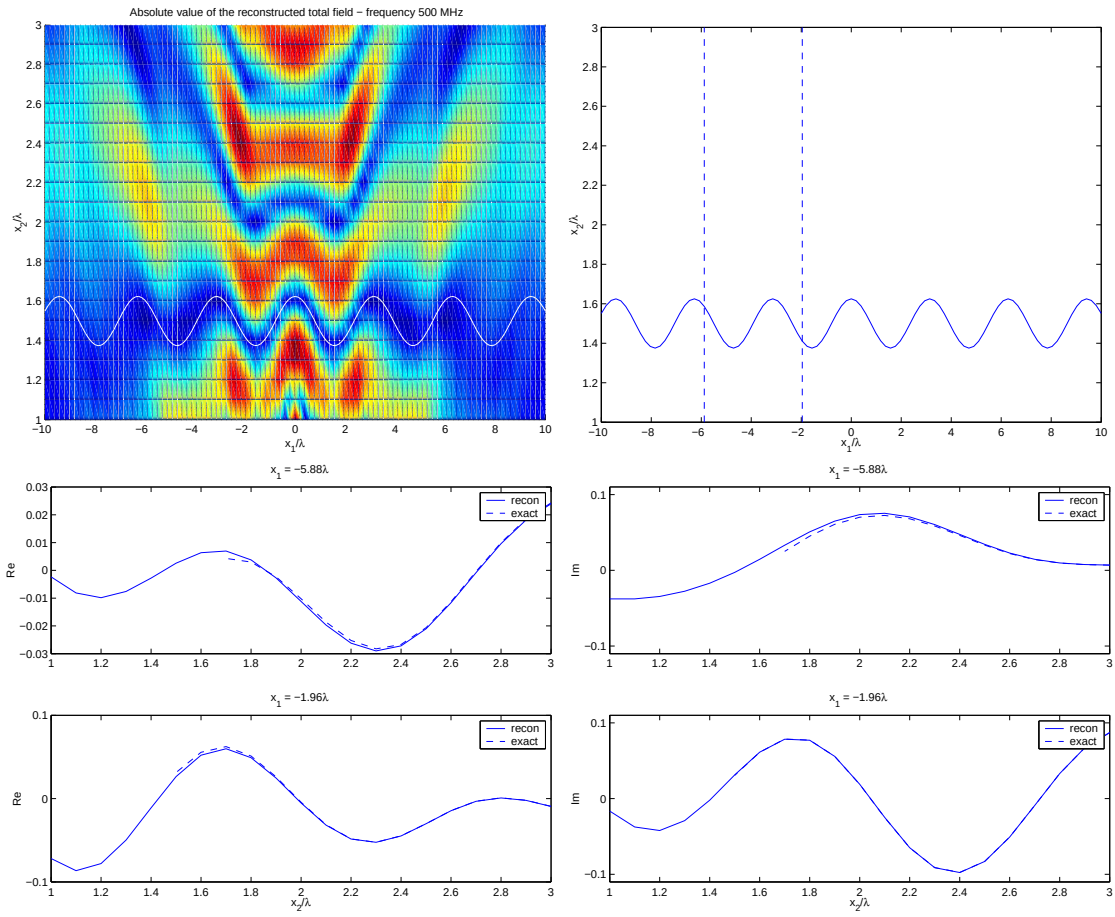

Figure 4.7: Results for $f = 500$MHz and the sinusoidal surface (4.31) shown in the top right figure. Absolute value of the reconstructed total field, $|G^\alpha(x,z)|$ (top left). Lower figures compare the reconstructed total field, $G^\alpha(x,z)$, and the exact field, $G(x,z)$, on the lines shown in the top right figure. Plotted are $\Re(G^\alpha(x,z))$ and $\Re(G(x,z))$ (left hand side) and $\Im(G^\alpha(x,z))$ and $\Im(G(x,z))$ (right hand side).

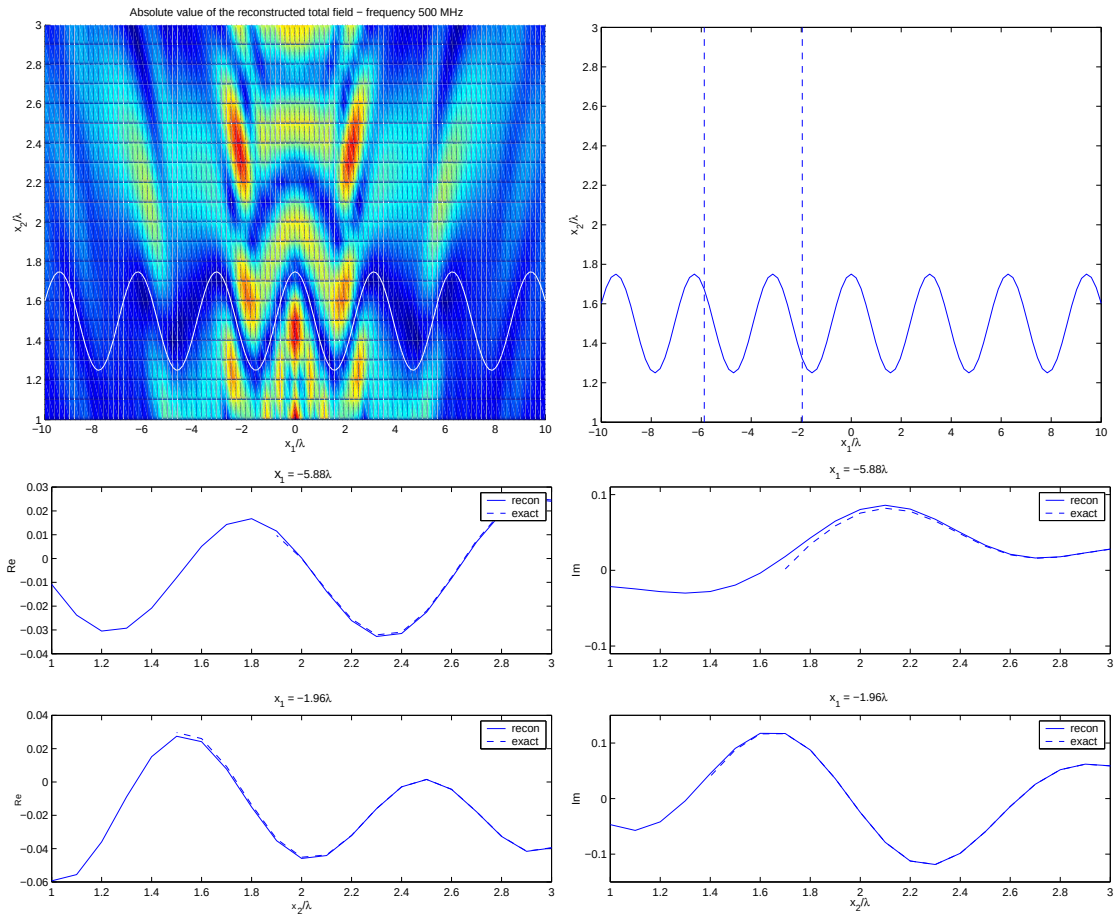

Figure 4.8: Results for $f = 500$MHz and the sinusoidal surface (4.32) shown in the top right figure. Absolute value of the reconstructed total field, $|G^\alpha(x,z)|$ (top left). Lower figures compare the reconstructed total field, $G^\alpha(x,z)$, and the exact field, $G(x,z)$, on the lines shown in the top right figure. Plotted are $\Re(G^\alpha(x,z))$ and $\Re(G(x,z))$ (left hand side) and $\Im(G^\alpha(x,z))$ and $\Im(G(x,z))$ (right hand side).

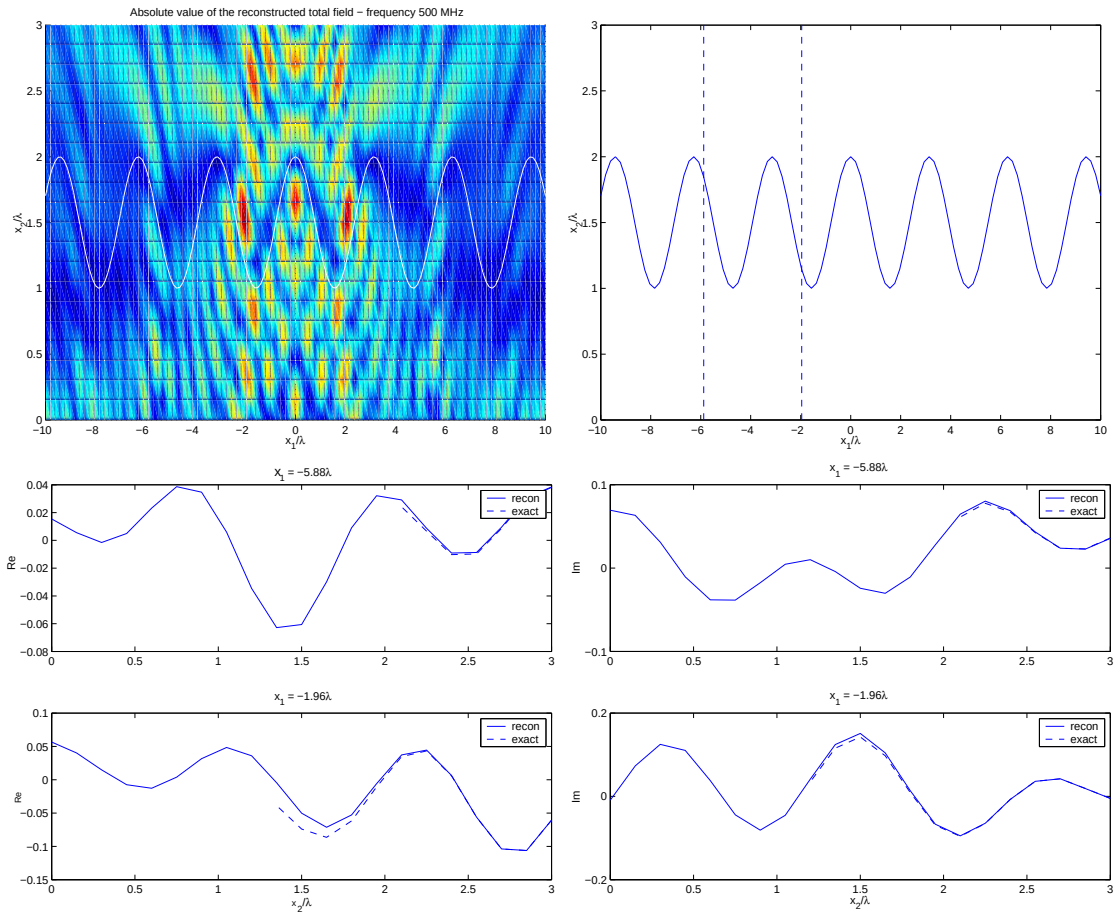

Figure 4.9: Results for $f = 500$MHz and the sinusoidal surface (4.33) shown in the top right figure. Absolute value of the reconstructed total field, $|G^\alpha(x,z)|$ (top left). Lower figures compare the reconstructed total field, $G^\alpha(x,z)$, and the exact field, $G(x,z)$, on the lines shown in the top right figure. Plotted are $\Re(G^\alpha(x,z))$ and $\Re(G(x,z))$ (left hand side) and $\Im(G^\alpha(x,z))$ and $\Im(G(x,z))$ (right hand side).

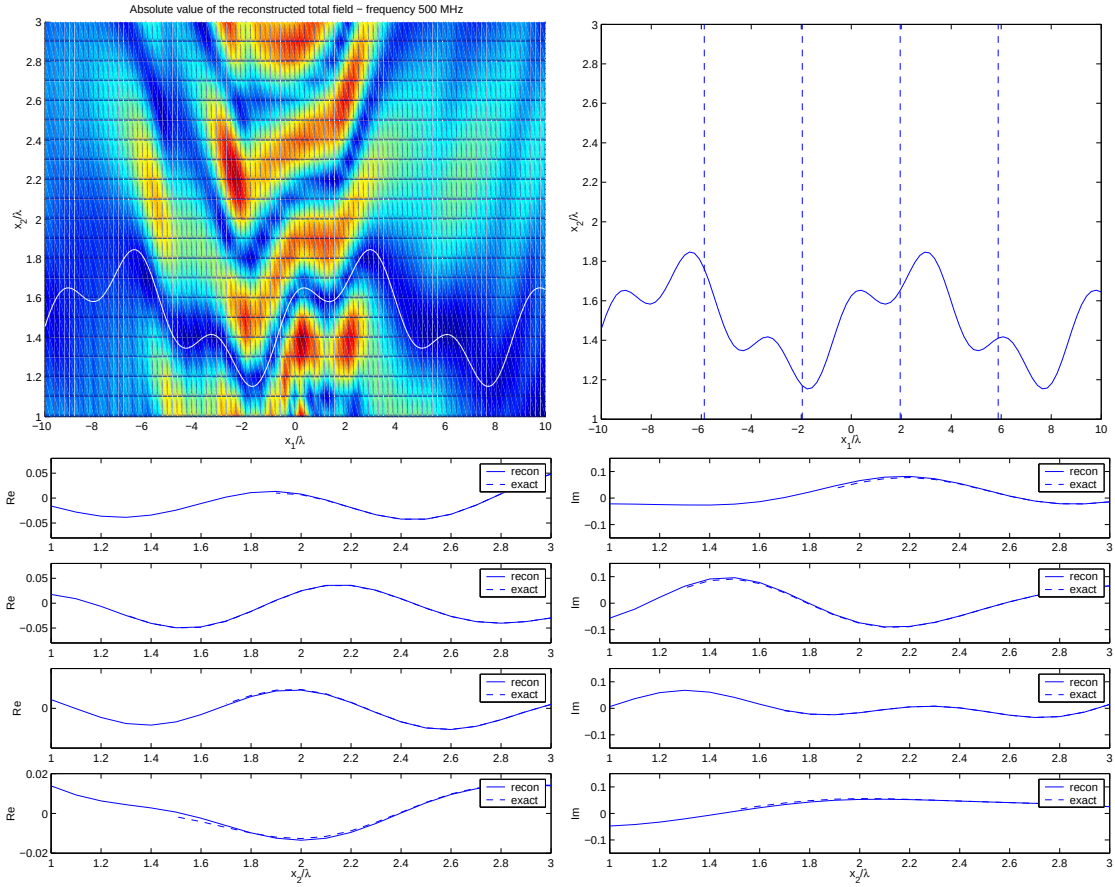

Figure 4.10: Results for $f = 500$MHz and the rough surface (4.34) shown in the top right figure. Absolute value of the reconstructed total field, $|G^\alpha(x,z)|$ (top left). Lower figures compare the reconstructed total field, $G^\alpha(x,z)$, and the exact field, $G(x,z)$, on the lines shown in the top right figure, namely at (from top to bottom) $x_1 = -5.88\lambda$, $x_1 = -1.96\lambda$, $x_1 = 1.96\lambda$ and $x_1 = 5.88\lambda$. Plotted are $\Re(G^\alpha(x,z))$ and $\Re(G(x,z))$ (left hand side) and $\Im(G^\alpha(x,z))$ and $\Im(G(x,z))$ (right hand side).

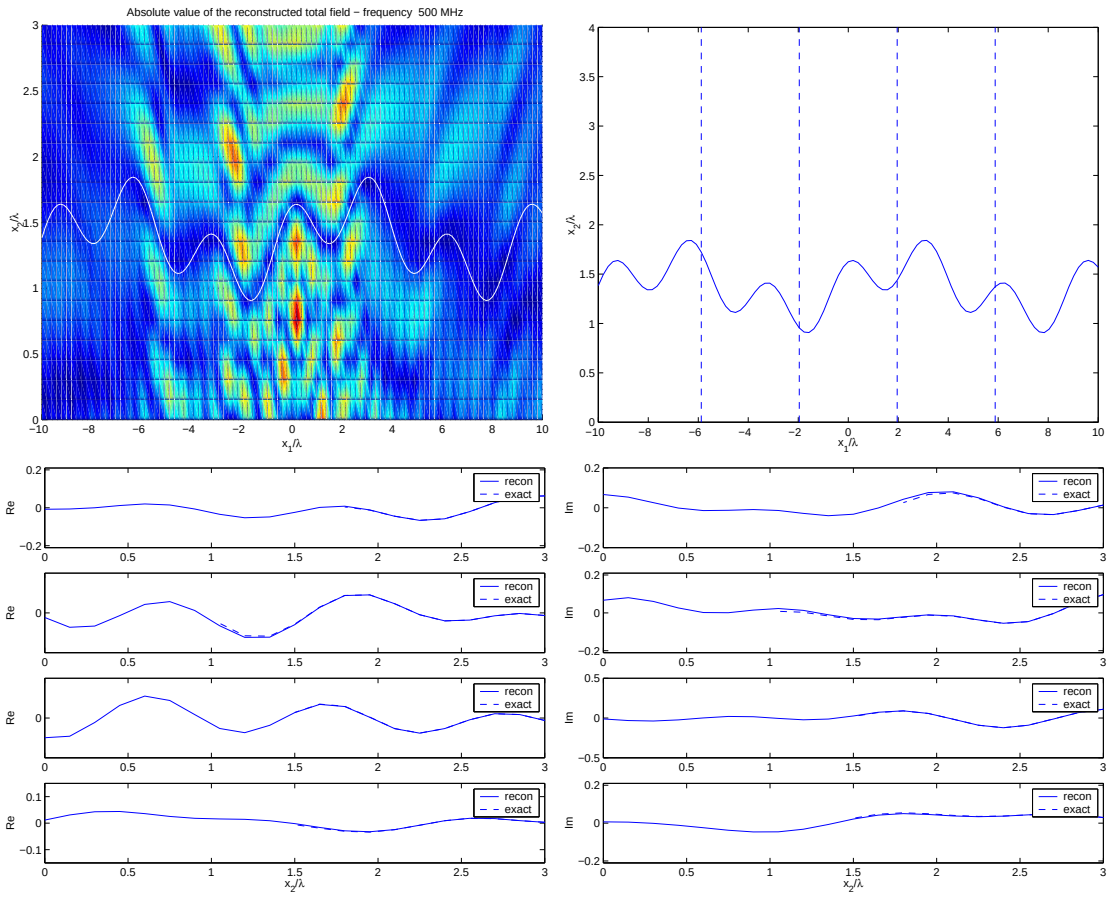

Figure 4.11: Results for $f = 500$MHz and the rough surface (4.35) shown in the top right figure. Absolute value of the reconstructed total field, $|G^\alpha(x,z)|$ (top left). Lower figures compare the reconstructed total field, $G^\alpha(x,z)$, and the exact field, $G(x,z)$, on the lines shown in the top right figure, namely at (from top to bottom) $x_1 = -5.88\lambda$, $x_1 = -1.96\lambda$, $x_1 = 1.96\lambda$ and $x_1 = 5.88\lambda$. Plotted are $\Re(G^\alpha(x,z))$ and $\Re(G(x,z))$ (left hand side) and $\Im(G^\alpha(x,z))$ and $\Im(G(x,z))$ (right hand side).

In figures 4.12 to 4.16 we compare the noisy reconstructed total field $G_\delta^\alpha(x,y)$ with the exact total field $G(x,z)$, calculated as before. Note that when noise is added, each measured value of $G(x,z)$ is replaced by $G_\delta(x,z) = G(x,z) + N(x)$, where $N(x)$ and $N(y)$ are independently distributed for $x \neq y$, and where, for each x, the real and imaginary parts of $N(x)$ are independently and identically normally distributed with mean 0 and standard deviation chosen such that $\sqrt{E(|N(x)|^2)} = \frac{\delta^*}{100}|\Phi(x,z)|$, where δ^* is the specified percentage error. Note that the relationship between $\delta = \|N\|_{L^2(\gamma^*)}$ and δ^* is that

$$\begin{aligned} E(\delta^2) &= \int_{\gamma^*} E(|N(x)|^2)\mathrm{ds}(x) \\ &= \left(\frac{\delta^*}{100}\right)^2 \int_{\gamma^*} |\Phi(x,z)|^2 \mathrm{ds}(x), \end{aligned} \tag{4.36}$$

i.e.

$$\sqrt{E(\delta^2)} = \frac{\delta^*}{100}\|\Phi(\cdot,z)\|_{L^2(\gamma^*)}.$$

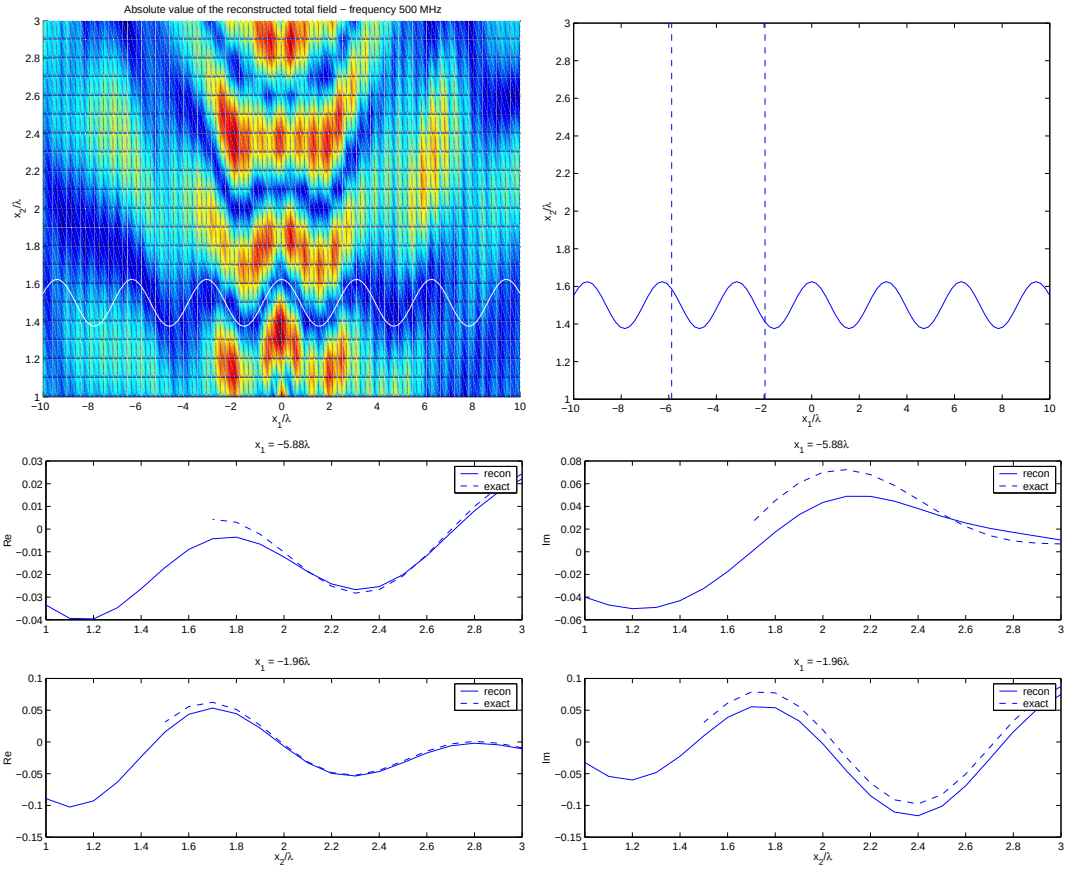

Figure 4.12: Results for $f = 500$MHz and the sinusoidal surface (4.31) shown in the top right figure. Absolute value of the noisy reconstructed total field, $|G^{\alpha}_{\delta}(x,z)|$, with $\delta^* = 5$, (top left). Lower figures compare the reconstructed total field, $G^{\alpha}_{\delta}(x,z)$, and the exact field, $G(x,z)$, on the lines shown in the top right figure. Plotted are $\Re(G^{\alpha}_{\delta}(x,z))$ and $\Re(G(x,z))$ (left hand side) and $\Im(G^{\alpha}_{\delta}(x,z))$ and $\Im(G(x,z))$ (right hand side).

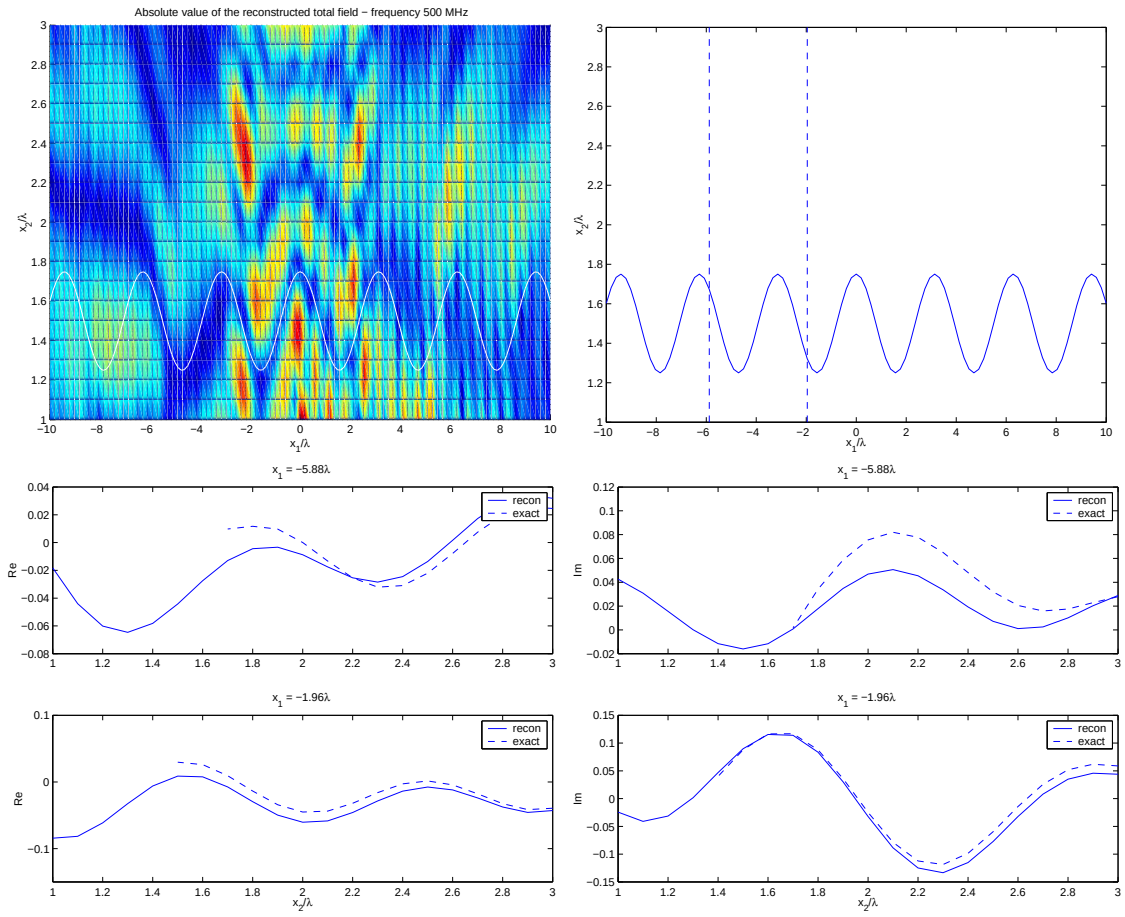

Figure 4.13: Results for $f = 500$MHz and the sinusoidal surface (4.32) shown in the top right figure. Absolute value of the noisy reconstructed total field, $|G_\delta^\alpha(x,z)|$, with $\delta^* = 5$, (top left). Lower figures compare the reconstructed total field, $G_\delta^\alpha(x,z)$, and the exact field, $G(x,z)$, on the lines shown in the top right figure. Plotted are $\Re(G_\delta^\alpha(x,z))$ and $\Re(G(x,z))$ (left hand side) and $\Im(G_\delta^\alpha(x,z))$ and $\Im(G(x,z))$ (right hand side).

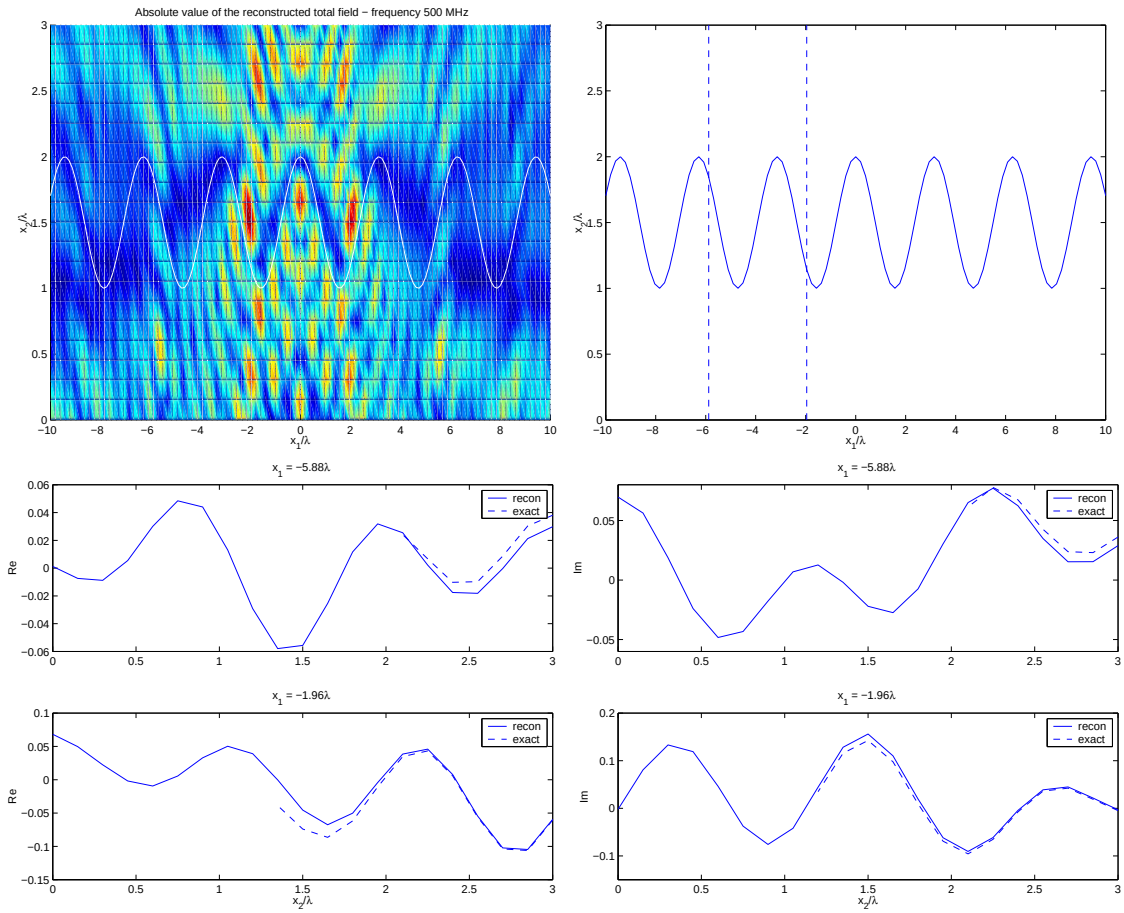

Figure 4.14: Results for $f = 500$MHz and the sinusoidal surface (4.33) shown in the top right figure. Absolute value of the noisy reconstructed total field, $|G^{\alpha}_{\delta}(x,z)|$, with $\delta^* = 5$, (top left). Lower figures compare the reconstructed total field, $G^{\alpha}_{\delta}(x,z)$, and the exact field, $G(x,z)$, on the lines shown in the top right figure. Plotted are $\Re(G^{\alpha}_{\delta}(x,z))$ and $\Re(G(x,z))$ (left hand side) and $\Im(G^{\alpha}_{\delta}(x,z))$ and $\Im(G(x,z))$ (right hand side).

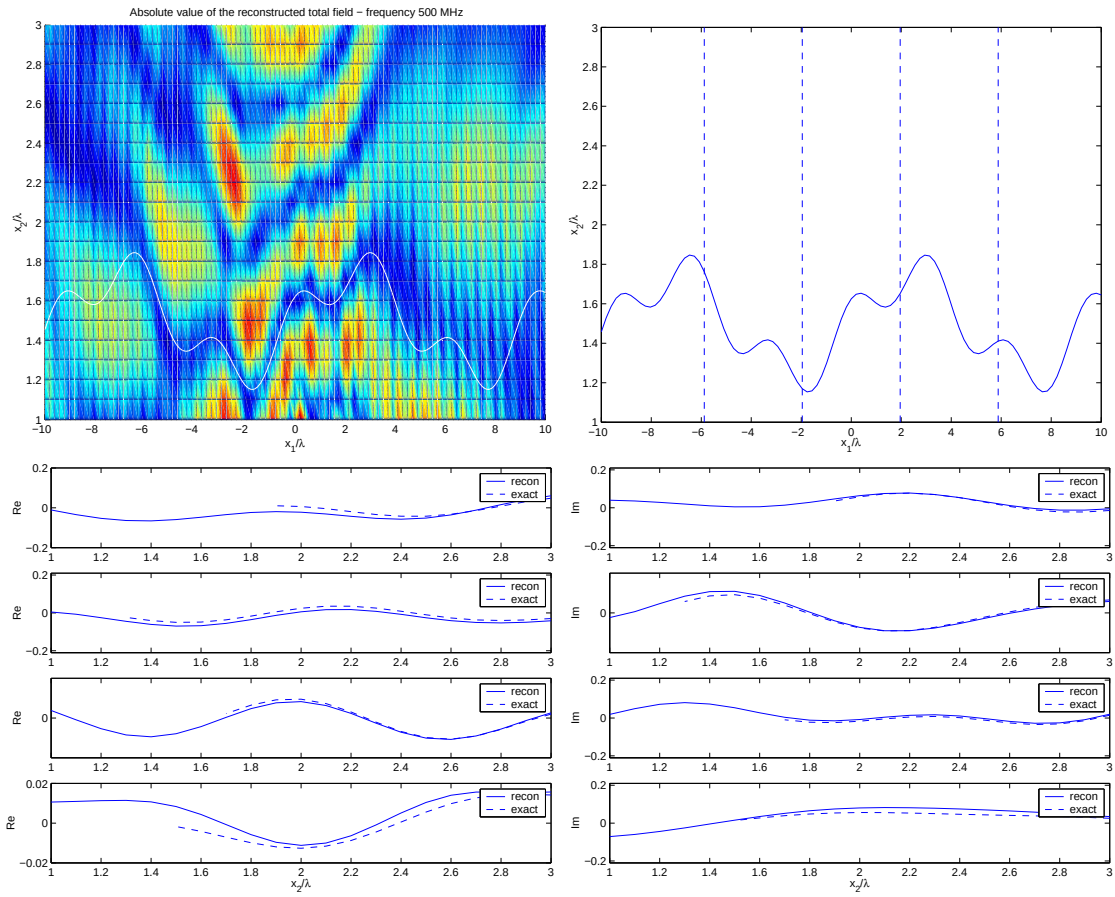

Figure 4.15: Results for $f = 500$MHz and the rough surface (4.34) shown in the top right figure. Absolute value of the noisy reconstructed total field, $|G_\delta^\alpha(x,z)|$, with $\delta^* = 5$, (top left). Lower figures compare the reconstructed total field, $G_\delta^\alpha(x,z)$, and the exact field, $G(x,z)$, on the lines shown in the top right figure, namely at (from top to bottom) $x_1 = -5.88\lambda$, $x_1 = -1.96\lambda$, $x_1 = 1.96\lambda$ and $x_1 = 5.88\lambda$. Plotted are $\Re(G_\delta^\alpha(x,z))$ and $\Re(G(x,z))$ (left hand side) and $\Im(G_\delta^\alpha(x,z))$ and $\Im(G(x,z))$ (right hand side).

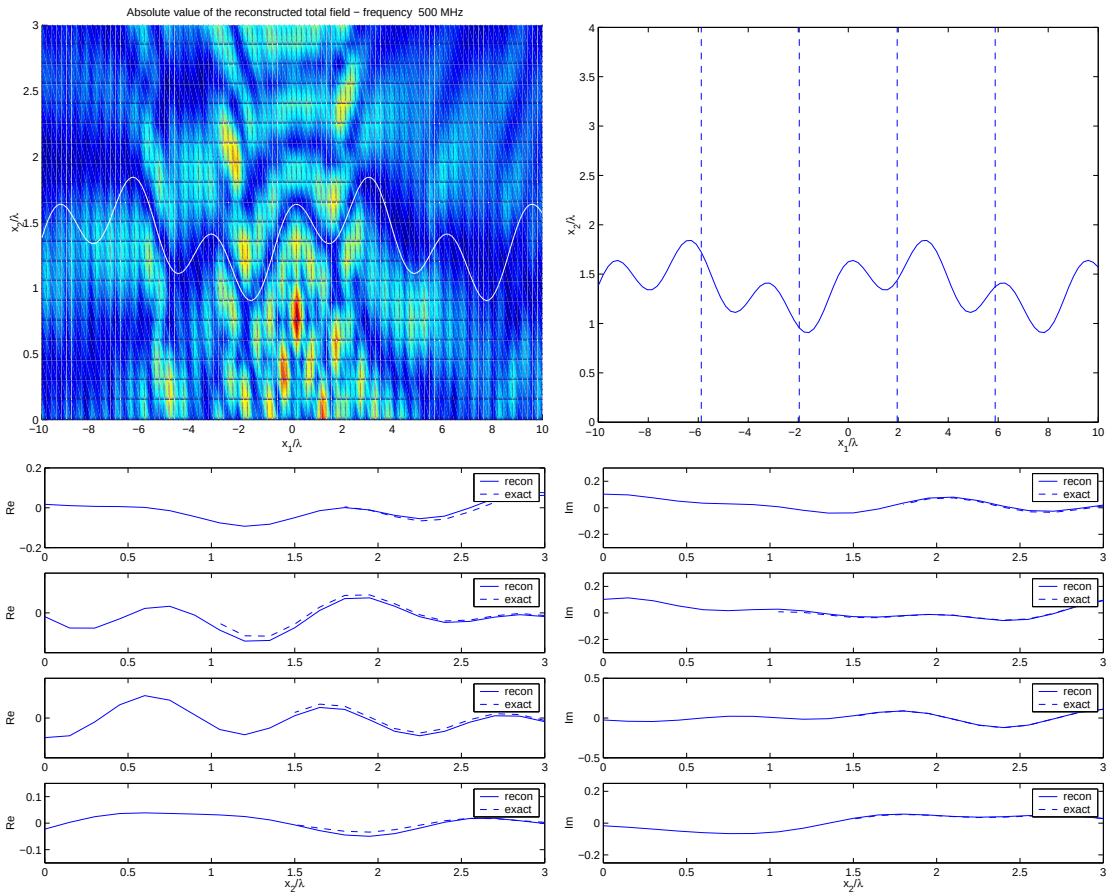

Figure 4.16: Results for $f = 500$MHz and the rough surface (4.35) shown in the top right figure. Absolute value of the noisy reconstructed total field, $|G_\delta^\alpha(x,z)|$, with $\delta^* = 5$, (top left). Lower figures compare the reconstructed total field, $G_\delta^\alpha(x,z)$, and the exact field, $G(x,z)$, on the lines shown in the top right figure, namely at (from top to bottom) $x_1 = -5.88\lambda$, $x_1 = -1.96\lambda$, $x_1 = 1.96\lambda$ and $x_1 = 5.88\lambda$. Plotted are $\Re(G_\delta^\alpha(x,z))$ and $\Re(G(x,z))$ (left hand side) and $\Im(G_\delta^\alpha(x,z))$ and $\Im(G(x,z))$ (right hand side).

Conclusions

The figures show that, with $\alpha = 10^{-4}$ taken and the geometry described above, the point source reconstruction of the total field, $G^{\alpha}(x, z)$, agrees well with the exact total field $G(x, z)$. Reconstructions have been carried out for three sinusoidal surfaces increasing in peak-to-trough amplitude from $\lambda/4$ to λ and two non-sinusoidal surfaces of peak-to-trough amplitudes $\frac{3\lambda}{4}$ and λ. The reconstructions get slightly worse the more we increase the amplitude. When 5% noise is added to the measurements the reconstructions still agree well with the exact values of the total field. The accuracy of the reconstructions worsen as $|x_1|$ increases towards its value at the end of the measurement line, i.e. as $|x_1|$ approaches 10λ.

4.3.2 Surface Predictions

In the second set of numerical experiments we reconstruct the total field and predict the location of the surface using data from three frequencies, namely $500/\sqrt{2}$ MHz, 500 MHz, and $500\sqrt{2}$ MHz, which have wavenumbers $k_1 = 23.4\text{m}^{-1}$, $k = 33.1\text{m}^{-1}$ and $k_3 = 46.8\text{m}^{-1}$, and wavelengths $\lambda_1 = 0.2683$m, $\lambda = 0.1897$m and $\lambda_3 = 0.1342$m, respectively. Denote $G^{\alpha}(x, z)$ by $G^{\alpha}_k(x, z)$ to indicate its dependence on k. In figures 4.17, 4.19 and 4.23 we plot the absolute value of the reconstructed total fields, $|G^{\alpha}_k(x, z)|$, for the three surfaces given above, as a function of $x = (x_1, x_2)$. Calculations of $G^{\alpha}_k(x, z)$ are made for $|x_1| \leq 10\lambda$ and $\lambda \leq x_2 \leq 3\lambda$, at 5 points per wavelength (λ) in both directions, for the surfaces (4.31), (4.32) and (4.34). For the higher amplitude surfaces (4.33) and (4.35) calculations of $G^{\alpha}_k(x, z)$ are made for $|x_1| \leq 10\lambda$ and $0 \leq x_2 \leq 3\lambda$, at 5 points per wavelength (λ) in both directions. In the bottom right hand plot of each figure we plot a weighted sum of squares of the reconstructed total fields, $G_{\Sigma}(x, z)$, given by

$$G_{\Sigma}(x, z) = \frac{\lambda}{\lambda_1}|G^{\alpha}_{k_1}(x, z)|^2 + |G^{\alpha}_k(x, z)|^2 + \frac{\lambda}{\lambda_3}|G^{\alpha}_{k_3}(x, z)|^2. \tag{4.37}$$

In figures 4.18, 4.20, 4.22, 4.24 and 4.26 to 4.31 we predict the location of the surface using two different methods. In both methods we utilize the a priori knowledge that the total field vanishes on the boundary. Denote $\Phi(x,z)$ by $\Phi_k(x,z)$ to indicate its dependence on k. In the first method (on the right hand side) we colour in black the squares for which

$$G_\Sigma(x,z) \leq \epsilon \Phi_\Sigma(x,z),$$

where

$$\Phi_\Sigma(x,z) = \frac{\lambda}{\lambda_1}|\Phi_{k_1}(x,z)|^2 + |\Phi_k(x,z)|^2 + \frac{\lambda}{\lambda_3}|\Phi_{k_3}(x,z)|^2,$$

and ϵ is as specified in the figure caption. During the remainder of this thesis we will refer to this method as 'Method A'. In the second method (on the left hand side) in each column we colour in black the square in which $G_\Sigma(x,z)$ is minimised as a function of x_2. We refer to this method as 'Method B'. In the bottom plots we interpolate the values of $G_\Sigma(x,z)$ from 5 points per wavelength (λ) to 10 points per wavelength (λ) before invoking either one of the two methods.

In figures 4.27, 4.28, 4.29, 4.30 and 4.31 we plot the noisy reconstructed total field $G^\alpha_{\Sigma,\delta}(x,z)$ given by

$$G_{\Sigma,\delta}(x,z) = \frac{\lambda}{\lambda_1}|G^\alpha_{\delta,k_1}(x,z)|^2 + |G^\alpha_{\delta,k}(x,z)|^2 + \frac{\lambda}{\lambda_3}|G^\alpha_{\delta,k_3}(x,z)|^2,$$

where $\delta^* = 5$, i.e. with 5% noise added to the measurements. The reconstructions are calculated at 5 points per wavelength (λ) in both directions. Along with the reconstruction of the total field, predictions of the surface location are made using the methods described in the previous paragraph.

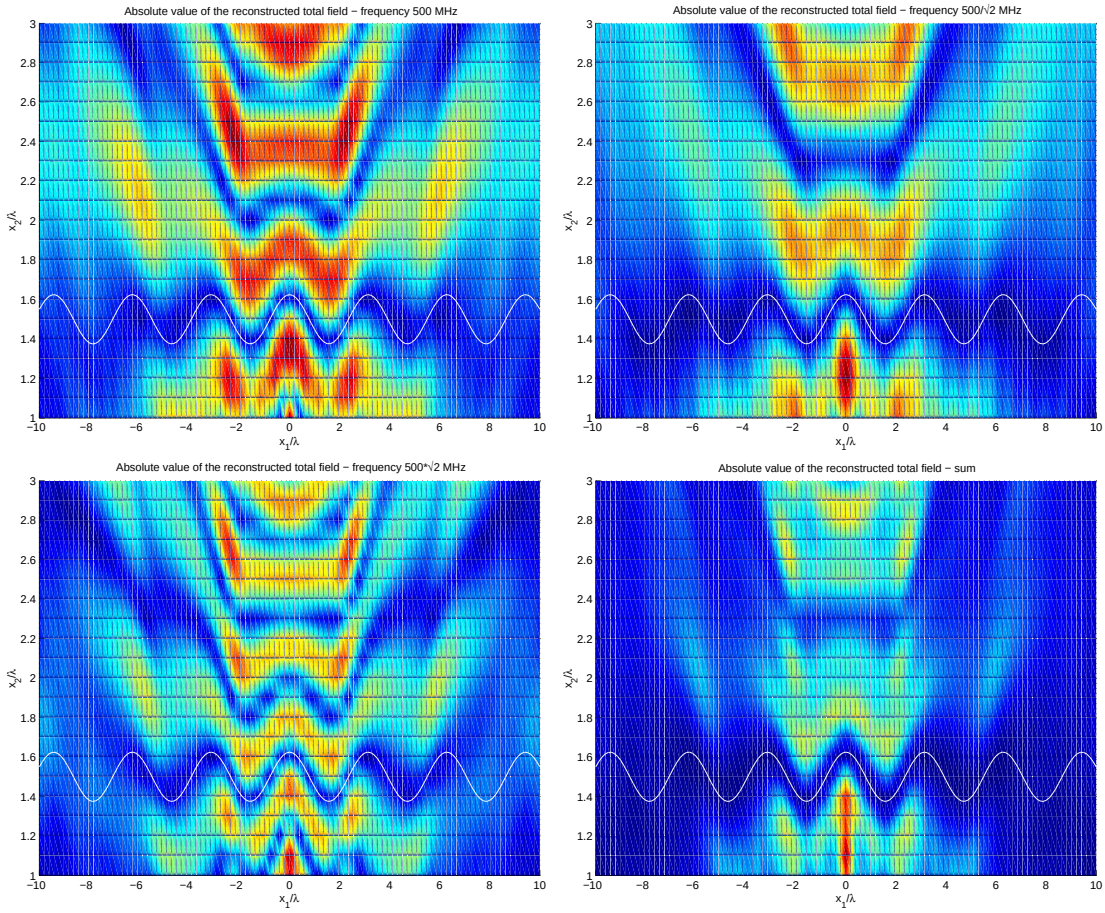

Figure 4.17: The absolute value of the reconstructed total field, $|G_k^\alpha(x,z)|$, for $k = 46.8\text{m}^{-1}$ (bottom left), $k = 33.1\text{m}^{-1}$ (top left) and $k = 23.4\text{m}^{-1}$ (top right) i.e. frequencies $500\sqrt{2}$MHz, 500MHz and $500/\sqrt{2}$MHz respectively, for surface (4.31). Also shown is $G_\Sigma(x,z)$ given by (4.37) (bottom right).

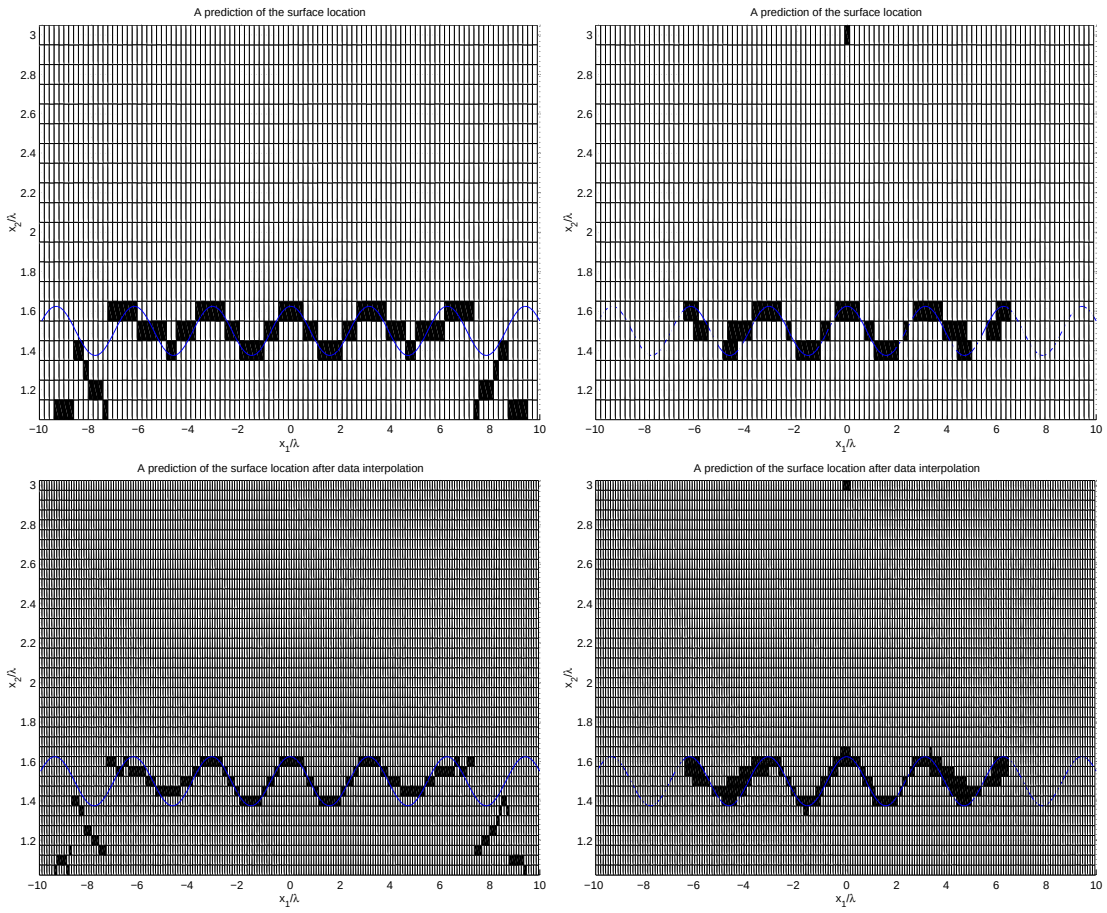

Figure 4.18: Shown are the predictions of the surface location for surface (4.31) using Method A with $\epsilon = 0.17$ (right hand side) and Method B (left hand side). The bottom plots interpolate $G_\Sigma(x, z)$ before invoking either method.

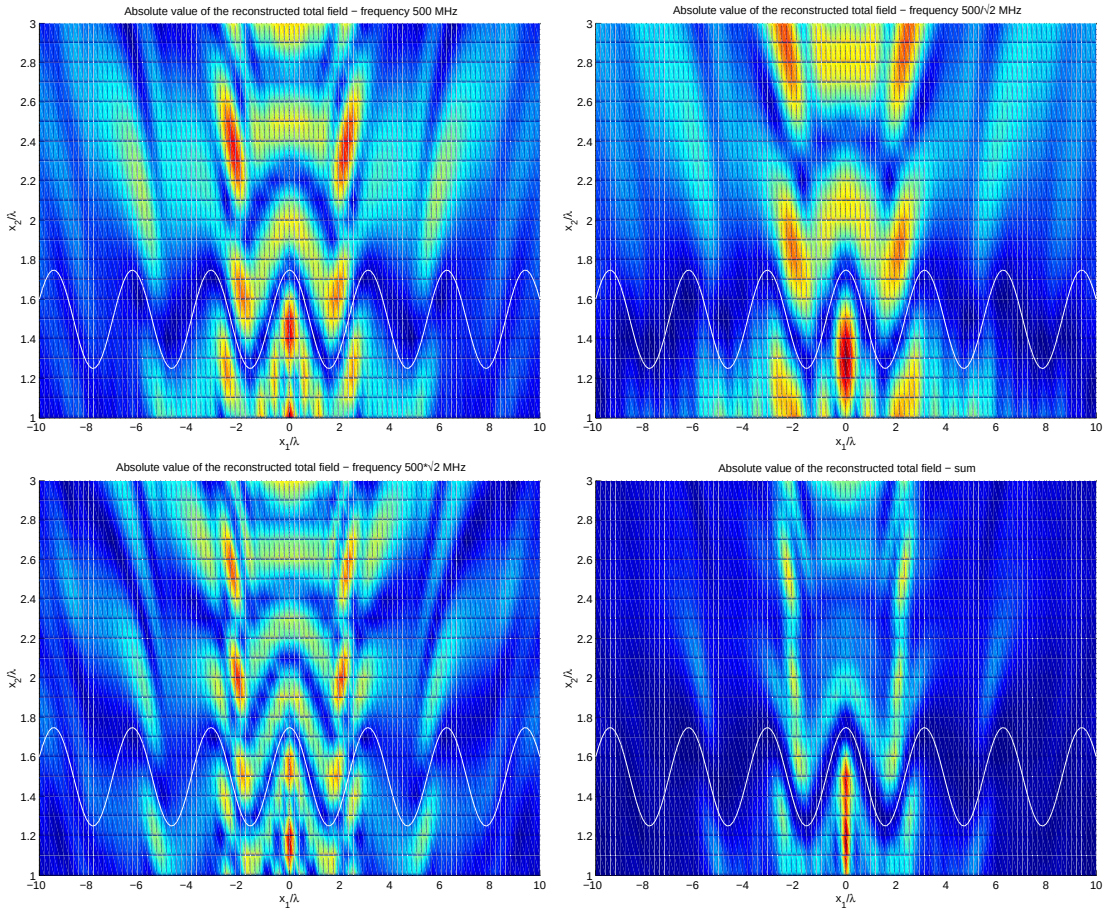

Figure 4.19: The absolute value of the reconstructed total field, $|G_k^\alpha(x,z)|$, for $k = 46.8\text{m}^{-1}$ (bottom left), $k = 33.1\text{m}^{-1}$ (top left) and $k = 23.4\text{m}^{-1}$ (top right) i.e. frequencies $500\sqrt{2}$MHz, 500MHz and $500/\sqrt{2}$MHz respectively, for surface (4.32). Also shown is $G_\Sigma(x,z)$ given by (4.37) (bottom right).

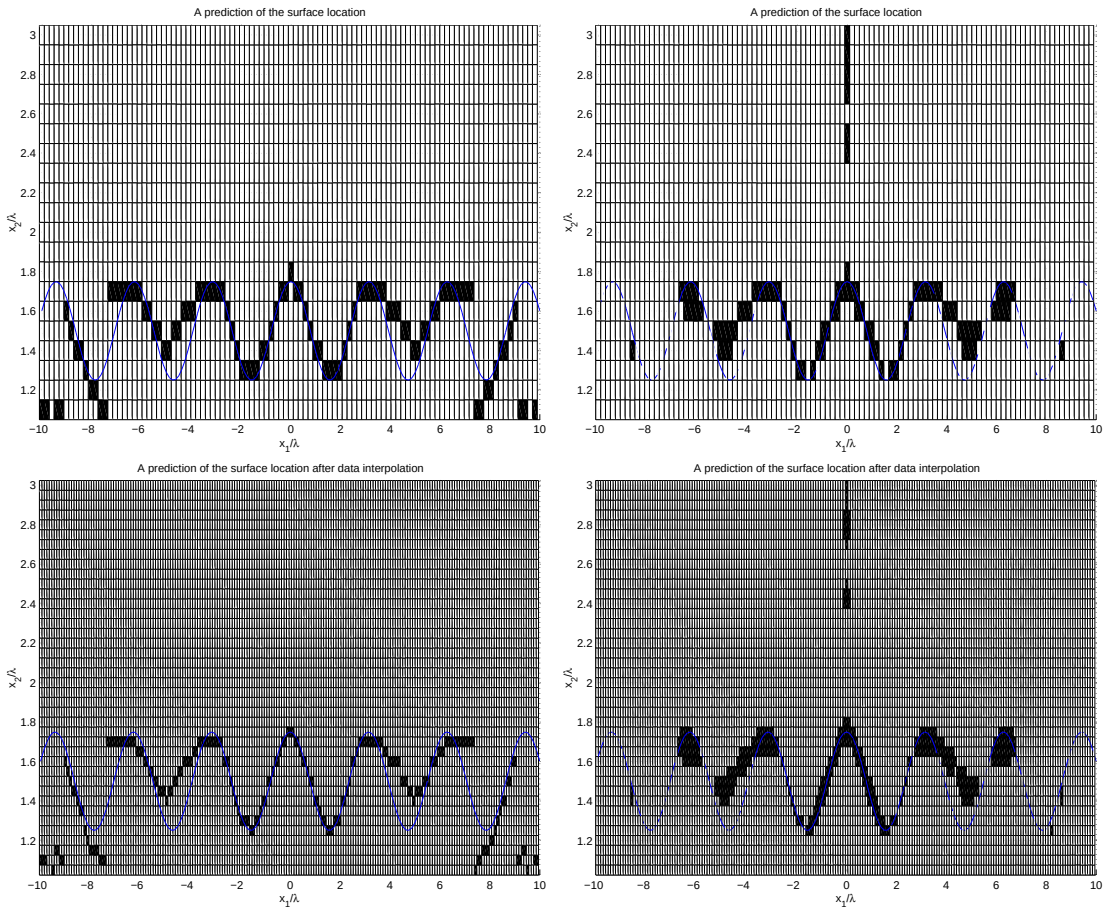

Figure 4.20: Shown are the predictions of the surface location for surface (4.32) using Method A with $\epsilon = 0.33$ (right hand side) and Method B (left hand side). The bottom plots interpolate $G_\Sigma(x, z)$ before invoking either method.

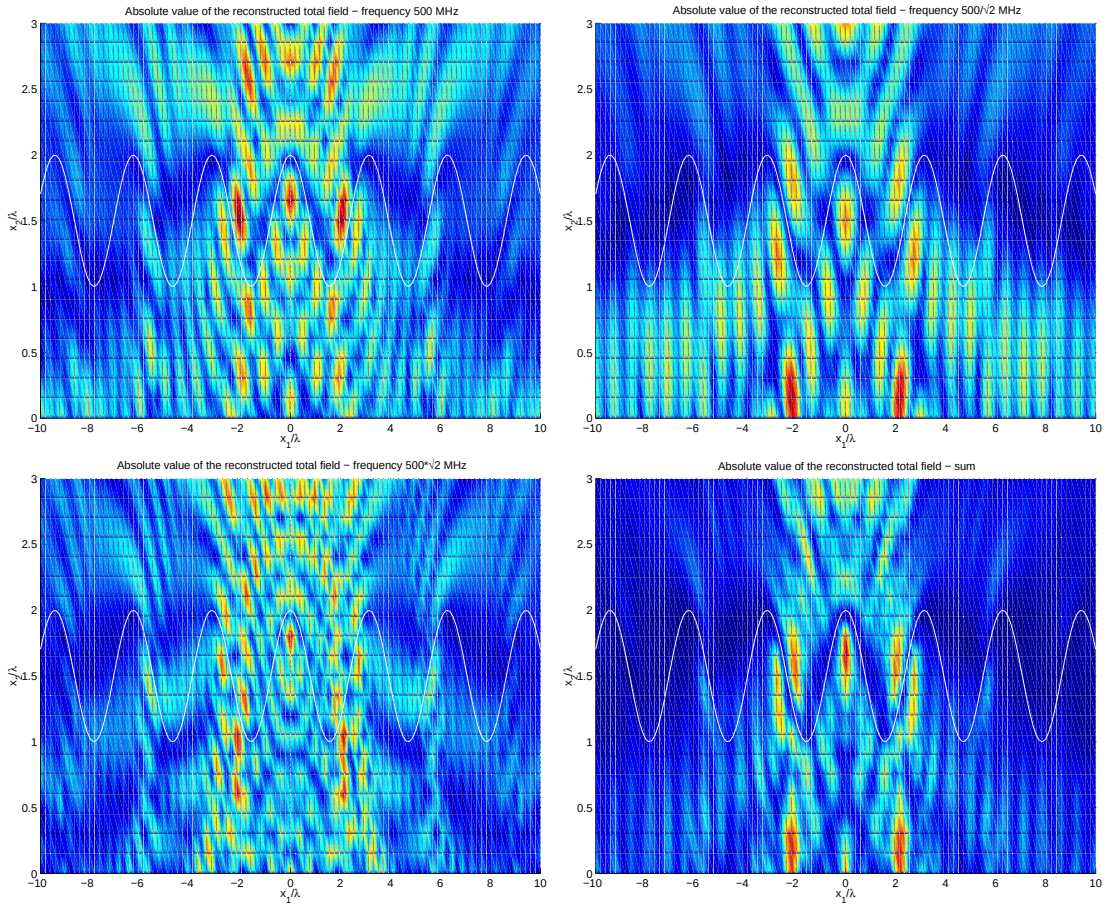

Figure 4.21: The absolute value of the reconstructed total field, $|G_k^\alpha(x,z)|$, for $k = 46.8\text{m}^{-1}$ (bottom left), $k = 33.1\text{m}^{-1}$ (top left) and $k = 23.4\text{m}^{-1}$ (top right) i.e. frequencies $500\sqrt{2}$MHz, 500MHz and $500/\sqrt{2}$MHz respectively, for surface (4.33). Also shown is $G_\Sigma(x,z)$ given by (4.37) (bottom right).

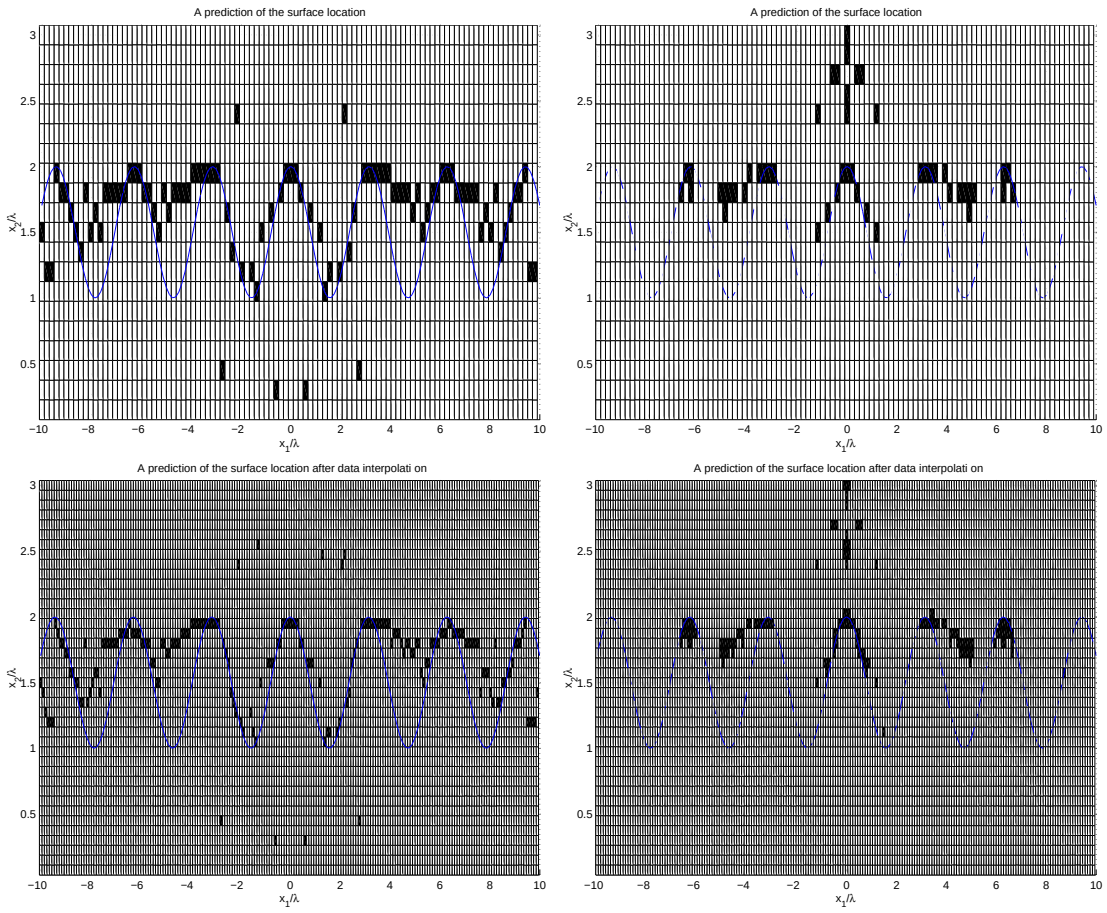

Figure 4.22: Shown are the predictions of the surface location for surface (4.33) using Method A with $\epsilon = 0.35$ (right hand side) and Method B (left hand side). The bottom plots interpolate $G_\Sigma(x, z)$ before invoking either method.

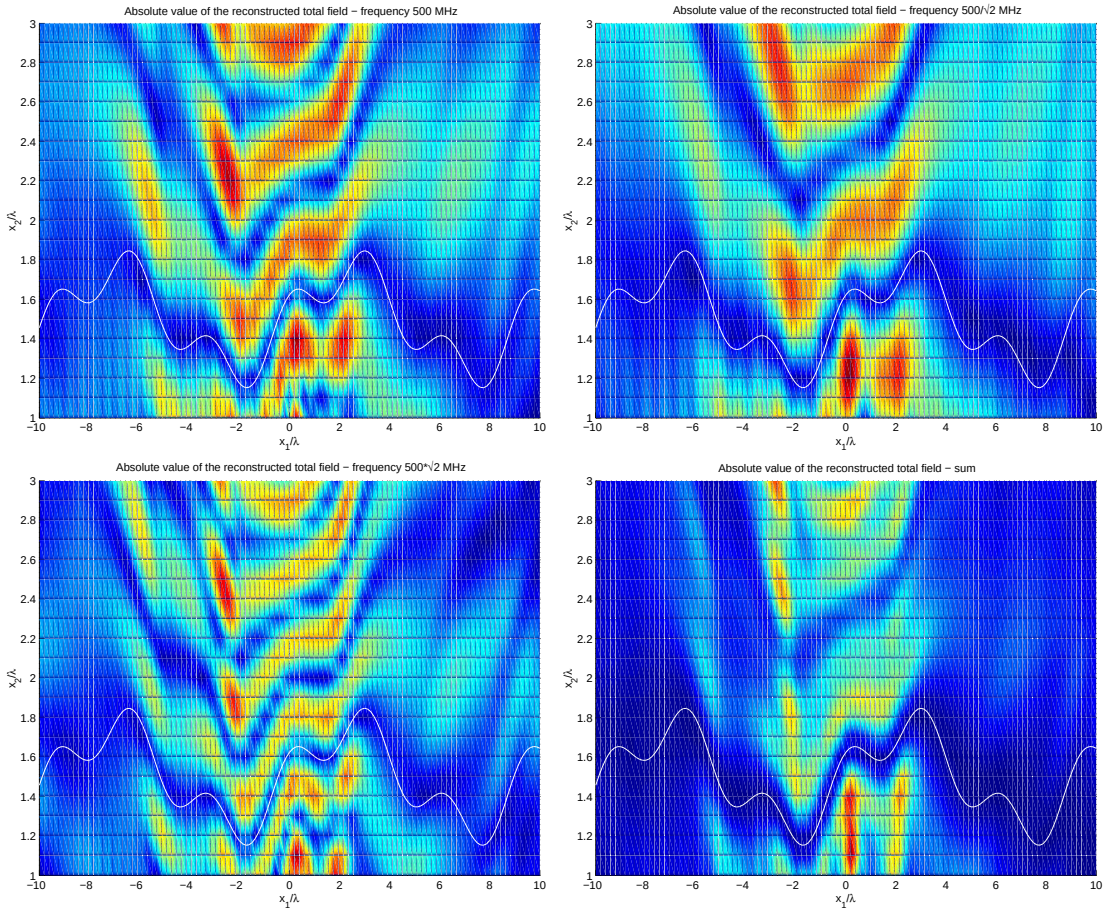

Figure 4.23: The absolute value of the reconstructed total field, $|G_k^\alpha(x,z)|$, for $k = 46.8\text{m}^{-1}$ (bottom left), $k = 33.1\text{m}^{-1}$ (top left) and $k = 23.4\text{m}^{-1}$ (top right) i.e. frequencies $500\sqrt{2}$MHz, 500MHz and $500/\sqrt{2}$MHz respectively, for surface (4.34). Also shown is $G_\Sigma(x,z)$ given by (4.37) (bottom right).

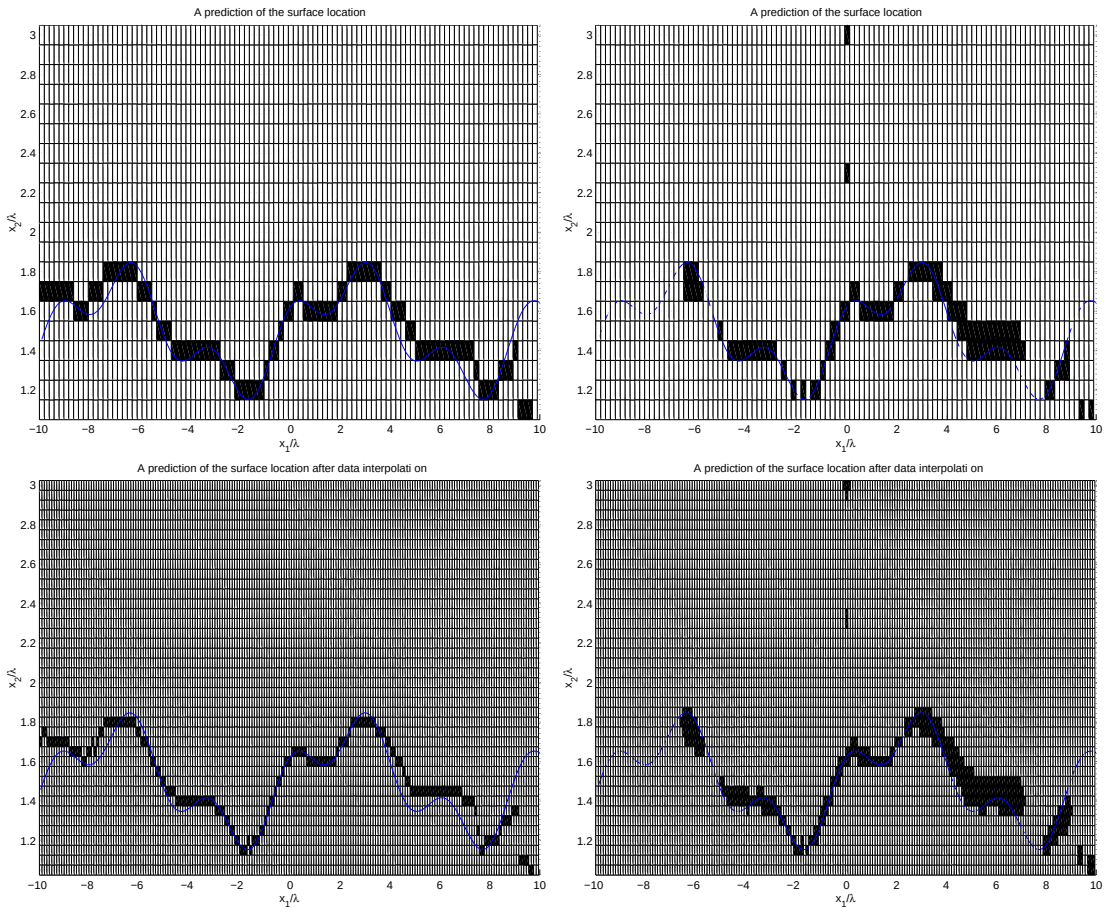

Figure 4.24: Shown are the predictions of the surface location for surface (4.34) using Method A with $\epsilon = 0.25$ (right hand side) and Method B (left hand side). The bottom plots interpolate $G_\Sigma(x, z)$ before invoking either method.

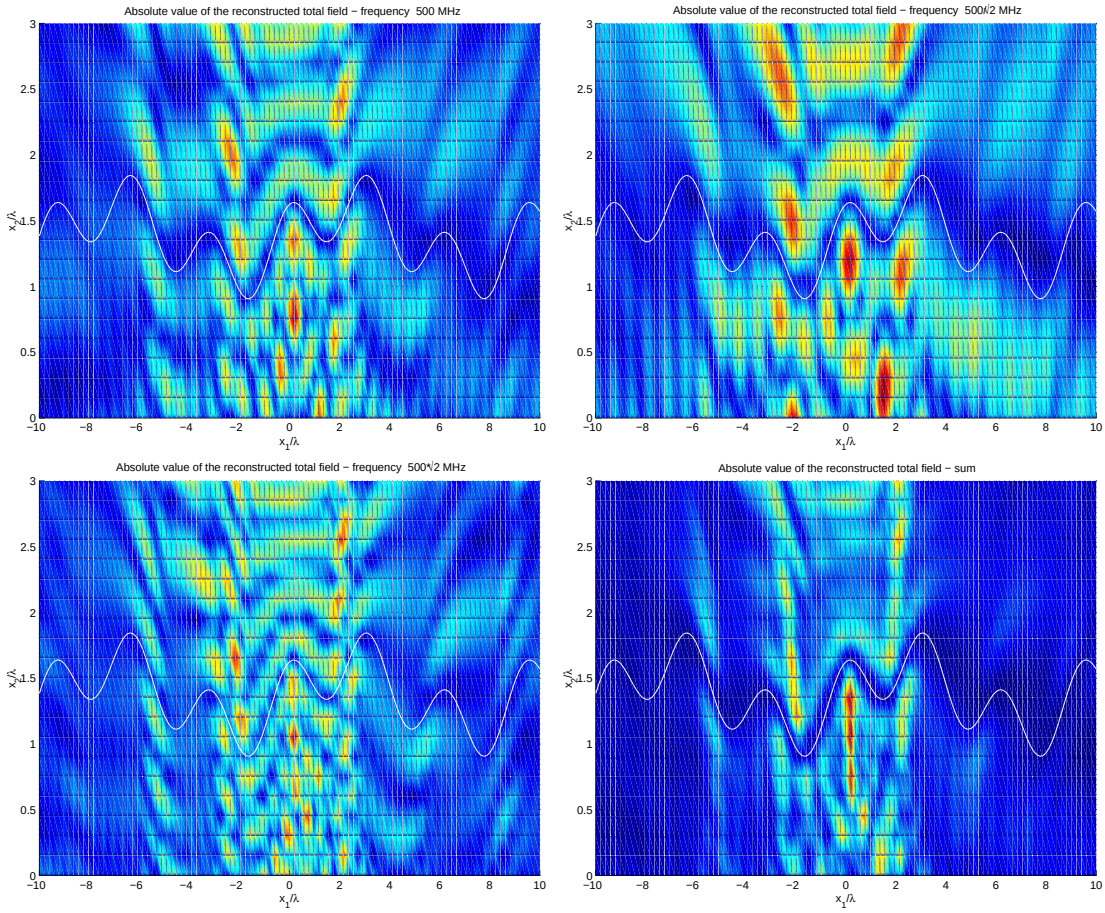

Figure 4.25: The absolute value of the reconstructed total field, $|G_k^\alpha(x,z)|$, for $k = 46.8\text{m}^{-1}$ (bottom left), $k = 33.1\text{m}^{-1}$ (top left) and $k = 23.4\text{m}^{-1}$ (top right) i.e. frequencies $500\sqrt{2}$MHz, 500MHz and $500/\sqrt{2}$MHz respectively, for surface (4.35). Also shown is $G_\Sigma(x,z)$ given by (4.37) (bottom right).

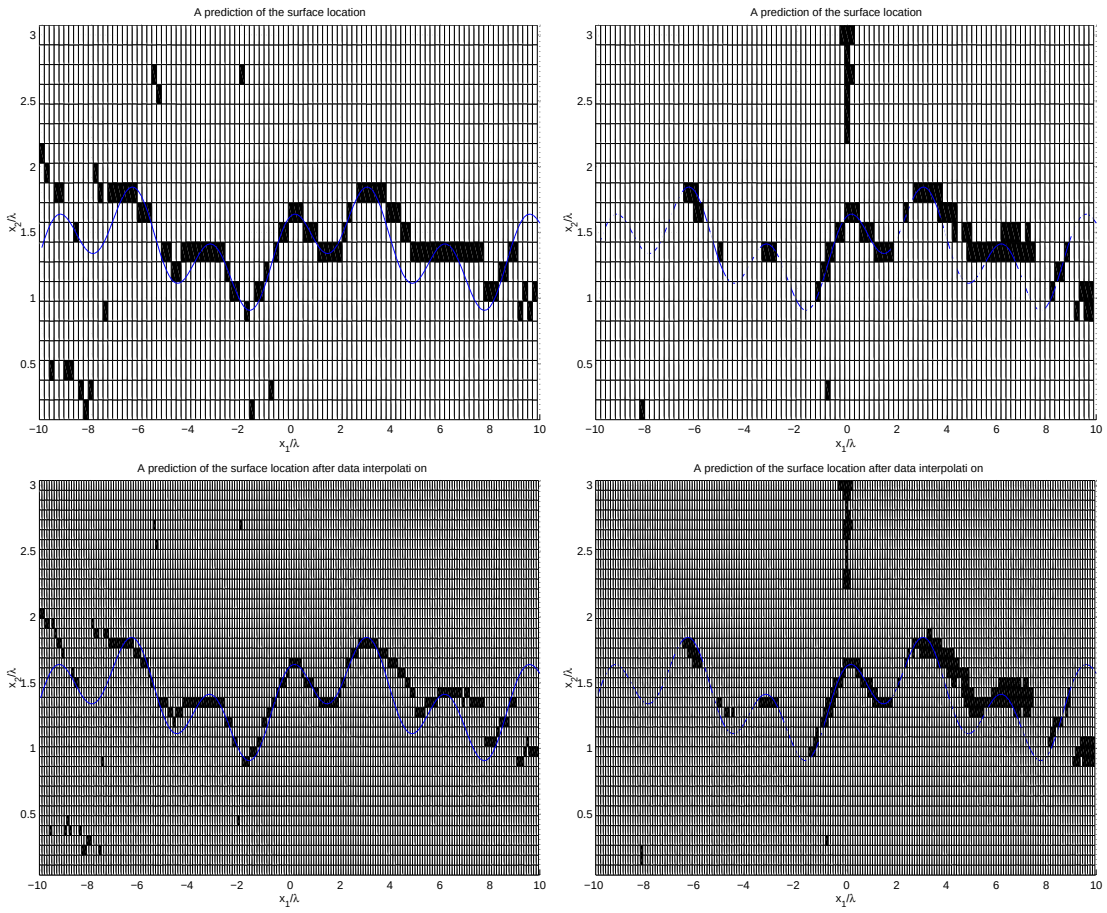

Figure 4.26: Shown are the predictions of the surface location for surface (4.35) using Method A with $\epsilon = 0.4$ (right hand side) and Method B (left hand side). The bottom plots interpolate $G_\Sigma(x, z)$ before invoking either method.

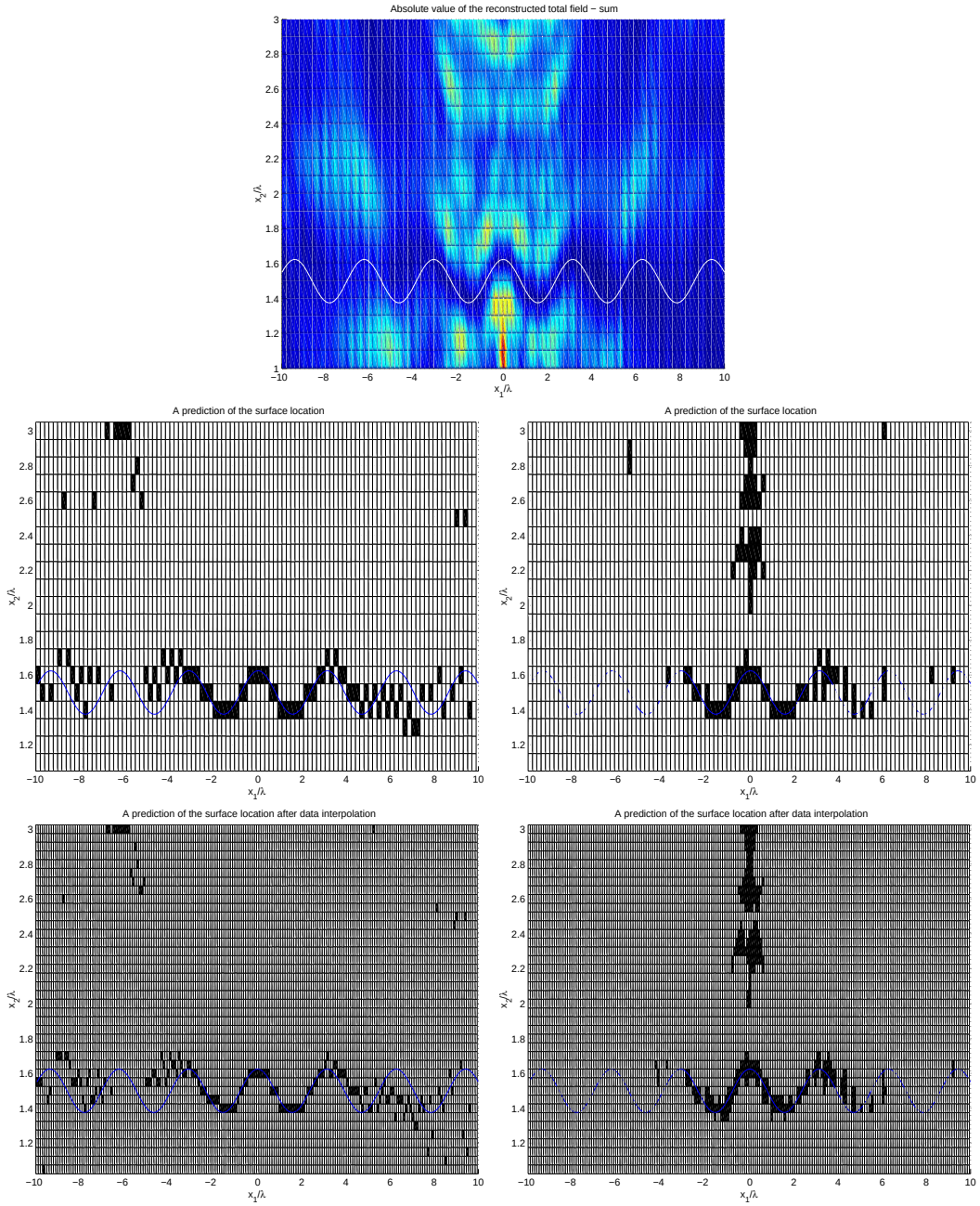

Figure 4.27: Weighted sum of squares of reconstructed total fields, $G_{\Sigma,\delta}(x,z)$, for frequencies $f = 500/\sqrt{2}$MHz, $f = 500$MHz and $f = 500\sqrt{2}$MHz, and surface (4.31) (top), with $\delta^* = 5$, i.e. 5% measurement error. Predictions of the surface location are made using Method A (right hand side) with $\epsilon = 0.57$ and using Method B (left hand side). The bottom plots interpolate $G_{\Sigma,\delta}(x,z)$ before invoking either method.

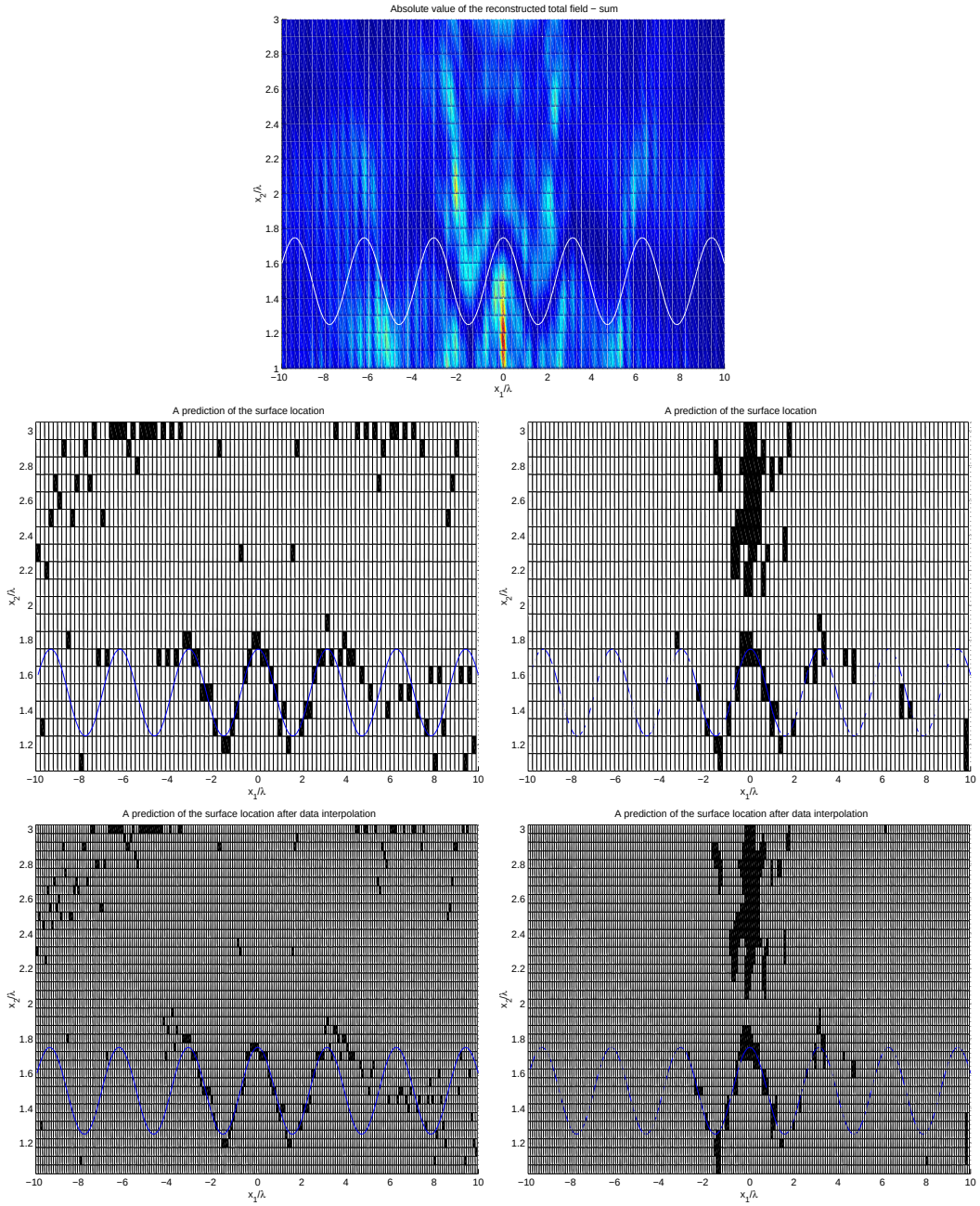

Figure 4.28: Weighted sum of squares of reconstructed total fields, $G_{\Sigma,\delta}(x,z)$, for frequencies $f = 500/\sqrt{2}$MHz, $f = 500$MHz and $f = 500\sqrt{2}$MHz, and surface (4.32) (top), with $\delta^* = 5$, i.e. 5% measurement error. Prediction of the surface location are made using Method A with $\epsilon = 0.75$ (right hand side) and using Method B (left hand side). The bottom plots interpolate $G_{\Sigma,\delta}(x,z)$ before invoking either method.

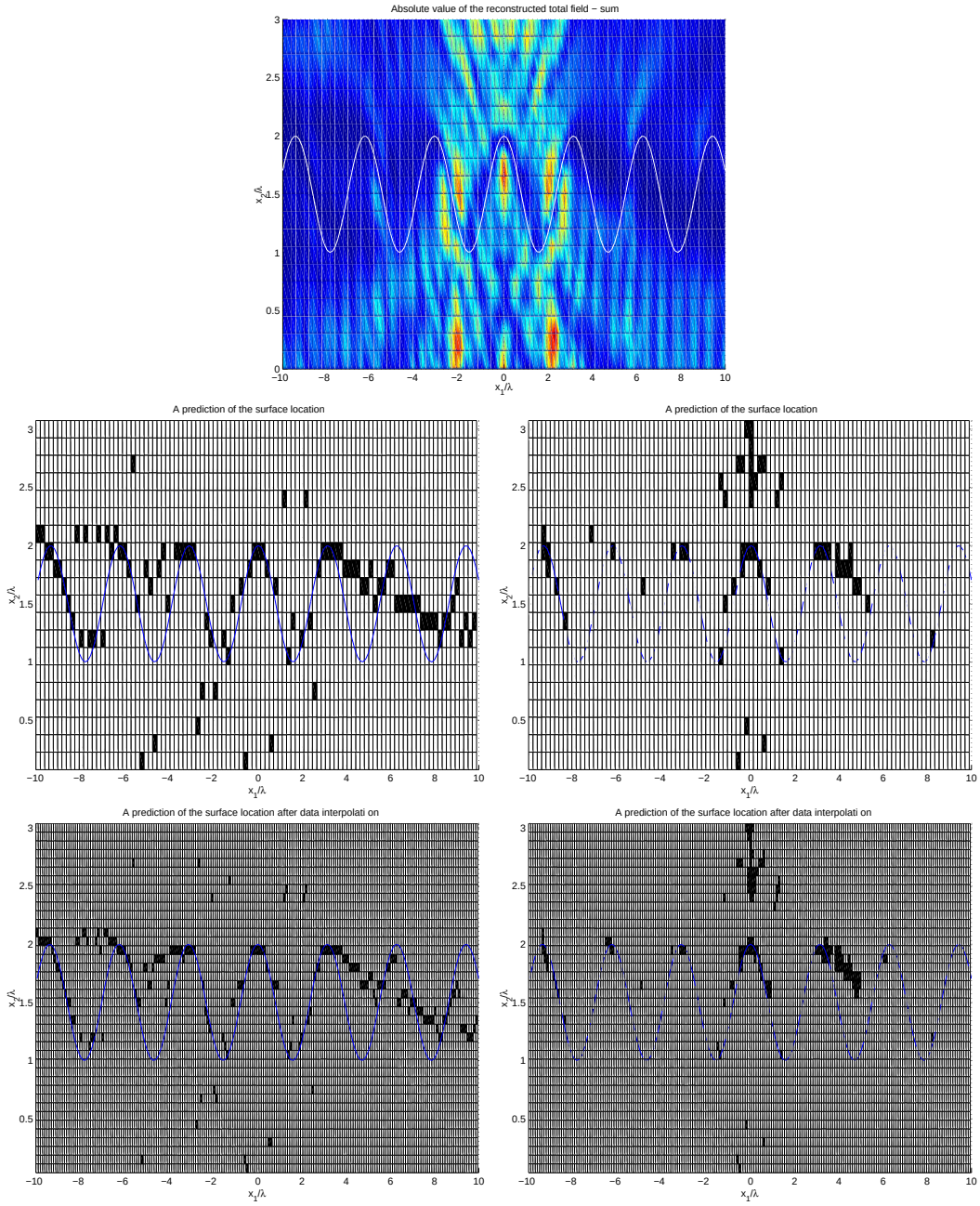

Figure 4.29: Weighted sum of squares of reconstructed total fields, $G_{\Sigma,\delta}(x,z)$, for frequencies $f = 500/\sqrt{2}$MHz, $f = 500$MHz and $f = 500\sqrt{2}$MHz, and surface (4.33) (top), with $\delta^* = 5$ i.e. 5% measurement error. Prediction of the surface location are made using Method A with $\epsilon = 0.4$ (right hand side) and using Method B (left hand side). The bottom plots interpolate $G_{\Sigma,\delta}(x,z)$ before invoking either method.

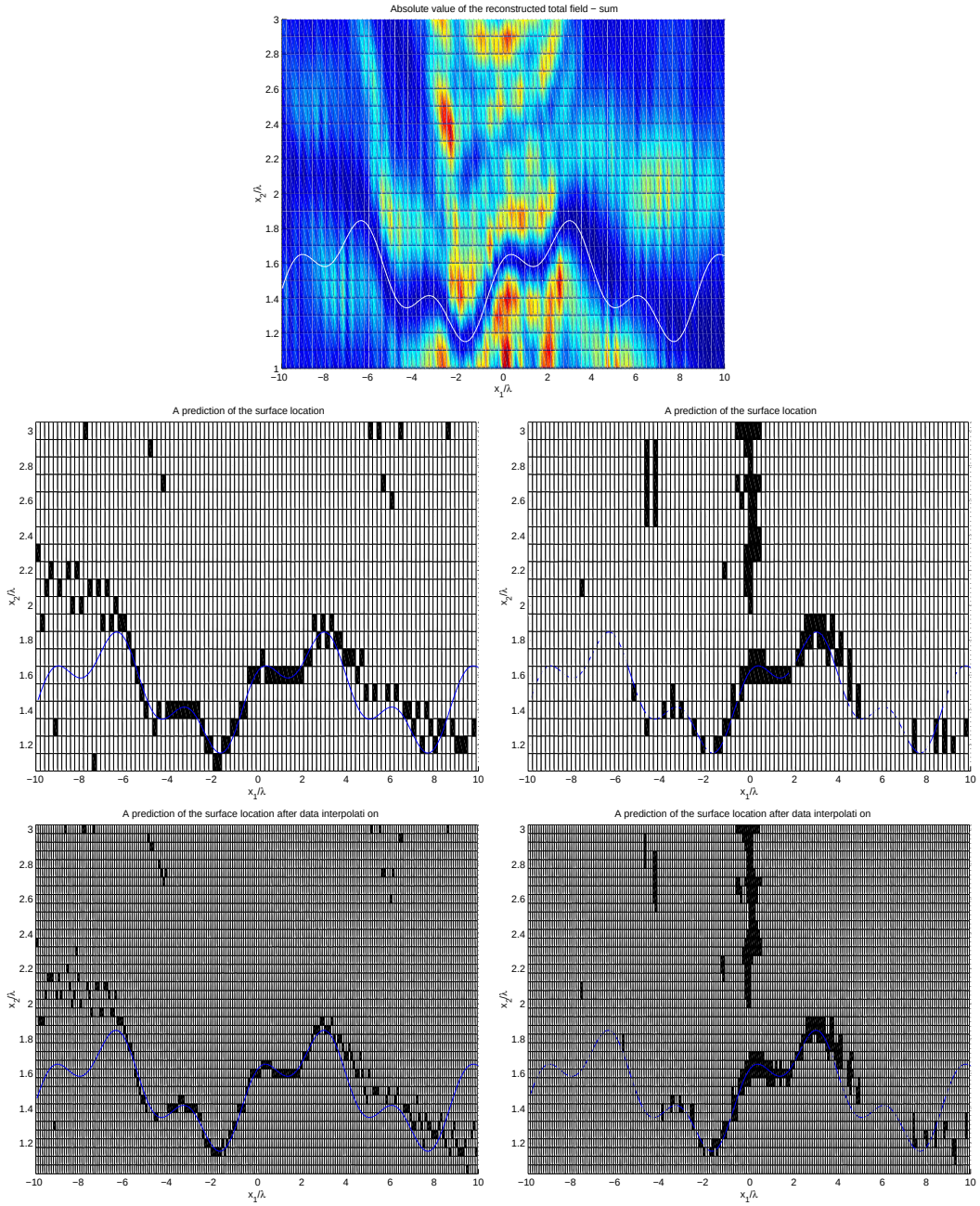

Figure 4.30: Weighted sum of squares of reconstructed total fields, $G_{\Sigma,\delta}(x,z)$, for frequencies $f = 500/\sqrt{2}$MHz, $f = 500$MHz and $f = 500\sqrt{2}$MHz, and surface (4.34) (top), with $\delta^* = 5$, i.e. 5% measurement error. Prediction of the surface location are made using Method A with $\epsilon = 0.6$ (right hand side) and using Method B (left hand side). The bottom plots interpolate $G_{\Sigma,\delta}(x,z)$ before invoking either method.

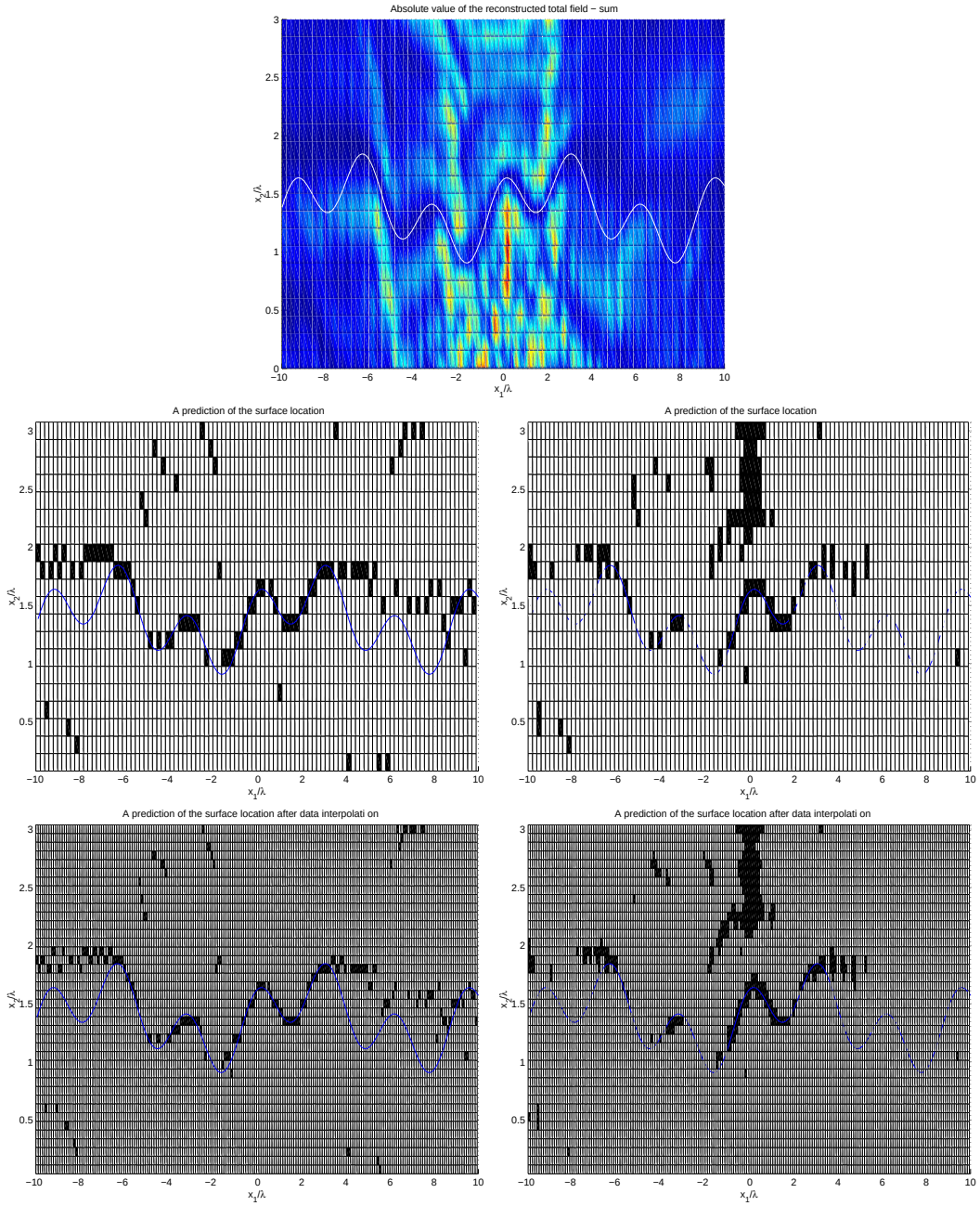

Figure 4.31: Weighted sum of squares of reconstructed total fields, $G_{\Sigma,\delta}(x,z)$, for frequencies $f = 500/\sqrt{2}$MHz, $f = 500$MHz and $f = 500\sqrt{2}$MHz, and surface (4.35) (top), with $\delta^* = 5$, i.e 5% measurement error. Prediction of the surface location are made using Method A with $\epsilon = 0.7$ (right hand side) and using Method B (left hand side). The bottom plots interpolate $G_{\Sigma,\delta}(x,z)$ before invoking either method.

Conclusions

By combining the information collected from three frequencies we have shown that the point source method gives us a good indication as to the location and shape of the surface that we are trying to detect. The results shown here are restricted to the geometry described above and as before show that the predictions of the surface location get worse as $|x_1|$ approaches the ends of the measurement line ie. as $|x_1| \to 10\lambda$. Again results have been shown for three sinusoidal surfaces increasing in amplitude from $\lambda/4$ to λ and two non-sinusoidal surfaces with amplitudes λ and λ. After interpolating the values of $G_\Sigma(x,z)$, from 5 points per wavelength (λ) to 10 points per wavelength (λ), the results improve. When 5% noise is added to the measurement, accuracy of the reconstructions worsen but in certain cases, especially the lower amplitude surfaces, the predictions remain good, especially for $|x_1| \leq 5$ and for Method A.

4.3.3 Effects of Noise Level

In this third set of numerical results we show the effect of the noise level when predicting the location of the surface. We compute $G_\delta^\alpha(x,z)$, defined by (4.26), with $G(y,z)$ replaced by the noisy data $G_\delta(y,z)$ as in section 4.3.1. We remind the reader that $G_\delta(x,z) = G(x,z) + N(x)$ where $N(x)$ and $N(y)$ are independently distributed for $x \neq y$ and where, for each x the real and imaginary parts of $N(x)$ are independently and identically normally distributed with mean 0 and standard deviation chosen such that $\sqrt{E(|N(x)|^2)} = \frac{\delta^*}{100}|\Phi(x,z)|$. For the frequency $f = 500$ MHz and for the surface (4.34), $G_\delta^\alpha(x,z)$ is computed on the two vertical lines, $x_1 = 0$ and $x_1 = 4\lambda$, for $\lambda < x_2 < 3\lambda$ (see Figure 4.32). For each vertical line we compute the value of x_2, denoted by X_2, which minimises $|G_\delta^\alpha(x,z)|$ over some range of x_2. The range of x_2 is either $\lambda < x_2 < 3\lambda$ or the part of this interval which lies within distance $\lambda/3$ of the surface, i.e. $\max(\lambda, f(x_1) - \frac{\lambda}{3}) < x_2 < \min(f(x_1) + \frac{\lambda}{3}, 3\lambda)$. X_2 is a point source

estimate of the surface height, $f(x_1)$. Using each of the ranges of x_2, X_2 is computed for 40 values of δ^*, logarithmically spaced on the interval $0.0001 < \delta^* < 12$. We choose $\alpha = 10^{-4}\delta^*/5$. Thus, as $\delta^* \to 0$, $\alpha \to 0$ and, by (4.36),

$$\frac{E(\delta^2)}{\alpha} \to 0$$

(monotonically) as $\delta^* \to 0$ and so, by (4.30),

$$E(|G_\delta^\alpha(x,z) - G(x,z)|^2) \to 0$$

for $x_2 > f(x_1)$. We compute the value of X_2 on the two vertical lines $x_1 = 0$ and $x_1 = 4\lambda$ twice, with two different realisations of the random noise, to give an indication of the variation from one realisation to another. In figures 4.33 and 4.34

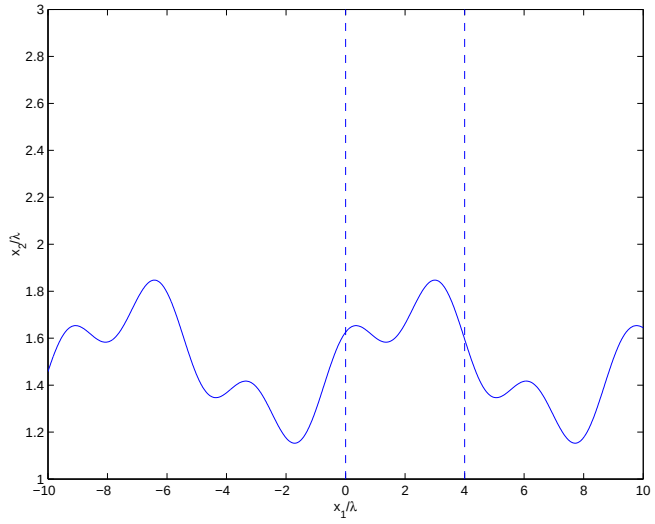

Figure 4.32: Graph to show the location of the two vertical lines on which $G_\delta^\alpha(x,z)$ is calculated.

we plot $|X_2 - f(x_1)|/\lambda$ against δ^*, i.e. we plot the distance of the predicted surface location from the actual surface (in wavelengths) as the noise in the measurement data increases. In Figure 4.33 $x_1 = 0$ so $f(x_1) = 1.625\lambda$. In Figure 4.34, $x_1 = 4\lambda$ so $f(x_1) = 1.591\lambda$. As expected, as the percentage of noise added to the measurement

data increases, the accuracy with which the prediction algorithm described above predicts the surface location worsens. In both sets of results, Figure 4.34 and Figure 4.33, the blue line indicates the distance of X_2 from $f(x_1)$ when x_2 minimises $|G^{\alpha}_{\delta}(x,z)|$ over the range $\lambda < x_2 < 3\lambda$. Also shown in each plot is a red line which shows the distance of X_2 from $f(x_1)$ when x_2 minimises $|G^{\alpha}_{\delta}(x,z)|$ over the range $f(x_1) - \lambda/3 < x_2 < f(x_1) + \lambda/3$. Comparing the results for $x_1 = 0$, Figure 4.33, and $x_1 = 4\lambda$, Figure 4.34, we can see that the accuracy with which the surface location is predicted is significantly better for $x_1 = 0$ than for $x_1 = 4\lambda$. The results for $x_1 = 0$ show that for small δ^* the surface location can be predicted to within $10^{-3}\lambda$ of the actual surface height but for $x_1 = 4\lambda$ this value reduces to $10^{-1.2}\lambda$. In each figure we plot, in green, $C(\delta^*)^{\frac{1}{2}}$, for some real valued constant, C, against δ^*. Comparing with this line we can observe that the accuracy with which the surface location is predicted converges at a rate of ${\delta^*}^{\frac{1}{2}}$ for $x_1 = 0$ but the convergence rate for $x_1 = 4\lambda$ is slower. These results are consistent with the results in Section 4.3.2 where it was observed that as x_1 approaches the end of the measurement line, i.e. 10λ, the prediction of the surface location worsens. We observe in figures 4.33 and 4.34 that when $\delta^* > 2$, for $x_1 = 0$, and $\delta^* > 1$, for $x_1 = 4\lambda$, the prediction of the surface location is improved when the interval of x_2 over which $|G^{\alpha}_{\delta}(x,z)|$ is minimised is restricted to $f(x_1) \pm \lambda/3$. This result is consistent with the observations in Section 4.3.1 where it was pointed out that while $|G^{\alpha}_{\delta}(x,z)|$ has a minimum at $x_2 = f(x_1)$ it is also minimised approximately at the points $x_2 = f(x_1) + c\lambda/2$, for small integer values of c.

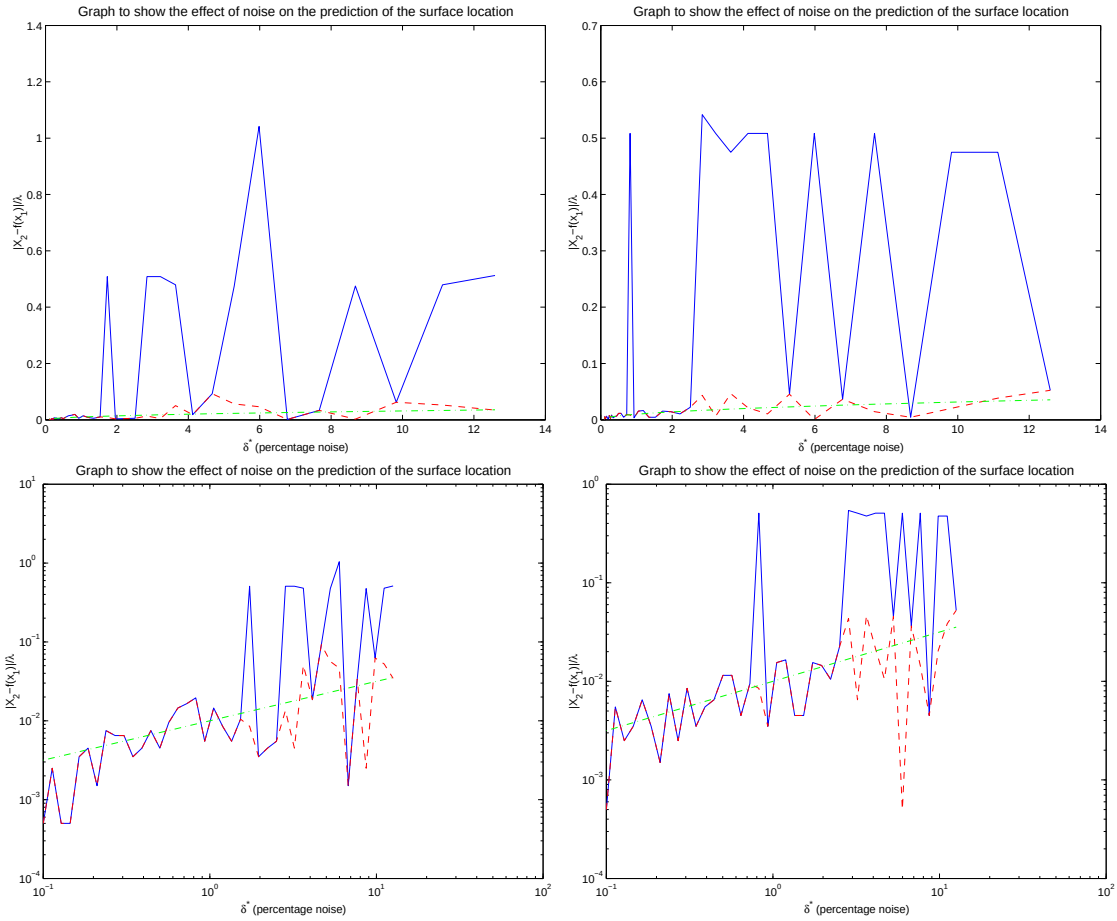

Figure 4.33: Results showing the accuracy of the predicted surface location (X_2) as δ^* increases. Shown are results for $f = 500$ MHz and the rough surface (4.34) when $G^{\alpha}_{\delta}(x, z)$ is calculated on the vertical line $x_1 = 0$. As discussed in the main text X_2 is computed twice for each value of δ^*, using different realisations of the random noise. The first set of results are shown on the left hand side and the second on the right hand side. The top plots indicate in wavelengths the distance of X_2 from the surface height, $f(x_1)$, and the bottom plots show the same data on a logarithmic scale. The blue line shows the distance of X_2 from $f(x_1)$ when X_2 is the value of x_2 which minimises $|G^{\alpha}_{\delta}(x, z)|$ over the range $\lambda < x_2 < 3\lambda$ and the red line shows the distance of X_2 from $f(x_1)$ when X_2 is the value of x_2 which minimises $|G^{\alpha}_{\delta}(x, z)|$ over the range $f(x_1) - \lambda/3 < x_2 < f(x_1) + \lambda/3$.

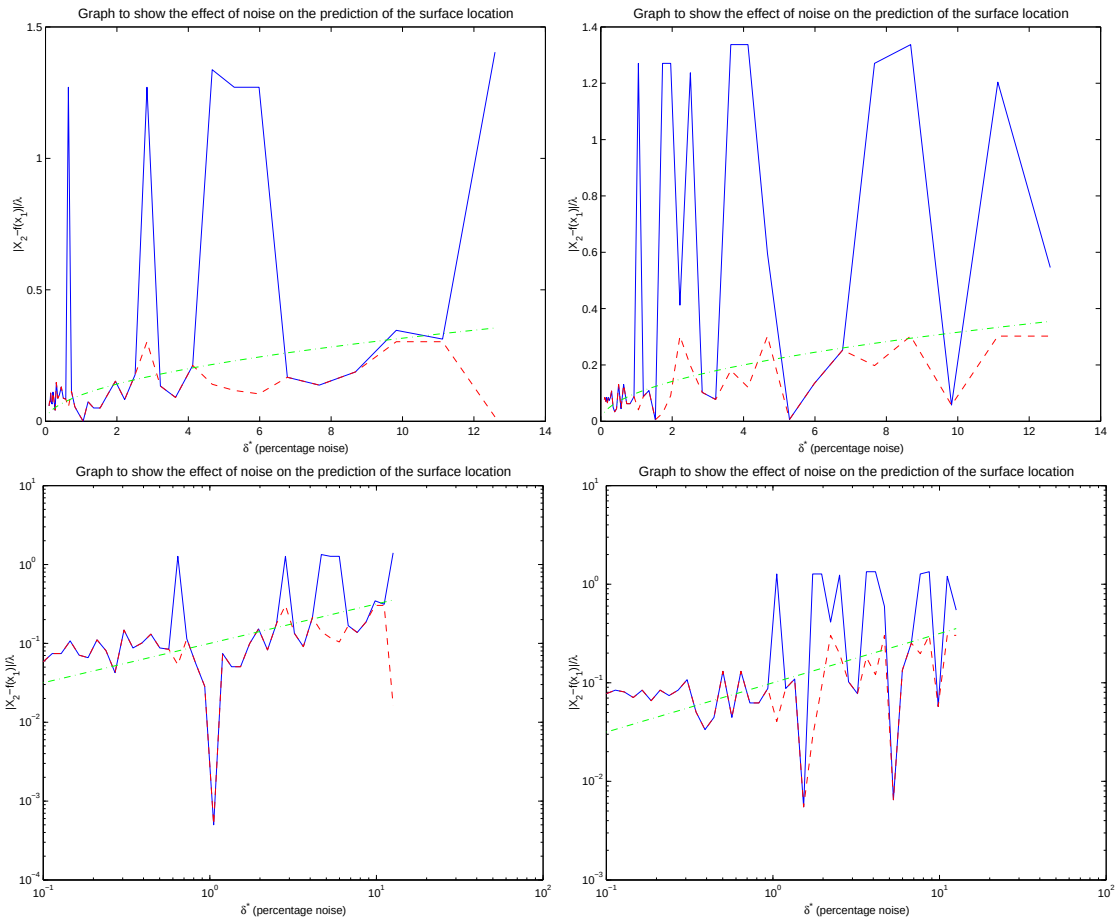

Figure 4.34: Results showing the accuracy of the predicted surface location (X_2) as δ^* increases. Shown are results for $f = 500$ MHz and the rough surface (4.34) when $G^{\alpha}_{\delta}(x, z)$ is calculated on the vertical line $x_1 = 4\lambda$. As discussed in the main text X_2 is computed twice for each value of δ^*, using different realisations of the random noise. The first set of results are shown on the left hand side and the second on the right hand side. The top two plots indicate in wavelengths the distance of X_2 from the surface height, $f(x_1)$, and the bottom two plots show the same data on a logarithmic scale. The blue line shows the distance of X_2 from $f(x_1)$ when X_2 is the value of x_2 which minimises $|G^{\alpha}_{\delta}(x, z)|$ over the range $\lambda < x_2 < 3\lambda$ and the red line shows the distance of X_2 from $f(x_1)$ when X_2 is the value of x_2 which minimises $|G^{\alpha}_{\delta}(x, z)|$ over the range $f(x_1) - \lambda/3 < x_2 < f(x_1) + \lambda/3$.

Chapter 5

The Point Source Method in the Time Domain

5.1 Direct and Inverse Problems in the Time Domain

In Chapter 3 we have discussed the problem of scattering of an incident field by a rough surface when the point source which gives rise to the incident field is time harmonic. In this chapter we consider the case when the point source emits a pulse. In particular we will have in mind inverse rough surface scattering problems with geometry and incident pulses similar to those arising in ground penetrating radar (GPR) applications.

GPR techniques have become more popular over the last few years in areas such as rescue archaeology, site conservation and non-invasive methods for subsurface exploration [23]. GPR information is acquired by reflecting radar waves off subsurface features. The radar waves are propagated in distinct pulses from a surface antenna, reflected off buried objects or features and detected back at the surface by a receiving antenna. (See Figure 5.1 for an example of GPR antennas.) As the radar pulses are transmitted through the ground their velocity depends upon the electrical and magnetic properties of the material through which they are travelling. For materials whose magnetic permeability is equal to that in vacuo, the velocity of the radar wave as it passes through a material is given by

$$c = \frac{c_0}{\sqrt{\epsilon/\epsilon_0}}$$

where c_0 is the speed of light in vacuo, ϵ_0 is the dielectric permittivity in vacuo and ϵ is the dielectric permittivity of the material [23]. From time of travel information the distance or depth of a feature can be calculated. General GPR systems use dipolar antennas ranging from 10 MHz to 1000 MHz. Most of the antenna energy is concentrated around this one central frequency, but radar energy is produced in an interval that ranges up to one octave above and below the centre frequency.

For $F \in L^1(\mathbb{R})$ let $\hat{F} \in BC(\mathbb{R})$ denote the Fourier Transform of F, defined by

$$\hat{F}(\omega) = \frac{1}{2\pi} \int_{-\infty}^{\infty} F(t) e^{i\omega t} \mathrm{d}t, \qquad \omega \in \mathbb{R}.$$

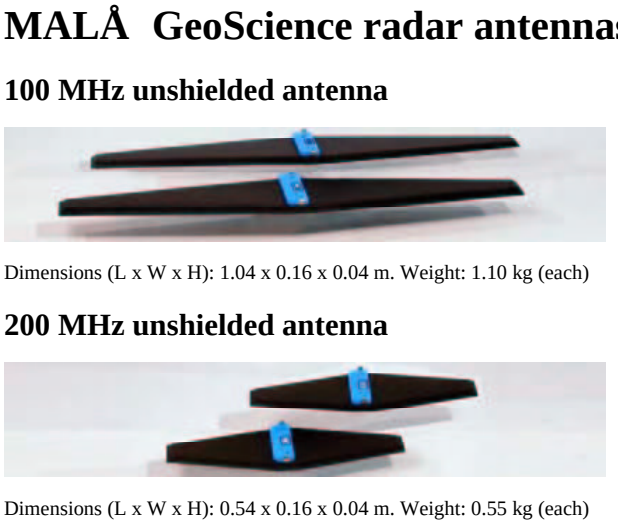

Figure 5.1: Examples of Ground Penetrating Radar antennas

If F is sufficiently smooth (e.g. if $F \in C^2(\mathbb{R}) \cap L^1(\mathbb{R})$) then $\hat{F} \in L^1(\mathbb{R})$ and F is given in terms of $\hat{F}$ by the inverse Fourier transform formula

$$F(t) = \int_{-\infty}^{\infty} F(\omega) e^{-i\omega t} \mathrm{d}\omega, \qquad t \in \mathbb{R}.$$

To model the pulse from a GPR antenna we assume that the incident field takes the form

$$U^i(x,t) = \int_{-\infty}^{\infty} \frac{\Phi_{\omega/c}(x,z)}{\Phi_{\omega/c}(x_0,z)} \hat{F}^i(\omega) e^{-i\omega t} \mathrm{d}\omega, \tag{5.1}$$

for some real-valued $F^i \in C^2(\mathbb{R})$ which is compactly supported, where z is the source position, $x_0 \neq z$ is some reference point where the incident field is measured and, for $x, y \in \mathbb{R}^2$, $x \neq y$,

$$\Phi_k(x,y) := \frac{i}{4} H_0^{(1)}(k|x-y|), \qquad k > 0,$$

while

$$\Phi_k(x,y) := \overline{\Phi_{-k}(x,y)}, \qquad k < 0.$$

It follows from (5.1) that, if $|x-z| = R := |x_0 - z|$, then

$$U^i(x,t) = \int_{-\infty}^{\infty} \hat{F}^i(\omega) e^{-i\omega t} \mathrm{d}\omega = F^i(t),$$

so that $F^i(t)$ is the incident field at time t at distance R from the source (and in particular is the incident field at x_0).

The direct problem we consider in this chapter is as follows: Given $F^i \in C^2(\mathbb{R})$ which is compactly supported, find $U^s \in C^2(D \times \mathbb{R}) \cap C(\overline{D} \times \mathbb{R})$ such that

$$\begin{aligned} \Delta U^s &= \frac{1}{c^2} \frac{\partial^2 U^s}{\partial t^2} \qquad \text{in } D \times \mathbb{R}, \\ U^s &= -U^i \qquad \text{in } \Gamma \times \mathbb{R} \end{aligned}$$

and, for some $t_0 \in \mathbb{R}$, $U^s(\cdot, t) = 0$ for $t < t_0$. By inspection, the solution to this direct problem (at least formally) is that the total field is given as

$$U(x,t) = U^i(x,t) + U^s(x,t) = \int_{-\infty}^{\infty} \frac{G_{\omega/c}(x,z)}{\Phi_{\omega/c}(x_0,z)} \hat{F}^i(\omega) e^{-i\omega t} \mathrm{d}\omega, \tag{5.2}$$

where, for $k > 0$, $G_k(x,z)e^{-i\omega t}$ denotes the total field corresponding to the time harmonic incident field $\Phi_k(x,z)e^{-i\omega t}$, so that $G_k(\cdot,z)$ is the solution to **BVP1** in Chapter 3 and, for $k < 0$, $G_k(\cdot,z) := \overline{G_{-k}(\cdot,z)}$.

Figure 5.2 shows an actual incident pulse signature, $F^i(t)$, for a 500MHz GPR antenna, and the corresponding power spectrum, and Figure 5.3 a proposed idealisation, both taken from [23]. A good approximation to such an idealised pulse is given by defining

$$F^i(t) = -e^{-\sigma(t+\frac{\epsilon}{\sqrt{\sigma}})^2} + 2e^{-\sigma t^2} - e^{-\sigma(t-\frac{\epsilon}{\sqrt{\sigma}})^2}, \qquad t \in \mathbb{R}, \tag{5.3}$$

with $\sigma = 25\omega_0^2/98$, $\omega_0 = 2\pi f$, f the nominal frequency, and $\epsilon = 0.1$. The Fourier transform of F^i, given by (5.3), is

$$\hat{F}^i(\omega) = -\sqrt{\frac{2\pi}{3\sigma}} e^{-\omega^2/4\sigma} \Big(\cos\Big(\frac{\omega\epsilon}{\sqrt{\sigma}}\Big) - 1 \Big) \tag{5.4}$$

so that

$$|\hat{F}^i(\omega)|^2 = \frac{2\pi}{3\sigma} e^{-\omega^2/2\sigma} \Big(\cos\Big(\frac{\omega\epsilon}{\sqrt{\sigma}}\Big) - 1 \Big)^2. \tag{5.5}$$

In Figures 5.4 and 5.5 we plot $F^i(t)$ and $|\hat{F}^i(\omega)|^2$, given by (5.4) and (5.5) respectively, for nominal frequency $f = 500$MHz.

To compute an approximation to $U^s(x,t)$ we proceed by first approximating $F^i(t)$ by a periodic function, $F^i_T(t)$, of some sufficiently large period T, defined by

$$F^i_T(t) = F^i(t), \qquad -T < t \leq T.$$

Sampling $F^i_T(t) = F^i_T(t+T)$ over a period T at intervals $\Delta = \frac{T}{N}$ for some $N \in \mathbb{N}$,

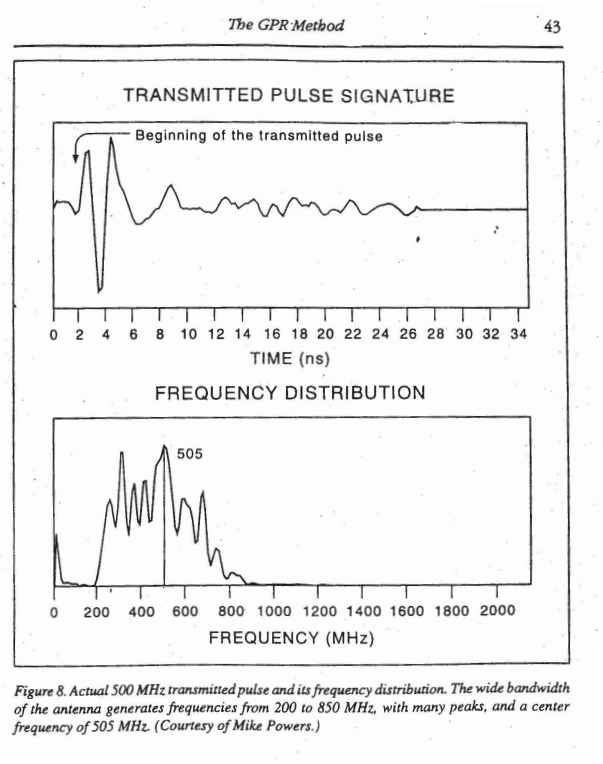

Figure 5.2: Actual pulse signature and frequency distribution for a GPR antenna with nominal frequency 500MHz (taken from [23]).

with T_1 the start time, define

$$F^i_p := F^i_T(T_1 + \Delta p), \qquad p \in \mathbb{Z}. \tag{5.6}$$

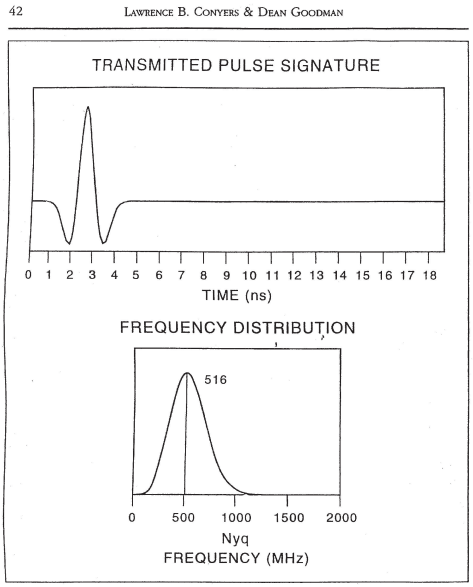

Figure 7. Idealized wave of a transmitted radar pulse and the frequency distribution of a 500 MHz antenna. The upper figure is the idealized pulse as it is transmitted into the ground over time. The lower figure is the calculated frequency distribution of that pulse, with a calculated center frequency of 516 MHz. (Modified from Powers and Olhoeft 1995.)

Figure 5.3: Idealised transmitted pulse signature and frequency distribution for a GPR antenna with nominal frequency 500MHz (taken from [23]).

Then, using the standard discrete Fourier transform formula [42],

$$F_p^i = \sum_{j=0}^{N-1} X_j e^{-2\pi ijp/N}, \qquad p = 0, 1 \ldots, N-1,$$

where

$$X_j := \frac{1}{N} \sum_{p=0}^{N-1} F_p^i e^{2\pi ijp/N}, \qquad j \in \mathbb{Z}.$$

Now since $F_T^i(t) = F_T^i(t+T)$ is periodic with period T, $F_{p+N}^i = F_p^i$ for $p \in \mathbb{Z}$. Hence, $X_{j+N} = X_j$, $j \in \mathbb{Z}$. Moreover, for N odd, which we assume to be the case for the rest of the chapter,

$$X_j = \frac{1}{N} \sum_{p=-(N-1)/2}^{(N-1)/2} F_p^i e^{2\pi ijp/N}, \qquad j \in \mathbb{Z}. \tag{5.7}$$

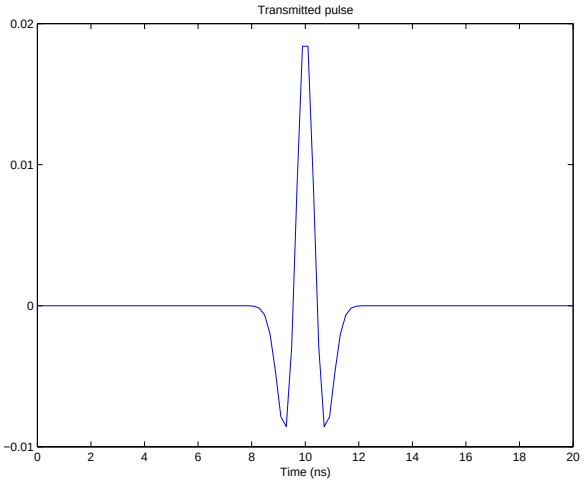

Figure 5.4: Incident pulse signature, $F^i(t)$, for nominal frequency $f = 500$MHz, given by (5.4)

.

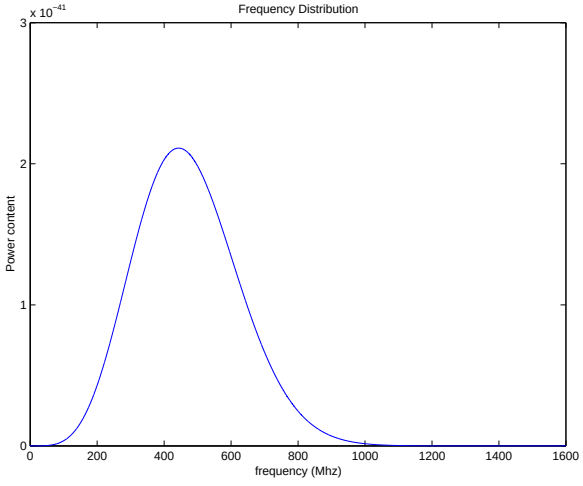

Figure 5.5: Power spectrum, $|\hat{F}^i(\omega)|^2$, for nominal frequency $f = 500$MHz, given by (5.5)

.

From this representation it becomes clear, since F^i is real-valued, that

$$\overline{X}_j = X_{-j}, \qquad j \in \mathbb{Z}.$$

Since $X_{j+N} = X_j$, $j \in \mathbb{Z}$, it follows that

$$F_p^i = \sum_{j=-(N-1)/2}^{(N-1)/2} X_j e^{-2i\pi j \Delta p/T}, \qquad p \in \mathbb{Z}.$$

Let

$$F_N^i(t) := \sum_{j=-(N-1)/2}^{(N-1)/2} X_j e^{-2i\pi j (t-T_1)/T}, \qquad t \in \mathbb{R}. \tag{5.8}$$

Then $F_N^i(t+T) = F_N^i(t)$, $t \in \mathbb{R}$, and

$$F_N^i(T_1 + \Delta p) = F_p^i = F_T^i(T_1 + \Delta p), \qquad p \in \mathbb{Z},$$

so that F_N^i interpolates F_T^i at $T_1 + \Delta p$, $p \in \mathbb{Z}$. It is easy to see that $F_N^i(t)$ can be rewritten in the form

$$F_N^i(t) = \frac{\alpha_0}{2} + \sum_{k=1}^{(N-1)/2} \Big[\alpha_k \cos \frac{2\pi j (t-T_1)}{T} + \beta_k \sin \frac{2\pi j (t-T_1)}{T}\Big],$$

with real coefficients $\alpha_j = 2\Re X_j$ and $\beta_j = 2\Im X_j$. In fact [34], there exists a unique function of this form (a so-called trigonometric polynomial of degree $(N-1)/2$ and period T) which interpolates $F_T^i(t)$ at $T_1 + \Delta p$, $p \in \mathbb{Z}$, and, if $F_T^i \in C^n(\mathbb{R})$, for some $n \in \mathbb{N}$, there holds the error estimate [34, Theorem 11.6]

$$\|F_N^i - F_T^i\|_\infty \le c \frac{\ln N}{N^n},$$

for some constant $c > 0$. We note that $F_T^i \in C^n(\mathbb{R})$ if $F^i \in C^n(\mathbb{R})$ and T is large enough so that $(-T/2, T/2)$ contains the support of F^i.

With F_N^i given by (5.8) it holds that

$$\hat{F}_N^i(\omega) = \sum_{j=-(N-1)/2}^{(N-1)/2} X_j e^{i\omega_j T_1} \delta(\omega - \omega_j),$$

where $\omega_j = 2\pi j/T$ and δ is the Dirac delta. We suppose that $X_0 = 0$ (the incident pulse has no DC component) which is the case for F^i given by (5.3). Then, from

(5.1), an approximation to $U^i(x,t)$ is

$$U_N^i(x,t) := \sum_{\substack{j=-(N-1)/2 \\ j\neq 0}}^{(N-1)/2} A_j \Phi_{k_j}(x,z) e^{-i\omega_j t},$$

where $k_j := \omega_j/c$ and

$$A_j := \frac{X_j e^{2i\pi j T_1/T}}{\Phi_{k_j}(x_0,z)}.$$

Since $\overline{A}_j = A_j$, we have that

$$U_N^i(x,t) = 2\Re \sum_{j=1}^{(N-1)/2} A_j \Phi_{k_j}(x,z) e^{-i\omega_j t}.$$

Similarly, from (5.2), an approximation to the total field is

$$U_N(x,t) := 2\Re \sum_{j=1}^{(N-1)/2} A_j G_{k_j}(x,z) e^{-i\omega_j t}. \tag{5.9}$$

For the direct scattering problem we are considering in this chapter the inverse problem analogous to that of Chapter 4 is the following one. Let γ^* denote the finite horizontal line given by (4.1) as in Chapter 4.

The Time Domain Inverse Problem. *Given the source position $z \in D\backslash\gamma^*$, the incident field, $F^i(t)$, for $t \in \mathbb{R}$, at a reference point $x_0 \neq z$, and measurements of the total field $U(x,t)$, for $x \in \gamma^*$ and $t \in \mathbb{R}$, determine f, i.e. the location of the infinite rough surface Γ.*

The obvious analogue of the point source method of Chapter 4 is as follows. As a first step, compute, given $U(x,t)$, for $x \in \gamma^*$, $t \in \mathbb{R}$, an approximation to $U(x,t)$ for $x \in D$, $t \in \mathbb{R}$. As a second step determine Γ as the curve on which the approximation to $U(x,t)$ is minimised.

To construct an approximation to $U(x,t)$ for $x \in D$, $t \in \mathbb{R}$, we propose, as a first stage, to approximate F^i by F_N^i, given by (5.8). Then the total field is given approximately by (5.9). As a second stage we propose to, similarly, approximate

the measured data by $\tilde{U}_N(x,t)$, for $x \in \gamma^*$, $t \in \mathbb{R}$, where $\tilde{U}_N(x,t)$ is the T-periodic trigonometric polynomial of degree $\leq (N-1)/2$ which interpolates $U(x,\cdot)$ at $T_1+\Delta p$, $p = 0, 1, \ldots, N-1$. This approximation takes the form

$$\tilde{U}_N(x,t) = 2\Re \sum_{j=1}^{(N-1)/2} a_j(x) e^{-i\omega_j t}, \tag{5.10}$$

for some functions $a_j(x)$, determined by the interpolation requirement. Comparing (5.9) with (5.10) we obtain, approximately, values for $G_{k_j}(x,z)$ for $j = 1, \ldots, (N-1)/2$ and $x \in \gamma^*$, namely $G_{k_j}(x,z) = a_j(x)/A_j$. Given these values we can compute the Point Source Method approximations $G^\alpha_{k_j}(x,z)$, given by (4.26). Then, as the third and final stage, we can approximate the total field by (5.9) with $G_{k_j}(x,z)$ replaced by $G^\alpha_{k_j}(x,z)$, giving the approximation

$$U^\alpha_N(x,t) := 2\Re \sum_{j=1}^{(N-1)/2} A_j G^\alpha_{k_j}(x,z) e^{-i\omega_j t}, \qquad x \in \mathbb{R}^2 \backslash (\gamma^* \cup \{z\}), t \in \mathbb{R}. \tag{5.11}$$

We propose to locate the surface Γ as the minimum of

$$P(x) = \frac{1}{T} \int_0^T \left(U^\alpha_N(x,t) \right)^2 \mathrm{d}t. \tag{5.12}$$

By Parseval's theorem,

$$P(x) = 2 \sum_{j=1}^{(N-1)/2} |A_j|^2 |G^\alpha_{k_j}(x,z)|^2. \tag{5.13}$$

5.2 Numerical Results

5.2.1 Reconstructions of the total field

Throughout the remainder of the chapter we assume a wave speed $c = c_0/\sqrt{10}$, where c_0 is the velocity of light in vacuo. This wave speed is appropriate for GPR waves in dry sandy coastal land [23], and gives a wavelength of $\lambda = c/f = 0.19$m when the frequency is $f = 500$MHz. In the remainder of the chapter we also assume that F^i

is given by (5.3) with $f = 500$MHz, so that the incident pulse is that appropriate to a GPR antenna with nominal frequency 500MHz. For the first set of numerical experiments, we calculate $U_N^\alpha(x^*, t)$ for $N = 49$, using (5.11), for $0 < t \leq T$ where $T = 20ns$ and for $|x_1^*| \leq 5\lambda$ and $\lambda/2 \leq x_2^* \leq 3\lambda/2$. $G_{k_p}^\alpha(x^*, z)$ is calculated using the Point Source Method described in Chapter 4, for x^* at 9.6 points per wavelength (λ) in both directions, where $k_p = 2\pi f_p/c$, for $p = 1 \ldots 24$, with $f_p = 50p$MHz. As in section 4.3, for each $x^* = (x_1^*, x_2^*) \in \mathbf{R}^2$, we make the choice $\Gamma_{x^*} = \{(x_1, f_{x^*}(x_1))|x_1 \in \mathbb{R}\}$, with $f_{x^*}(x) = -\frac{3\lambda}{4}e^{-(\frac{x_1 - x_1^*}{8\lambda})^2} + \frac{\lambda}{4} + x_2^*$. The measurement line in the inverse problem is $\gamma^* = \{(x_1, H)|\, |x_1| \leq 10\lambda = 1.9\text{m}\}$ and we fix the height of the measurement line as $H = 4\lambda = 0.76$m, $z = (0, 4\lambda) = (0, 0.76)$m and $\alpha = 10^{-4}$. Other details of the calculation of $G_k^\alpha(x^*, z)$ are as in Chapter 4. In the numerical experiments in this chapter we use only two surfaces, a sinusoidal surface described by

$$f(x_1) = \lambda + \frac{\lambda}{4}\cos(\frac{2x_1}{\lambda}), x_1 \in \mathbf{R}, \tag{5.14}$$

and a rough surface described by

$$f(x_1) = \frac{11\lambda}{8} + \frac{\lambda}{8}\cos(\frac{2x_1}{\lambda}) + \frac{\lambda}{4}\sin(\frac{2x_1}{3\lambda}), x_1 \in \mathbf{R}. \tag{5.15}$$

To compute the noisy reconstructed total field we use the same method as in section 4.3; hence we calculate $U_{N,\delta}^\alpha(x, t)$ as for $U_N^\alpha(x, t)$ but with noise added to each measured value of $G_{k_p}(x, z)$, $x \in \gamma^*$, by replacing $G_{k_p}(x, z)$ by $G_{k_p,\delta}(x, z) = G_{k_p}(x, z) + N(x)$, where the real and imaginary parts of $N(x)$ and $N(y)$ are independently distributed for $x \neq y$, and where for each x, the real and imaginary parts of $N(x)$ are independently and identically normally distributed with mean 0 and standard deviation chosen such that $\sqrt{E(|N(x)|^2)} = \frac{\delta^*}{100}|\Phi_{k_p}(x, z)|$, where δ^* is the specified percentage error. Note that the "measured" values of $G_{k_p}(x, z)$ are computed by the boundary integral equation method and super-algebraically convergent Nyström method proposed in [41], with horizontal spacing between quadrature points of $\lambda/10$, and truncating the boundary integral so that Γ is replaced by $\{x \in \Gamma||x_1| \leq 100\lambda\}$ (see [40] for further details).

In figures 5.7 and 5.9 we compare the reconstructed total field $U_N^\alpha(x,t)$, for $0 \leq t \leq T$, where $T = 20$ns, with $U_N(x,t)$ given by (5.9). In figures 5.11 and 5.13 we compare the noisy reconstructed total field $U_{N,\delta}^\alpha(x,t)$, for $\delta^* = 5$, with $U_N(x,t)$. In the four figures 5.7, 5.9, 5.11 and 5.13 the incident and reflected pulse can be seen in the top two plots (the reflected pulse with phase change of 180°, appropriate to the boundary condition that the total field vanishes). Figures 5.6, 5.8, 5.10 and 5.12 show snapshots of $U_N^\alpha(x,t)$ at a sequence of times for the same geometry and noise levels as figures 5.7, 5.9, 5.11 and 5.13, respectively. In figures 5.7 and 5.11 the incident and reflected pulses begin to merge in the 3rd plot, $x = (0, 1.5\lambda)$. This point is close to the surface which passes through $(0, 1.25\lambda)$. In figures 5.9 and 5.13 the incident and reflected pulses also begin to merge in the 3rd plot, for $x = (0, 1.6\lambda)$ (the surface passes through $(0, 1.5\lambda)$. The reconstructed total fields agree very accurately with the exact values of the total field. When noise is added to the data, even though we can see errors in the reconstructed total fields, the incident and reflected pulses are clearly visible and correctly positioned on the time axis. Although these reconstructions are for the case when the total electric field vanishes on the surface, the same formula for reconstructing the total field from measured data can be expected to work regardless of the boundary condition. There would appear, in fact, to be good prospects for locating the surface, even without knowledge of the boundary condition, as the locus of those points where the incident and reflected pulses coincide in time.

5.2.2 Solving the Inverse Problem

We predict the surface location as the minimum of $P(x)$, given by (5.12) and (5.13) using the second method used in section 4.3. Hence in each column we colour in black the square in which $P(x)$ is minimised as a function of x_2. In figures 5.14 to 5.17 we first interpolate $|U_N^\alpha(x,t)|$, calculated for $|x_1| \leq 5\lambda$ and $1/2\lambda \leq x_2 \leq 3/2\lambda$ at 9.6 points per wavelength (λ), to 19 points per wavelength. On the right hand side of each of these figures we predict the location of the surface by colouring in black the

square in which $P(x)$ is minimised as a function of x_2.

5.2.3 Conclusions

In this chapter we have shown that we can generalise the Point Source Method, described in Chapter 4, to reconstruct the total electric field when the incident wave is not necessarily time harmonic. In particular we have chosen an incident pulse that is similar to that arising in ground penetrating radar (GPR) applications. The reconstructed total fields agree very well with the exact total field, and when 5% noise is added to the measurements the incident and reflected pulse positions in time are very accurate and clearly observable. Although we assume that the total field vanishes on the boundary we expect to be able to locate the surface with any boundary condition, predicting the surface location to be the locus of those points where the incident and reflected pulses merge. In figures 5.14 to 5.17 we plot the power content of the electric field, for $P(x)$ given by (5.12) and (5.13). On the right hand side of each of these figures we show that, by minimising $P(x)$ as a function of x_2, we can predict the location of the surface very well even when 5% noise is added to the measurements.

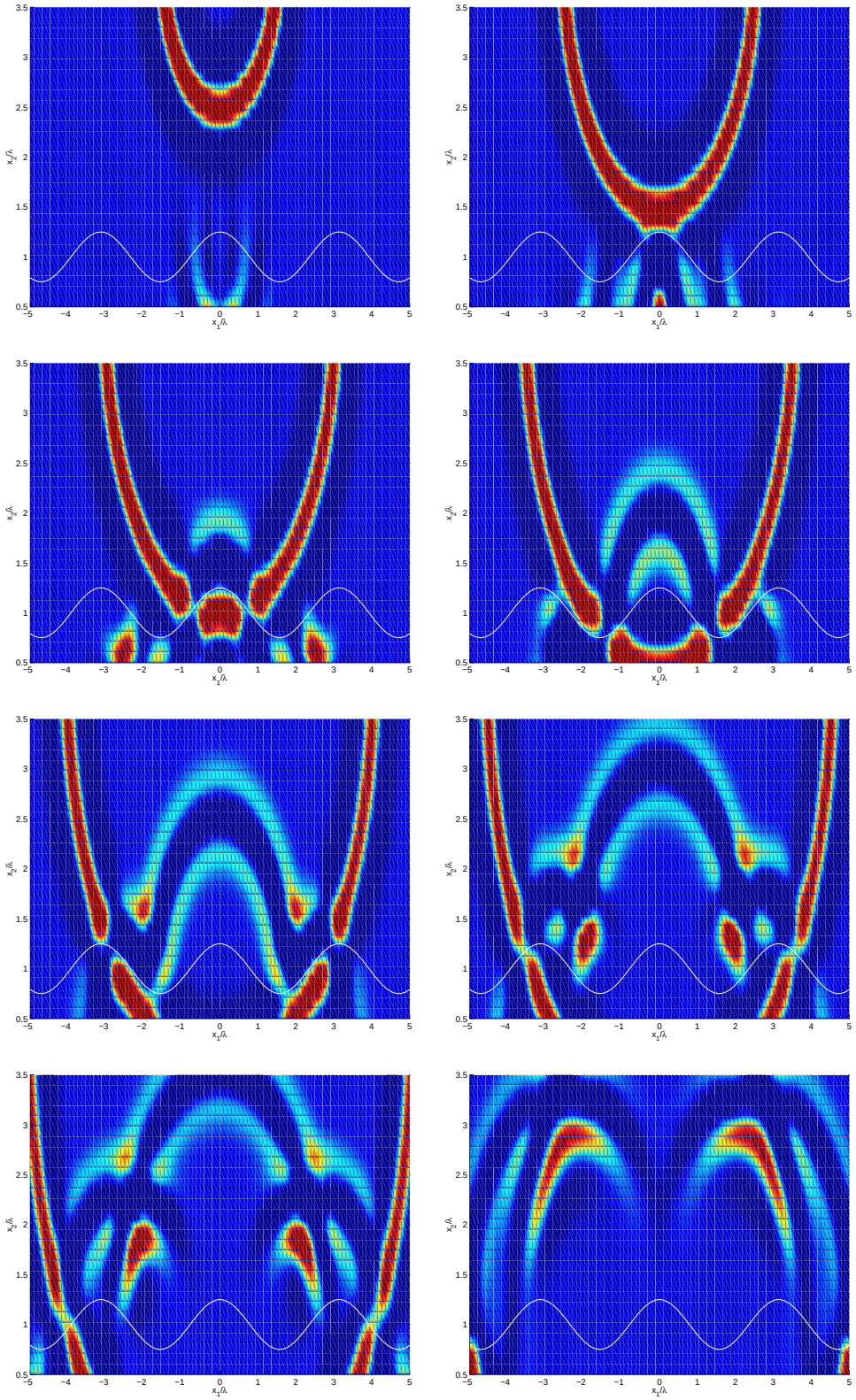

Figure 5.6: The reconstructed total field, $U_N^{\alpha}(x,t)$, for $t = 3.2$ns, 5.2ns, 6.2ns, 7.2ns, 8.2ns, 9.2ns, 10.2ns and 12.2ns (from top left to bottom right) for surface (5.14).

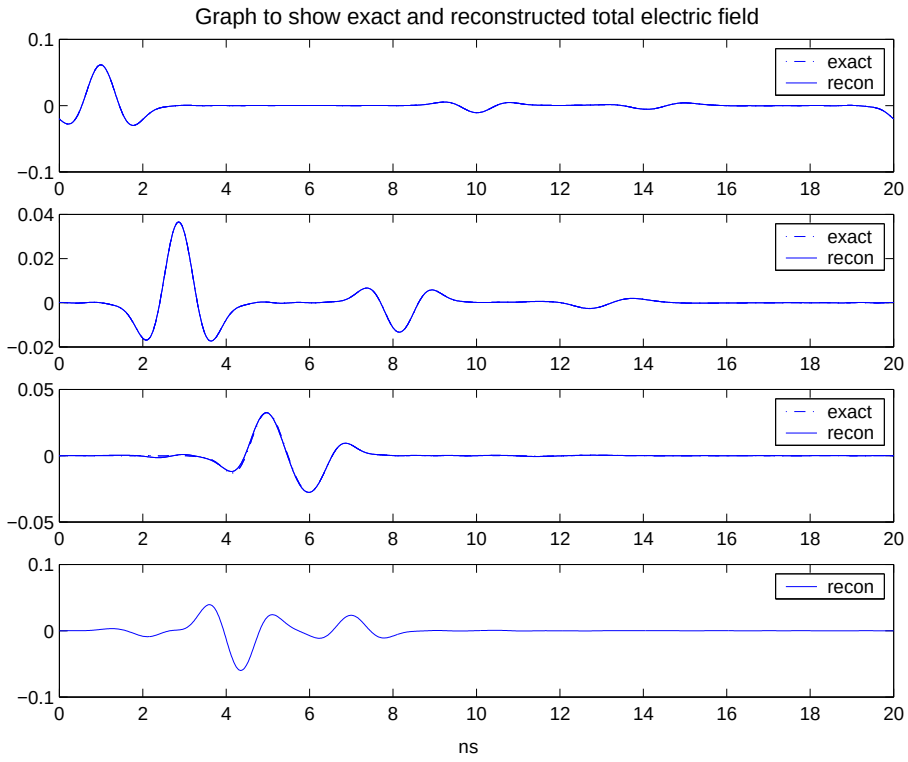

Figure 5.7: Comparison of the reconstructed total field, $U_N^\alpha(x,t)$, and the exact total field, $U_N(x,t)$, where $0 < t \leq T$, for the surface (5.14). The total fields are compared at the points $x = (0, 3.5\lambda)$, $x = (0, 2.6\lambda)$, $x = (0, 1.5\lambda)$ and $x = (0, 0.5\lambda)$ (from top to bottom). Note that the surface is at height 1.25λ. Thus the bottom plot shows a reconstructed total field for a point x below the surface. Note that the graphs are superposed.

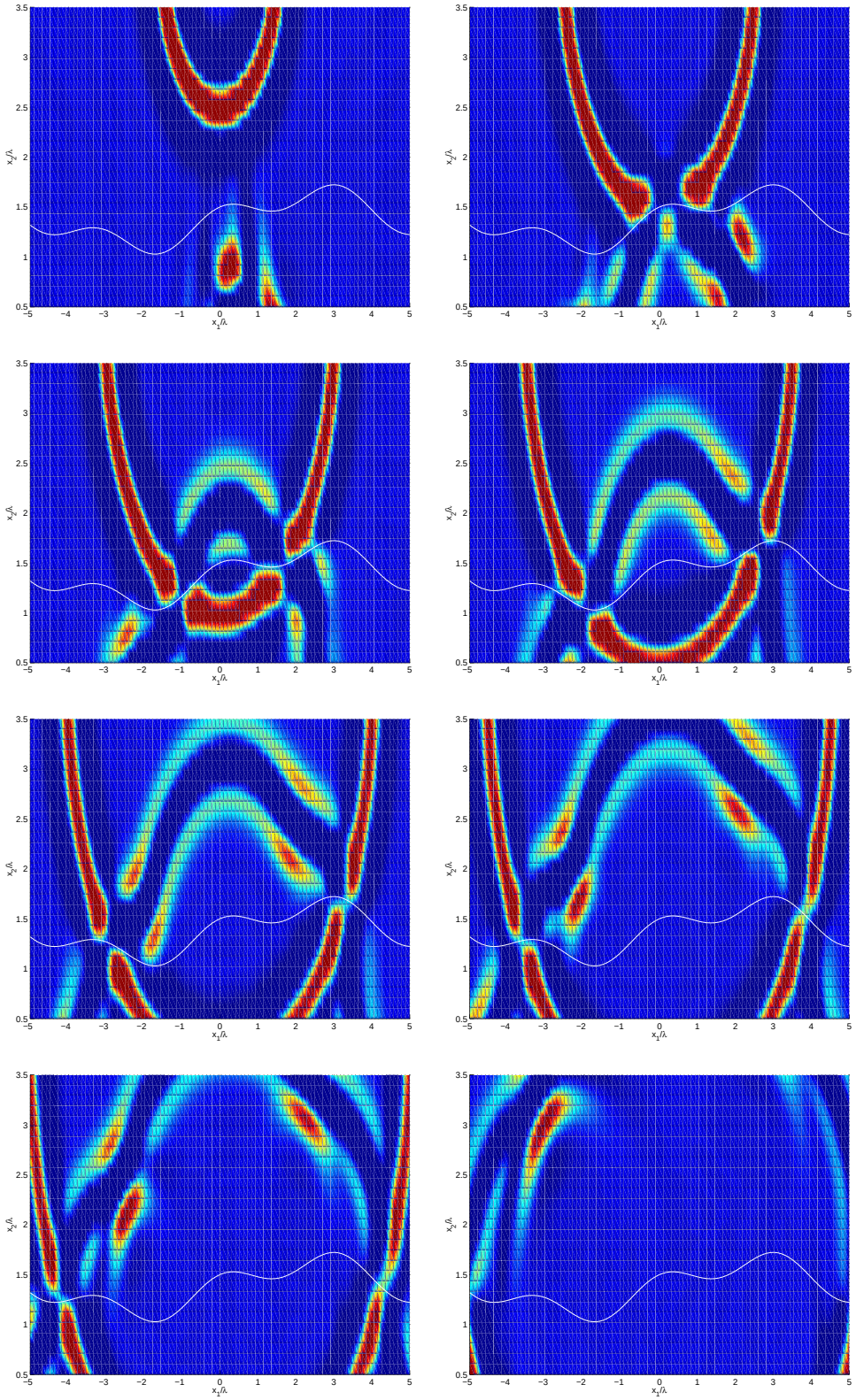

Figure 5.8: The reconstructed total field, $U_N^{\alpha}(x,t)$, for $t = 3.2$ns, 5.2ns, 6.2ns, 7.2ns, 8.2ns, 9.2ns, 10.2ns and 12.2ns (from top left to bottom right) for surface (5.15).

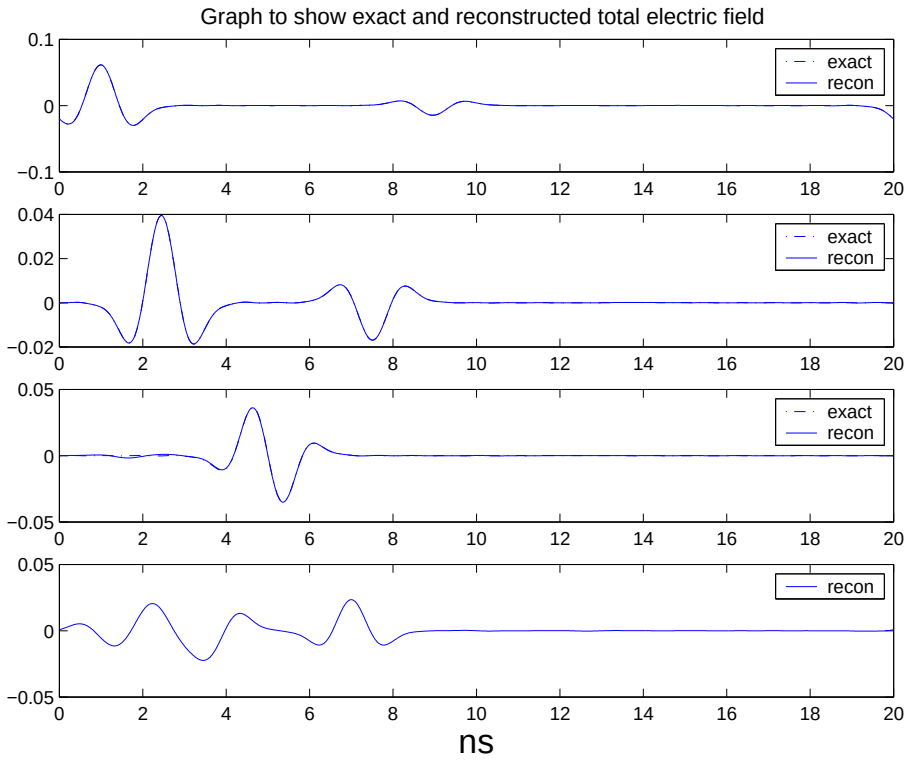

Figure 5.9: Comparison of the reconstructed total field, $U_N^{\alpha}(x,t)$, and the exact total field, $U_N(x,t)$, where $0 < t \leq T$, for the surface (5.15). The total fields are compared at the points $x = (0, 3.5\lambda)$, $x = (0, 2.6\lambda)$, $x = (0, 1.6\lambda)$ and $x = (0, 0.5\lambda)$ (from top to bottom). Note that the surface is at height 1.5λ. Thus the bottom plot shows a reconstructed total field for a point x below the surface. Note that the graphs are superposed.

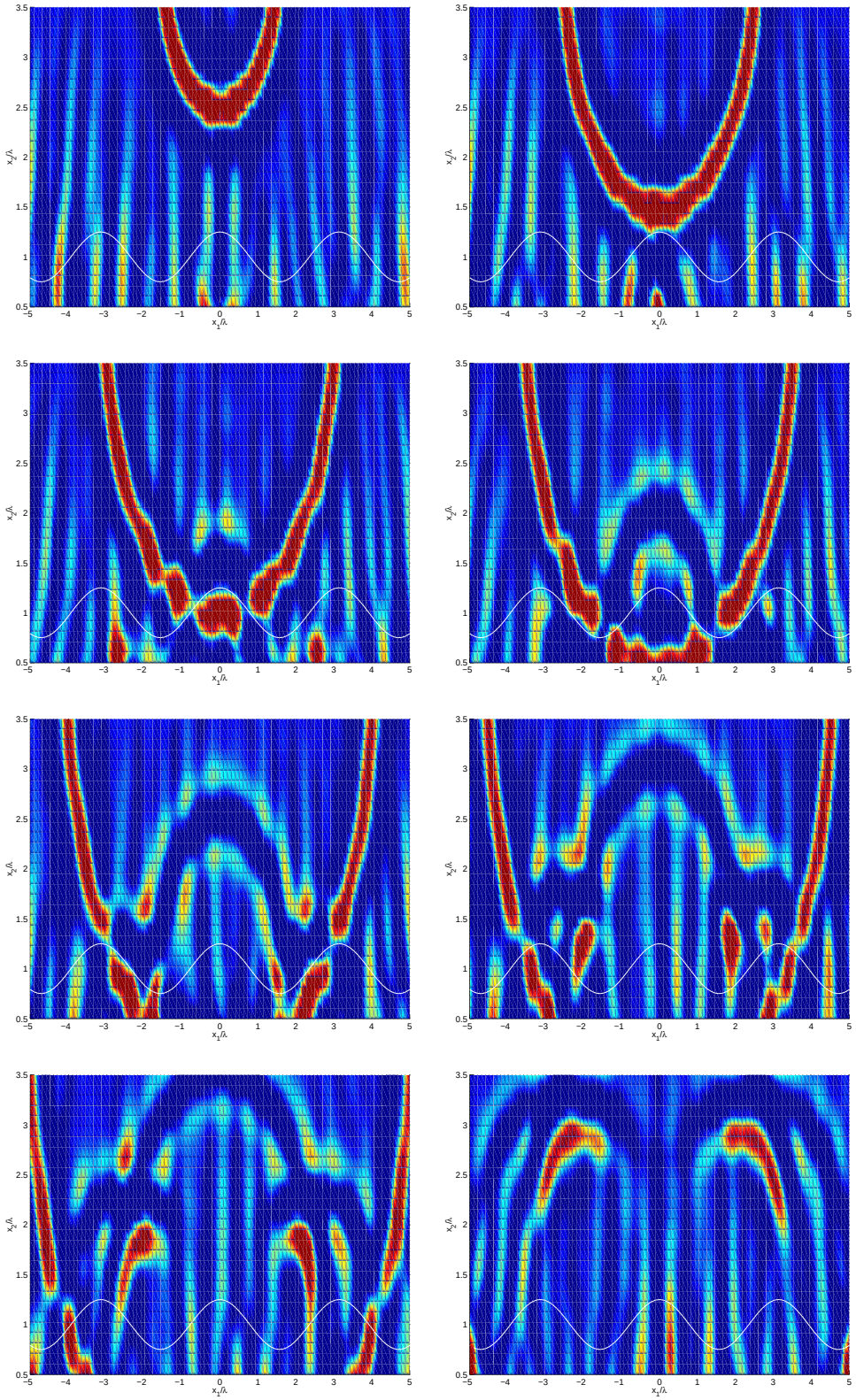

Figure 5.10: The reconstructed total field, $U^{\alpha}_{N,\delta}(x,t)$, for t = 3.2ns, 5.2ns, 6.2ns, 7.2ns, = 8.2ns, 9.2ns, 10.2ns and 12.2ns (from top left to bottom right) for surface (5.14) with $\delta^* = 5$, i.e 5% noise added to the measurement data.

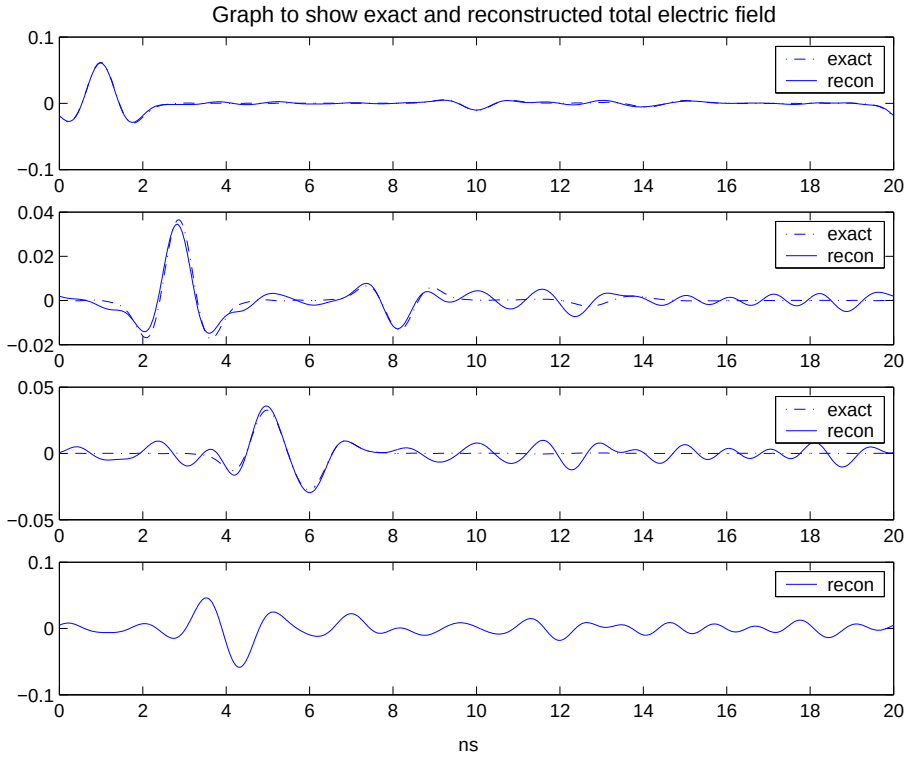

Figure 5.11: Comparison of the reconstructed total field, $U^{\alpha}_{N,\delta}(x,t)$, with $\delta^* = 5$, i.e. 5% noise added to the measurements, and the exact total field, $U_N(x,t)$, where $0 < t \leq T$, for the surface (5.14). The total fields are compared at the points $x = (0, 3.5\lambda)$, $x = (0, 2.6\lambda)$, $x = (0, 1.5\lambda)$ and $x = (0, 0.5\lambda)$ (from top to bottom). Note that the surface is at height 1.25λ. Thus the bottom plot shows a reconstructed total field for a point x below the surface.

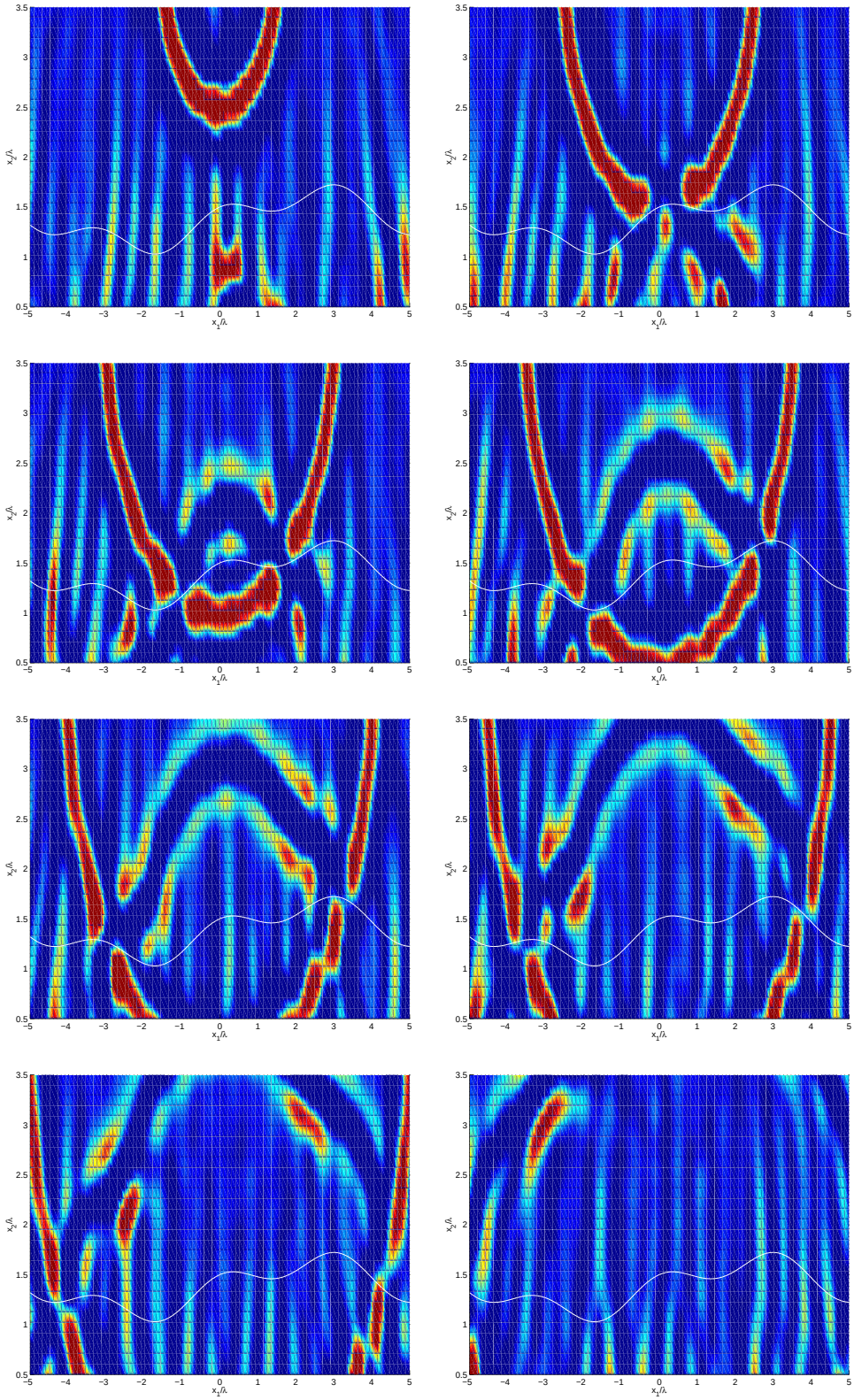

Figure 5.12: The reconstructed total field, $U^{\alpha}_{N,\delta}(x,t)$, for $t = 3.2$ns, 5.2ns, 6.2ns, 7.2ns, 8.2ns, 9.2ns, 10.2ns and 12.2ns (from top left to bottom right) for surface (5.15) with $\delta^* = 5$, i.e 5% noise added to the measurement data.

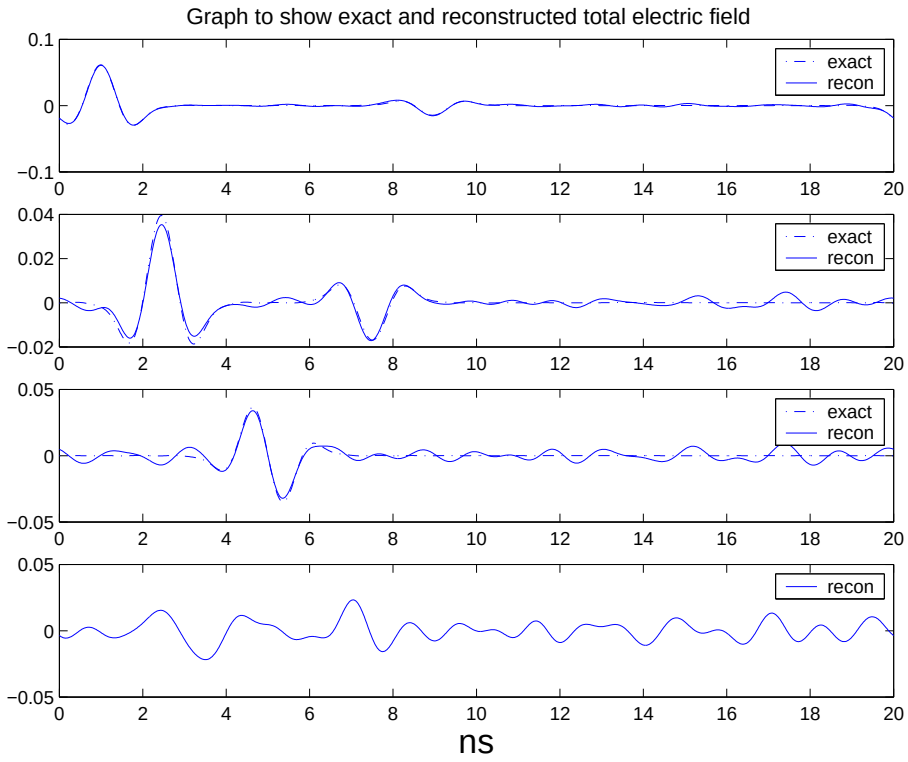

Figure 5.13: Comparison of the reconstructed total field, $U^{\alpha}_{N,\delta}(x,t)$, with $\delta^* = 5$, i.e. 5% noise added to the measurements, and the exact total field, $U_N(x,t)$, where $0 < t \leq T$, for the surface (5.15). The total fields are compared at the points $x = (0, 3.5\lambda)$, $x = (0, 2.6\lambda)$, $x = (0, 1.6\lambda)$ and $x = (0, 0.5\lambda)$ (from top to bottom). Note that the surface is at height 1.5λ. Thus the bottom plot shows a reconstructed total field for a point x below the surface.

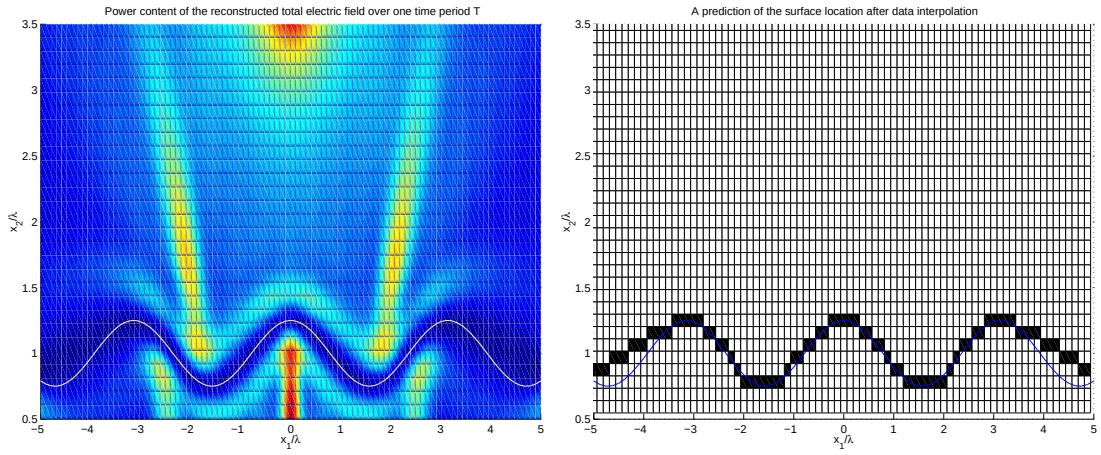

Figure 5.14: A plot of the power content, $P(x)$, of the electric field (left hand side) for surface (5.14). On the right hand side we predict the surface location from this plot by colouring in, in each column, the square in which $P(x)$ is minimised as a function of x_2.

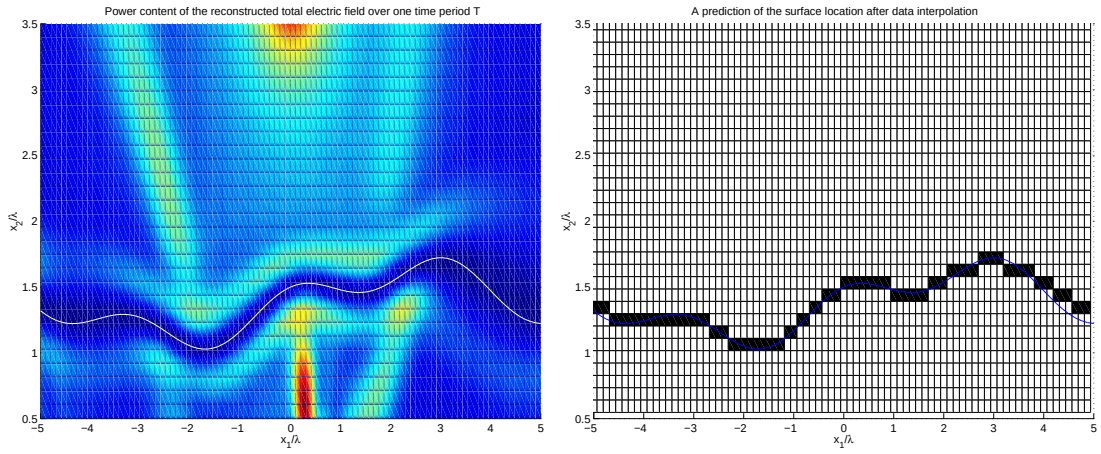

Figure 5.15: A plot of the power content, $P(x)$, of the electric field (left hand side) for surface (5.15). On the right hand side we predict the surface location from this plot by colouring in, in each column, the square in which $P(x)$ is minimised as a function of x_2.

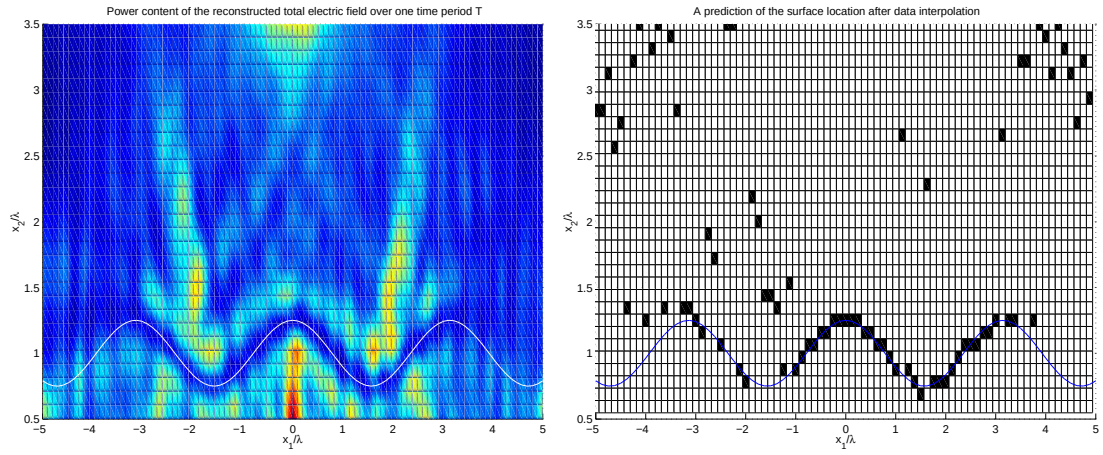

Figure 5.16: A plot of the power content, $P(x)$, of the electric field (left hand side) for surface (5.14) when 5% noise is added to the measurements. On the right hand side we predict the surface location from this plot by colouring in, in each column, the square in which $P(x)$ is minimised as a function of x_2.

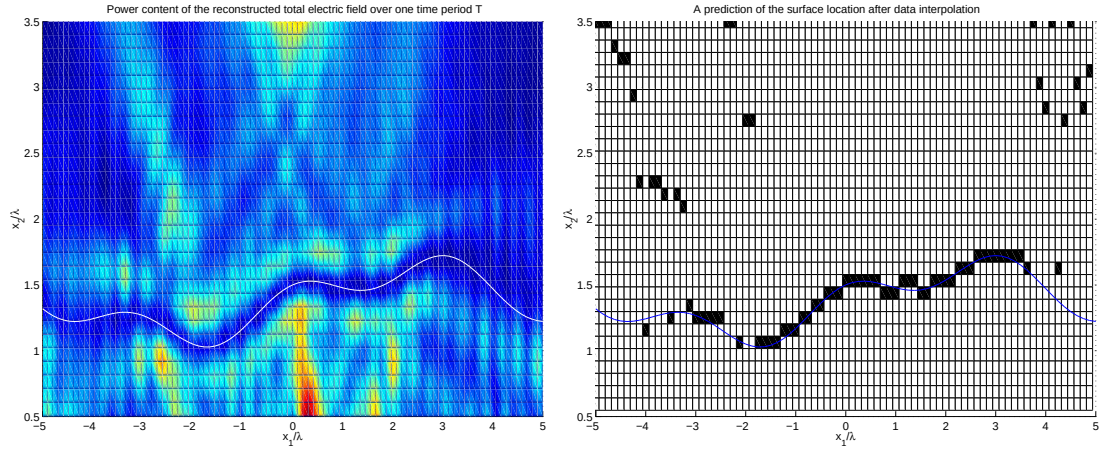

Figure 5.17: A plot of the power content, $P(x)$, of the electric field (left hand side) for surface (5.15) when 5% noise is added to the measurements. On the right hand side we predict the surface location from this plot by colouring in, in each column, the square in which $P(x)$ is minimised as a function of x_2.

5.2.4 Effects of Noise level

In this set of numerical results we show the effect of the noise level when predicting the location of the surface. We compute $U^{\alpha}_{N,\delta}(x,t)$, as in Section 5.2.1, where $G_{k_p}(x,z)$ is replaced by the noisy data $G_{k_p,\delta}(x,z)$ in (5.11). For the surface (5.15), $U^{\alpha}_{N,\delta}(x,z)$ is computed on the two vertical lines, $x_1 = 0$ and $x_1 = 4\lambda$, for $\lambda/2 < x_2 < 5\lambda/2$ (see Figure 5.18). On each vertical line we compute the value of x_2, denoted by X_2, which minimises $P(x)$, given by (5.13), over some range of x_2. The range of x_2 is either $\lambda/2 < x_2 < 5\lambda/2$ or the part of this interval which lies within distance $\lambda/3$ of the surface, i.e. $\max(\lambda/2, f(x_1) - \frac{\lambda}{3}) < x_2 < \min(f(x_1) + \frac{\lambda}{3}, 5\lambda/2)$. X_2 is a time domain point source estimate of the surface height, $f(x_1)$. Using each of the ranges of x_2, X_2 is computed for 20 values of δ^*, logarithmically spaced on the interval $0.0001 < \delta^* < 12$. As in Section 4.3.3 we choose $\alpha = 10^{-4}\delta^*/5$ so that $\alpha \to 0$ as $\delta^* \to 0$. In Figure 5.19 we plot $|X_2 - f(x_1)|/\lambda$ against δ^*, i.e. we plot the

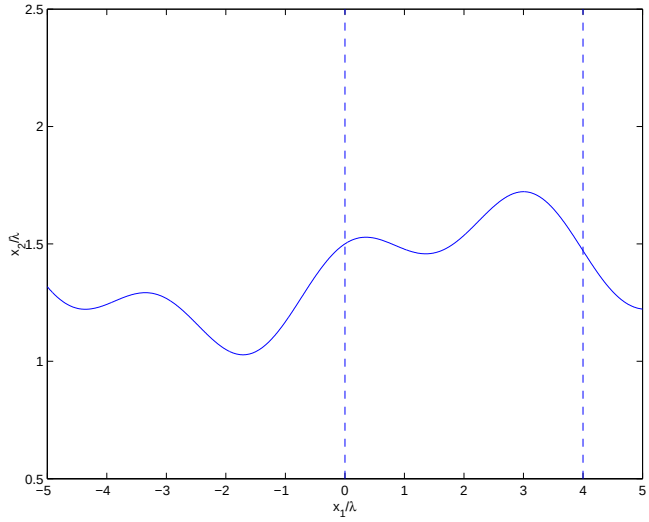

Figure 5.18: Graph to show the location of the two vertical lines on which $U^{\alpha}_{N,\delta}(x,z)$ is calculated.

distance of the predicted surface location from the actual surface (in wavelengths) as

the noise in the measurement data increases. In Figure 5.19 the top two plots show the results for $x_1 = 0$ (so $f(x_1) = 1.5\lambda$) and the bottom two plots show the results for $x_1 = 4\lambda$ (so $f(x_1) = 1.4711\lambda$). In both sets of results shown in Figure 5.19 the blue line indicates the distance of X_2 from $f(x_1)$ when x_2 minimises $P(x)$ over the range $\lambda/2 < x_2 < 5\lambda/2$. Also shown in each plot is a red line which shows the distance of X_2 from $f(x_1)$ when x_2 minimises $P(x)$ over the range $f(x_1) - \lambda/3 < x_2 < f(x_1) + \lambda/3$. As expected, as the percentage of noise added to the measurement data increases, the accuracy with which the prediction algorithm described above predicts the surface location worsens. Comparing the results for $x_1 = 0$ and $x_1 = 4\lambda$ we can see that the accuracy with which the surface location is predicted is significantly better for $x_1 = 0$ than for $x_1 = 4\lambda$. For small δ^* the results show that the surface location can be predicted to within $10^{-3}\lambda$ for $x_1 = 0$ and to within $10^{-1.4}\lambda$ for $x_1 = 4\lambda$. These results are consistent with the results in Section 4.3.2 and Section 5.2.2 where it was observed that as $|x_1|$ approaches the end of the measurement line, i.e. 10λ, the prediction of the surface location worsens. In each plot in Figure 5.19 we plot, in green, $C(\delta^*)^{\frac{1}{2}}$, for some real valued constant, C, against δ^*. Comparing with this plot we can observe that the accuracy with which the surface location is predicted converges at a rate of approximately $\delta^{*\frac{1}{2}}$ for $x_1 = 0$ but the rate of convergence for $x_1 = 4\lambda$ appears slower. Comparing these results with those in Section 4.3.3 it can be observed that there is no difference in the rate of convergence of accuracy of the prediction of the surface location. However the accuracy of the predicted surface location is improved when using the time domain algorithm, especially for larger δ^*. The results in Section 4.3.3 show that when $\delta^* > 2$ (for $x_1 = 0$) and when $\delta^* > 1$ (for $x_1 = 4\lambda$) the prediction of the surface location improves if x_2 is restricted to $f(x_1) \pm \lambda/3$. The results in this section show that only when $\delta^* > 8$ (for $x_1 = 0$) and $\delta^* > 2$ (for $x_1 = 4\lambda$) can we see any improvement. These results are consistent with the results in Section 4.3.2 where it was observed that by combining the results of several frequencies we could eradicate the occurrence of repeated minima.

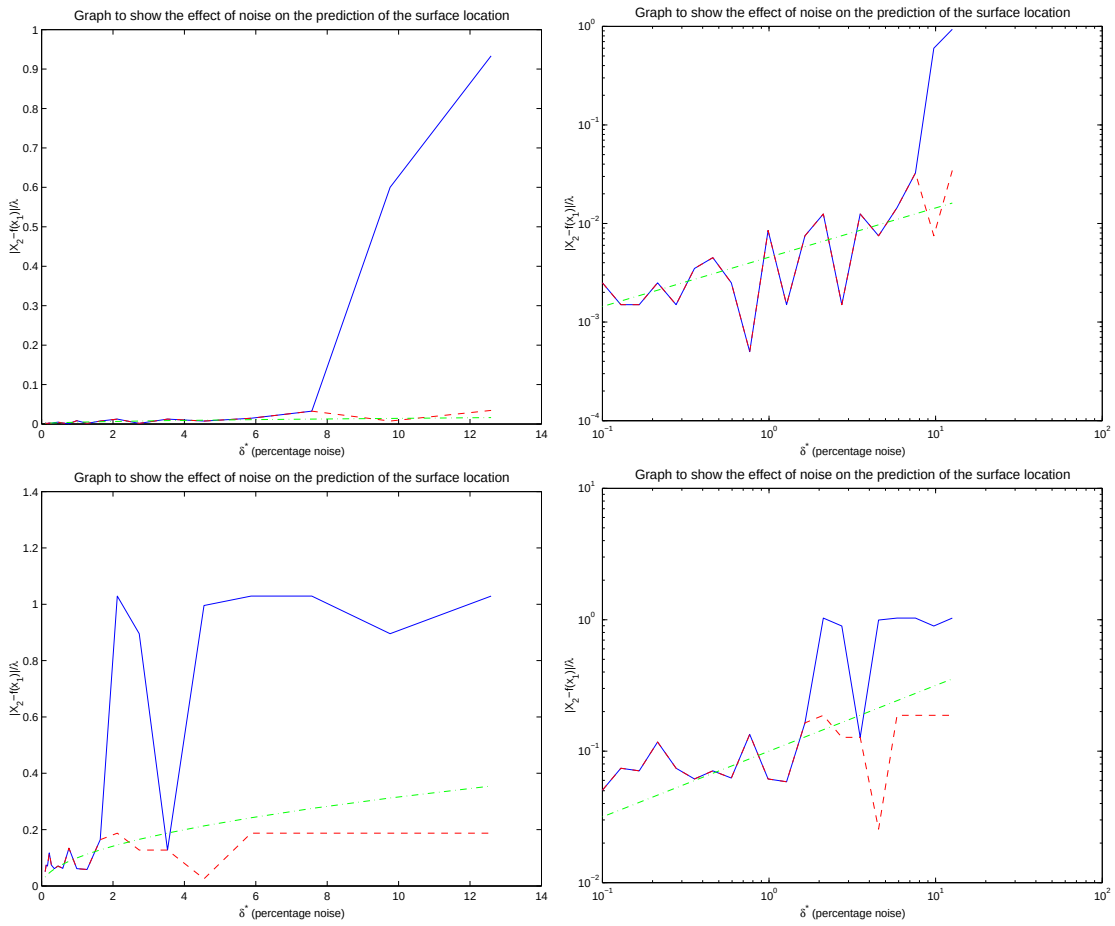

Figure 5.19: Results showing the accuracy of the predicted surface location as δ^* increases. Shown are results for the rough surface (5.15) where $U^{\alpha}_{N,\delta}(x,z)$ is calculated on the vertical line $x_1 = 0$ (top two plots) and on the vertical line $x_1 = 4\lambda$ (bottom two plots). The left hand plots indicate in wavelengths the distance of X_2 from the surface height, $f(x_1)$, and the right hand plots show the same data on a logarithmic scale. The blue line shows the distance of X_2 from $f(x_1)$ when x_2 minimises $P(x)$ over the range $\lambda/2 < x_2 < 5\lambda/2$ and the red line shows the distance of X_2 from $f(x_1)$ when x_2 minimises $P(x)$ over the range $f(x_1) - \lambda/3 < x_2 < f(x_1) + \lambda/3$.

Chapter 6

Conclusions and Future Work

In this thesis we have presented and fully analysed a new Point Source Method for inverse scattering by unbounded one-dimensional rough surfaces when the measured data are the field on a finite line above the surface and the source is a time harmonic point source. We have included numerical examples for a range of surface profiles that show that the Point Source Method can accurately reconstruct the total field below the measurement line and above the surface although the accuracy achieved depends on a number of variables. We show that we can predict the location and the shape of the surface, for the configuration we use, where the source is in the middle of the measurement line, although the reconstructions of the surface are significantly poorer underneath the ends of the measurement line compared to underneath the middle.

In Chapter 5 we consider the case when the source emits a pulse localised in time and propose novel reconstructions algorithms in this case too. Numerical examples in the time domain for two surface profiles are shown, using an incident pulse appropriate for a ground penetrating radar (GPR) antenna of 500MHz. Reconstructions of the total field are shown to agree well with the exact values of the total field as a function of position and time, and predictions of surface location and shape are good. We have also shown that when noise is added to the measurements we can still predict the surface location although the region where the surface is predicted accurately is smaller.

Further investigation is required on a number of fronts. We have not investigated experimentally how the choice of α, the regularisation parameter, affects the accuracy of the results especially when noise is added to the measurements, and, while the results of sections 4.3.3 and 5.2.4 suggest that choosing α proportional to noise level is fairly effective, further work is required to determine an optimum choice of α as a function of noise level and other variables. Further work is also needed to try to improve the accuracy of the reconstructions when the amplitude of the surface is increased.

There is a large scope for building on the work accomplished in this thesis. An obvious next step is to develop the Point Source Method such that reconstructions can be made in three dimensions. Another possibility is to extend the method, particularly in the time domain, so that predictions of the location of surfaces with more general boundary conditions can be made, for example surfaces that are not perfectly conducting but allow the transmission of energy. Future applications of the Point Source Method could include the detection of buried interfaces using GPR although, in addition to the possible advances mentioned above, more accurate modelling of the source would be necessary.

Chapter 7

The Appendix

Appendix A. Properties of the layer Potentials

In this appendix we state properties of the single and double-layer potentials which appear throughout this thesis. We assume throughout that $f \in B$, where B is defined by

$$B = B(c_1, c_2) := \{f \in C^{1,1}(\mathbb{R}) | f(s) \geq c_1, s \in \mathbb{R} \text{ and } \|f\|_{C^{1,1}(\mathbb{R})} \leq c_2\}, \tag{A.1}$$

for some $c_1 \in \mathbb{R}$, $c_2 > 0$. We remind the reader that $\nu(x)$ denotes the unit normal at $x \in \Gamma$, directed out of D.

For $\psi \in BC(\Gamma)$, $h < c_1$ we call the integrals

$$V(x) = \int_\Gamma G_{1,h}(x,y)\psi(y)\mathrm{ds}(y), \qquad x \in \overline{U_h}\backslash\Gamma, \tag{A.2}$$

$$W(x) = \int_\Gamma \frac{\partial G_{1,h}(x,y)}{\partial \nu(y)}\psi(y)\mathrm{ds}(y), \qquad x \in \overline{U_h}\backslash\Gamma, \tag{A.3}$$

single-layer and double-layer potentials, respectively, with density ψ. For a proof of the following properties see [8, lemmas A.1 and A.2] and [6, 48].

Lemma A.1 *[58] For W defined by (A.3), the following results hold.*

(i) Define $S := \{x \in \mathbb{R}^2 | 2h - c_1 < x_2 < f(x_1)\}$. Then $W \in C^2(S \cup D)$ and $\triangle W + k^2 W = 0$ in $S \cup D$.

(ii) W can be continuously extended from D to $\overline{D}$ and from $U_h\backslash\overline{D}$ to $U_h\backslash D$ with limiting values

$$W_\pm(x) = \int_\Gamma \frac{\partial G_1(x,y)}{\partial \nu(y)}\psi(y)\,ds(y) \mp \frac{1}{2}\psi(x), \qquad x \in \Gamma, \tag{A.4}$$

where

$$W_\pm(x) := \lim_{p \to 0, p>0} W(x \mp p\nu(x)).$$

The integral exists as an improper integral.

Lemma A.2 *[58] For V defined by (A.2), the following results hold.*

(i) With S defined as in Lemma A.1, $V \in C^2(S \cup D) \cap C(S \cup D \cup \Gamma)$ and $\triangle V + k^2 V = 0$ in $S \cup D$.

(ii) On the boundary Γ we have

$$V(x) = \int_\Gamma G_{1,h}(x,y)\psi(y)\,ds(y), \qquad x \in \Gamma, \tag{A.5}$$

$$\frac{\partial V_\pm}{\partial \nu}(x) = \int_\Gamma \frac{\partial G_{1,h}(x,y)}{\partial \nu(x)}\psi(y)\,ds(y) \pm \frac{1}{2}\psi(x), \qquad x \in \Gamma, \tag{A.6}$$

where

$$\frac{\partial V_\pm}{\partial \nu}(x) := \lim_{p \to 0, p>0} \nu(x) \cdot \nabla V(x \mp p\nu(x)), \tag{A.7}$$

and the convergence in (A.7) is uniform on compact subsets of Γ. The integrals (A.5) and (A.6) exist as improper integrals.

Lemma A.3 *[8] There holds*

$$\frac{\partial W(x)}{\partial x_2} + ikW(x) = 0 \tag{A.8}$$

for $x \in \Gamma_h$.

Bibliography

[1] R. A. Adams. *Sobolev Spaces*. Academic Press, New York; London [etc.], 1975.

[2] T. Arens, S. N. Chandler-Wilde, and K. Haseloh. Solvability and spectral properties of integral equations on the real line: II. L^p spaces and applications. *J. Int. Equ. Appl.*, 15:1–35, 2003.

[3] K. E. Atkinson and W. Han. *Theoretical Numerical Analysis, A Functional Analysis Framework*. Springer, New York, 2001.

[4] S. N. Chandler-Wilde. The impedance boundary value problem for the Helmholtz equation in a half-plane. *Math. Meth. Appl. Sci.*, 20:813–840, 1997.

[5] S. N. Chandler-Wilde and D. C. Hothersall. Efficient calculation of the Green function for acoustic propagation above a homogeneous impedance plane. *J. Sound Vib.*, 180:705–724, 1995.

[6] S. N. Chandler-Wilde and C. R. Ross. Scattering by rough surfaces: the Dirichlet problem for the Helmholtz equation in a non-locally perturbed half-plane. *Math. Meth. Appl. Sci.*, 19:959–976, 1996.

[7] S. N. Chandler-Wilde, C. R. Ross, and B. Zhang. Scattering by rough surfaces. In J. DeSanto, editor, *Proceedings of the Fourth International Conference on Mathematical and Numerical Aspects of Wave Propagation*, pages 164–168. SIAM, 1998.

[8] S. N. Chandler-Wilde, C. R. Ross, and B. Zhang. Scattering by infinite one-dimensional rough surfaces. *Proc. R. Soc. Lon. A*, 455:3767–3787, 1999.

[9] S. N. Chandler-Wilde and B. Zhang. Electromagnetic scattering by an inhomogenous conducting or dielectric layer on a perfectly conducting plate. *Proc. R. Soc. Lon. A*, 454:519–542, 1998.

[10] S. N. Chandler-Wilde, B. Zhang, and C. R. Ross. On the solvability of second kind integral equations on the real line. *J. Math. Anal. Appl.*, 245:28–51, 2000.

[11] D. Colton, J. Coyle, and P. Monk. Recent developments in inverse acoustic scattering theory. *SIAM Rev.*, 42:369–414, 2000.

[12] D. Colton and A. Kirsch. A simple method for solving inverse scattering problems in the resonance region. *Inverse Problems*, 12:383–393, 1996.

[13] D. Colton and R. Kress. *Integral Equation Methods in Scattering Theory*. Wiley, New York, 1983.

[14] D. Colton and R. Kress. *Inverse Acoustic and Electromagnetic Scattering Theory*. Springer, Berlin, second edition, 1998.

[15] D. Colton and P. Monk. The numerical solution of the three dimensional inverse scattering problem for time harmonic acoustic waves. *SIAM J. Sci. Stat. Comp.*, 8:278–291, 1987.

[16] D. Colton, M. Piana, and R. Potthast. A simple method using Morozov's discrepancy principle for solving inverse scattering problems. *Inverse Problems*, 13:1477–1493, 1997.

[17] R. Dautray and J. Lions. *Mathematical Analysis and Numerical Methods for Science and Technology. Volume 2: Functional and Variational methods*. Springer-Verlag, Berlin, 1988.

[18] J. A. DeSanto. Scattering by rough surfaces. In R. Pike and P. Sabatier, editors, *Scattering: Scattering and Inverse Scattering in Pure and Applied Science*, pages 15–36. Academic Press, 2002.

[19] J. A. DeSanto and R. J. Wombell. The reconstruction of shallow rough-surface profiles from scattered field data. *Inverse Problems*, 7:L7–L12, 1991.

[20] M. Engl, H. W. Hanke and A. Neubauer. *Regularization of Inverse Problems*. Kluwer Academic Publishers, 2000.

[21] G. Franceschetti, A. Iodice, S. Maddaluno, and D Riccio. A fractal-based theoretical framework for retrieval of surface parameters from electromagnetic backscattering data. *IEEE Trans. on Geoscience and Remote Sensing*, 38:641–649, 2000.

[22] D. Gilbarg and N. S. Trudinger. *Elliptic Partial Differential Equations of Second Order*. Springer, Berlin, second edition, 1983.

[23] D. Goodman and L. Conyers. *Ground Penetrating Radar, An Introduction for Archaeologists*. AltaMira, 1997.

[24] C. A. Guerin, M. Holschneider, and M. Saillard. Electromagnetic scattering from multi-scale rough surfaces. *Waves in Random Media*, 7:331–349, 1997.

[25] K. Harada and A. Noguchi. Reconstruction of two dimensional rough surface with gaussian beam illumination. *IEICE Trans. Electron.*, E79-C(10):1345–1349, 1996.

[26] V. Isakov. *Inverse Problems for Partial Differential Equations*. Springer, New York, 1998.

[27] F. Jones. *Lebesgue Integration on Euclidean Space*. Jones and Bartlett Publishers, Inc, 1993.

[28] A. Kirsch. The domain derivative and two applications in inverse scattering. *Inverse Problems*, 9:81–96, 1993.

[29] A. Kirsch. Numerical algorithm in inverse scattering theory. In Jarvis and Sleeman, editors, *Ordinary and partial differential equations. Vol IV*, pages 93–111. Pitman Research Notes in Mathematics, 1993.

[30] A. Kirsch. *An Introduction to the Mathematical Theory of Inverse Problems*. Springer, Berlin, 1996.

[31] A. Kirsch. Characterization of the shape of a scattering obstacle using the spectral data of the far field operator. *Inverse Problems*, 14:1489–1512, 1998.

[32] A. Kirsch. Factorization of the far field operator for the inhomogeneous medium case and an application in inverse scattering theory. *Inverse Problems*, 15:413–429, 1999.

[33] A. Kirsch and R. Kress. An optimization method in inverse acoustic scattering. In C. Brebbia, W. Wendland, and G. Kuhn, editors, *Boundary Elements IX*, pages 3–18. Spinger-Verlag, Heidelberg, 1987.

[34] R. Kress. *Linear Integral Equations*. Springer, Berlin, 1989.

[35] R. Kress. Integral equation methods in inverse acoustic and electromagnetic scattering. In Ingham and Wrobel, editors, *Boundary Integral Formulations for Inverse Analysis*, pages 67–92. Computational Mechanics Publications, Southampton, 1997.

[36] V. Malyshkin, S. Simeonov, A. R. McGurn, and A. A. Maradudin. Determination of surface profile statistics from electromagnetic scattering data. *Opt. Lett.*, 22:58–63, 1997.

[37] T. Marchand and G. S. Brown. Inferring rough surface parameters from average scattering data using approximate scattering models. 1. Gaussian spectrum. *Radio Science*, 33(4):821–834, 1998.

[38] T. Marchand and G. S. Brown. Inferring rough surface paramters from average scattering data using approximate scattering models. 2. Pierson-Moskowitz spectrum. *Radio Science*, 33(4):835–843, 1998.

[39] W. McLean. *Strongly Elliptic Systems and Boundary Integral Equations*. Cambridge University Press, 2000.

[40] A. Meier. *Numerical Treatment of Integral Equations on the Real Line with Application to Acoustic Scattering by Unbounded Rough Surfaces*. PhD thesis, Brunel University, 2001.

[41] A. Meier, T. Arens, S. N. Chandler-Wilde, and A. Kirsch. A Nyström method for a class of integral equations on the real line with applications to scattering by diffraction gratings and rough surfaces. *J. Int Equ. Appl.*, 12:281–321, 2000.

[42] D. E. Newland. *An Introduction to Random Vibrations, Spectral and Wavelet Analysis*. Longman, 1993.

[43] J. A. Ogilvy. *Theory of Wave Scattering from Random Rough Surfaces*. Adam Hilger, Bristol, 1991.

[44] R. Potthast. A point source method for inverse acoustic and electromagnetic obstacle scattering problems. *IMA J. Appl. Math.*, 61:119–140, 1998.

[45] R. Potthast. *Point Sources and Multipoles in Inverse Scattering Theory*. CRC Press, 2001.

[46] R. Potthast and D. Luke. The no response test - a sampling method for inverse scattering problems. *To appear in Siam J. Appl. Math.*

[47] R. Potthast, J. Sylvester, and S. Kusiak. A 'Range test' for determining scatterers with unknown physical properties. *Inverse Problems*, 19:533–547, 2003.

[48] C. R. Ross. *Direct and Inverse Scattering by Rough Surfaces*. PhD thesis, Brunel University, 1996.

[49] M. Saillard and A. Sentenac. Rigorous solutions for electromagnetic scattering from rough surfaces. *Waves Random Media*, 11:R103–R137, 2001.

[50] C. Sheppard. Imaging of random surfaces and inverse scattering in the Kirchhoff approximation. *Waves in Random Media*, 8:53–66, 1998.

[51] M. Spivack. Direct solution of the inverse problem for rough scattering at grazing incidence. *J. Phys. A: Math. Gen*, 25:3295–3302, 1992.

[52] M. Spivack. Solution of the inverse-scattering problem for grazing incidence upon a rough surface. *J. Opt, Soc. Am. A*, 9:1352–1355, 1992.

[53] E. C. Titchmarsh. *The Theory of Functions*. Oxford University Press, 1952.

[54] K.F. Warnick and W. C. Chew. Numerical simulation methods for rough surface scattering. *Waves Random Media*, 11:R1–R30, 2001.

[55] R. J. Wombell and J. A. DeSanto. Reconstruction of rough-surface profiles with the Kirchhoff approximation. *J. Opt. Soc. Am.*, 8:1892–1897, 1991.

[56] C. Ying and A. Noguchi. Rough surface inverse scattering problem with gaussian beam illumination. *IEICE Trans. Electron.*, E77-C(11):1781–1785, 1994.

[57] E. Zeidler. *Applied Functional Analysis: Main Principles and Their Applications*. Springer, New York, 1995.

[58] B. Zhang and S. N. Chandler-Wilde. Integral equation methods for scattering by infinite rough surfaces. *Math. Meth. Appl. Sci.*, 26:463–488, 2003.